School of Chemical and Petroleum Engineering

Microchanneled ceramic membranes for oxygen separation from air

Xin Shao

This thesis is presented for the Degree of

Doctor of Philosophy

of Curtin University

February 2015

Declaration

To the best of my knowledge and belief this thesis contains no material previously published by any other person except where due acknowledgement has been made.

This thesis contains no material which has been accepted for the award of any other degree or diploma in any university.

Signature:.....Xin shao.....

Date:.....25/3/2015.....

Abstract

Ceramic membranes for oxygen separation have attracted significant attention in recent years because they enable a low cost technology of oxygen production for oxygen consuming industries and medical applications. Although good progress has already been made regarding the development of either high oxygen flux materials or chemically stable materials, these two features have never been demonstrated in a single material used for oxygen permeation. An effective route to overcoming this problem is to develop novel microstructures, because the microstructure could be applied to any materials, including the materials with good chemical stability. The overall objective of this thesis is to develop a new membrane microstructure that can potentially improve the oxygen flux through a ceramic membrane.

A novel microchanneled membrane has been developed using a mesh-templating phase inversion process. Such membranes showed more than 5 times oxygen flux compared with a conventional dense disk membrane. It is believed that the microchannels are formed by the rapid convection of water and organic solvent during the phase inversion and the membrane microstructure is greatly affected by process parameters. Among the microchanneled membranes with different microstructures, the highest oxygen flux was produced by the membrane with the thinnest dense layer and the highest surface area. Further improvement of the oxygen flux has been attempted through using dual-phase membranes and applying catalysts on the membrane surfaces. The open microchannel structure facilitated the coating of catalysts on both sides of the membranes because catalyst can readily be delivered to the membrane surface on the microchannel side through the numerous microchannels.

Moreover, it has been found that the microchannel walls in microchanneled membranes contribute to oxygen flux. Thus, by increasing membrane thickness, the oxygen flux of the microchanneled membrane gradually increased in pure oxygen atmosphere. However, in air atmosphere, the oxygen flux of the microcahnneled membranes decreased by increasing the membrane thickness. It indicated the oxygen diffusion in gas phase was involved into the rate limiting steps of oxygen permeation in the microchanneled membranes. The gas diffusion resistance of the microchanneled membrane was also found much smaller than that of a supported membrane.

Acknowledgements

I would like to express my sincere gratitude to my supervisors Professor Chun-Zhu Li, Dr. Dehua Dong and Professor Gordon Parkinson for their constant supports, guidance and inspirations. During my PhD study, they gave me numerous valuable advices, comments and ideas and I have solved plenty of scientific problems, confusions through discussion with them. With their guidance and direction, we won the Curtin commercial innovation award and the Western Australia innovator award in 2013. I could not complete my PhD without each one of them.

I also would like to thank Angelina Rossiter, Tasneem Dawood and John Bromly, Zhitao Wang, Shanshan Xu, Yao Song, Liping Wu, Shuai Wang, Lei Zhang, Tingting Li, Dr. Yi Wang, Dr. Shu Zhang, Dr. Li Dong, Dr. Xun Hu, Mortaza Gholizadeh, Dr. Richard Gunawan, Dr. Kun Zhang, Yi Cheng, Jin Zhang, Dr. Kongfa Chen, Dr. Na Ai, Chengcheng Wang and all the members in our research institute for their help, advice and friendship throughout my PhD study.

I also sincerely acknowledge the financial support for this thesis from following sources:

- Australia Research Council Discovery Project (DP120103317).

- Curtin University of Technology through the Curtin Research Fellowship scheme.

I also thank Curtin University of Technology for awarding me a Curtin International Postgraduate Research Scholarship.

Finally, I would like to thank my parents and my girlfriend who constantly support me. Without their selfless love and concern, it would have been impossible for me to have completed this thesis.

List of publications, patent and awards

Publications

[1] D. Dong, **X. Shao**, Z. Wang, C. Lievens, J. Yao, H. Wang, C.-Z. Li, Fibrous NiO/CeO2 nanocatalysts for the partial oxidation of methane at microsecond contact times, RSC Advances, 3 (2013) 1341-1345.

[2] Z. Wang, **X. Shao**, A. Larcher, K. Xie, D. Dong, C.-Z. Li, A study on carbon formation over fibrous NiO/CeO2 nanocatalysts during dry reforming of methane, Catalysis Today, 216 (2013) 44-49.

[3] **X. Shao**, D. Dong, G. Parkinson, C.-Z. Li, A microchanneled ceramic membrane for highly efficient oxygen separation, Journal of Materials Chemistry A, 1 (2013) 9641-9644.

[4] **X. Shao**, D. Dong, G. Parkinson, C.-Z. Li, Microstructure control of oxygen permeation membranes with templated microchannels, Journal of Materials Chemistry A, 2 (2014) 410-417.

[5] **X. Shao**, D. Dong, G. Parkinson, C.-Z. Li, Improvement of oxygen permeation through microchanneled ceramic membranes, Journal of Membrane Science, 454 (2014) 444-450.

[6] Z. Wang, **X. Shao**, X. Hu, G. Parkinson, K. Xie, D. Dong, C.-Z. Li, Hierarchically structured NiO/CeO2 nanocatalysts templated by eggshell membranes for methane steam reforming, Catalysis Today, 228 (2014) 199-205.

[7] D. Dong, **X. Shao**, K. Xie, X. Hu, G. Parkinson, C.-Z. Li, Microchanneled anode supports of solid oxide fuel cells, Electrochemistry Communications, 42 (2014) 64-67.

Patent

D. H. Dong, C. -Z. Li, X. Shao and G. Parkinson, Channeled articles and methods for their manufacture, Australian Patent (Application No. 2013901454), 2013.

Awards

- ✓ Curtin Commercial Innovation Award, project of efficient oxygen separation membrane, 2013.

- ✓ Western Australia Innovator of the year Award (overall), for membranes, oxygen and renewable energy, 2013.

- ✓ Joint Chemical Engineering Committee of Western Australia (JCEC-WA) Postgraduate Research Excellence Award, 2015.

Table of contents

List of Figures

List of Tables

Chapter 1: Introduction

1.1. Background

Oxygen is one of the most sought after bulk chemicals in the world, being used in large quantities for steel making, chemical manufacture and medical uses. The global market is worth ca. $ 20nb pa.[1] Conventional cryogenic technology for oxygen production has been developed more than half century. The energy cost for the large scale pure oxygen production is about 0.3 kWh/Nm^3.[2] This technology was designed for tonnage scale production of oxygen, where there are economies of scale. It is too expansive to be used in medium or small scale due to the necessary large capital investment and operation costs. Another technology for oxygen production, pressure swing adsorption-desorption (PSA), produces oxygen with low purities (e.g. 90-95%).[3]

A relatively new technology, using ceramic ion transport membranes (ITMs) for oxygen separation, has been studied for more than three decades for its potential to replace the conventional technologies of oxygen separation. One of the major advantages is that this separation technology can be integrated with a high temperature membrane reactor, since the oxygen separation is operated at similar temperature to that at which many chemical reactions are carried out, such as natural gas conversion, coal gasification and oxyfuel combustion.[4-6] In the integrated membrane reactor, oxygen could be derived with little extra energy consumption. Another advantage is that ITMs produce oxygen that is nearly 100% pure.

However, this membrane separation technology has not yet been commercialized because of two major problems: low oxygen permeation rates and poor membrane stability. It has been reported that the oxygen flux for economically viable industrial application should be higher than 10 ml cm^{-2} min^{-1}.[7] One approach that can effectively improve the oxygen permeation rate is developing new membrane microstructures or geometries. The new membrane microstructures or geometries also can be fabricated using the materials with good stability to potentially enhance the membrane stability. In the past two decades, porous supported membranes and hollow fibre membranes had been developed. The complicated fabrication process and poor thermal stability of porous supported membranes have restrained their commercialization. Hollow fibre membranes have demonstrated high oxygen fluxes but the

mechanical strength is comparatively low. Thus, to develop a new membrane microstructure, which can be commercially viable, it has to meet following requirements: significantly improved oxygen flux, simple fabrication process, sufficient mechanical strength for handling and operation.

1.1 Significance of this study

A novel microchanneled membrane was developed in this study, which is a breakthrough in the design of membrane microstructures. The microchaneled membranes greatly increase oxygen separation rates from air compared with conventional dense membranes and supported membranes. This membrane microstructure owns excellent thermal compatibility and good mechanic strength. The simple fabrication process largely reduces the preparation time compared with supported membranes. The process can be easily scaled up to fit industrial requirements. The patented technology will promote the commercialization of ceramic membranes in oxygen production.

The novel membrane microstructure can be applied in many applications to achieve high efficiencies. The microchanneled membrane can be used as a membrane reactor in natural gas conversion industries. The oxygen required in such reactions can be naturally derived from air at the reaction temperature. It would greatly reduce the operation cost of natural gas conversion. Another promising application of the microchanneled membranes is CO_2 conversion. In microchanneled membranes, CO_2 can be electrolysed to be CO or co-electrolysed with water to form syngas. It could form a sustainable loop when CO_2 electrolysing in the microchanneled membranes couple with solar energy. The microchanneled membranes can be also designed as an oxygen pump with much smaller energy consumption, which is a portable oxygen supplier for medical purpose. Moreover, in other applications, such as solid oxide fuel cells, sodium batteries and hydrogen or CO_2 separations, microchanneled membranes are attractive as well because of the unique microstructure.

1.3 Objectives and outline of the thesis

The major objectives of this thesis were to develop a novel membrane microstructure and investigate and make full use of the advantages of the microchanneled membranes to improve oxygen flux. More specifically, this thesis includes the following studies:

- ✓ Developing a novel microchanneled membrane prepared by templated phase inversion; including the improvement of microchanneled structure on oxygen separation from air.

- ✓ Understanding the formation mechanism of microchannels in the phase inversion process; especially the effects of fabrication parameters on membrane micro structure to control the microchanneled structure.

- ✓ Further improving oxygen fluxes of the microchanneled membranes through using dual-phase membrane materials and applying catalysts.

- ✓ Investigating the advantages of the microstructure of microchanneld membranes for oxygen separaton from air.

According to the above outline, this thesis is comprised of seven chapters. Chapter 2 is the review of related literature in the area of oxygen permeation membrane and membrane fabrication. The experimental results and the discussions of the experimental results are presented in Chapters 3-6, which have been published, or will be submitted to journals for publication. In Chapter 7, the thesis will be concluded with some suggestions for future work.

Chapter 1: Introduction

Briefly introduce the oxygen separations membrane regarding a simple background and some advantages. The significance of this research is explained. The contents of this thesis are specifically presented.

Chapter 2: Literature review

This chapter firstly discusses the oxygen demands, current situation of oxygen production and applications of oxygen permeation membranes. The working principle of oxygen separations membrane is explained using a mathematical model. Finally, the different membrane microstructures for oxygen permeation are discussed in terms of advantages, disadvantages, fabrication methods and mathematic modelling.

Chapter 3: A microchanneled ceramic membrane for highly-efficient oxygen separation

A novel microchanneled ceramic membrane is presented including preparation and testing for oxygen separation from air. The oxygen permeation flux of microchanneled membrane is compared with that of other conventional membranes. It is confirmed that this structure significantly improves oxygen permeation rates.

Chapter 4: Microstructure control of oxygen permeation membranes with templated microchannels

In this chapter, the fabrication parameters of microchanneled membrane are studied to control membrane microstructure for the purpose of improving oxygen fluxes. It is found that the oxygen permeation rate is influenced by the microchannel structure.

Chapter 5: Improvement of oxygen permeation through microchanneled ceramic membranes

Two methods are applied to further improve oxygen flux of the microchanneled membrane in this chapter. One is using a dual-phase material to increase the ionic conductivity of the membrane. The other one is coating catalyst on the membrane surfaces and channel walls to enhance the surface kinetics.

Chapter 6: Investigation of microchannel influence in the oxygen permeation of microchanneled membranes

The advantages of the microchanneled membranes are investigated by comparing with dense membranes and supported membranes. The surface on microchannel wall contributes to

oxygen flux and it enables the microchanneled membranes enhance their mechanic strength by increase membrane thickness to some extent. Also, it greatly diminishes gas diffusion resistance compared with supported membranes.

Chapter 7: Conclusion

The overall conclusions of this thesis and the recommendations for future studies are summarized in this chapter.

1.4 References

1. *Energy Materials Coordinating Committe (EMaCC): 2001 Annual Technical Report*, U. S. Department of Energy Office of Science, 2002.
2. W. Castle, *International Journal of Refrigeration*, 2002, **25**, 158-172.
3. J. Schlaechter, U.S. Patent 4534346 1985.
4. C.-s. Chen, S.-j. Feng, S. Ran, D.-c. Zhu, W. Liu and H. J. M. Bouwmeester, *Angewandte Chemie International Edition*, 2003, **42**, 5196-5198.
5. A. Leo, S. Liu and J. C. D. d. Costa, *International Journal of Greenhouse Gas Control*, 2009, **3**, 357-367.
6. H. Stadler, F. Beggel, M. Habermehl, B. Persigehl, R. Kneer, M. Modigell and P. Jeschke, *International Journal of Greenhouse Gas Control*, 2011, **5**, 7-15.
7. K. Watenabe, M. Yuasa, T. Kida, Y. Teraoka, N. Yamazoe and K. Shimanoe, *Advanced Materials*, 2010, **22**, 2367-2370.

Chapter 2: Literature Review

2.1 Introduction

Oxygen plays important roles in industry and daily life. Statistics of the oxygen industry in the USA during part of the last century are shown in Figure 2-1. The oxygen industry scale was about 300-500 billions of cubic feet every year in the USA. It is believed that the oxygen industry will continuously expand due to the increasing demand from large scale clean energy technologies.[1-4] Typical oxygen consuming applications include metallurgical industry,[5] coal gasification,[6] natural gas reforming,[7, 8] waste water treatment,[9] medical and domestic health care.

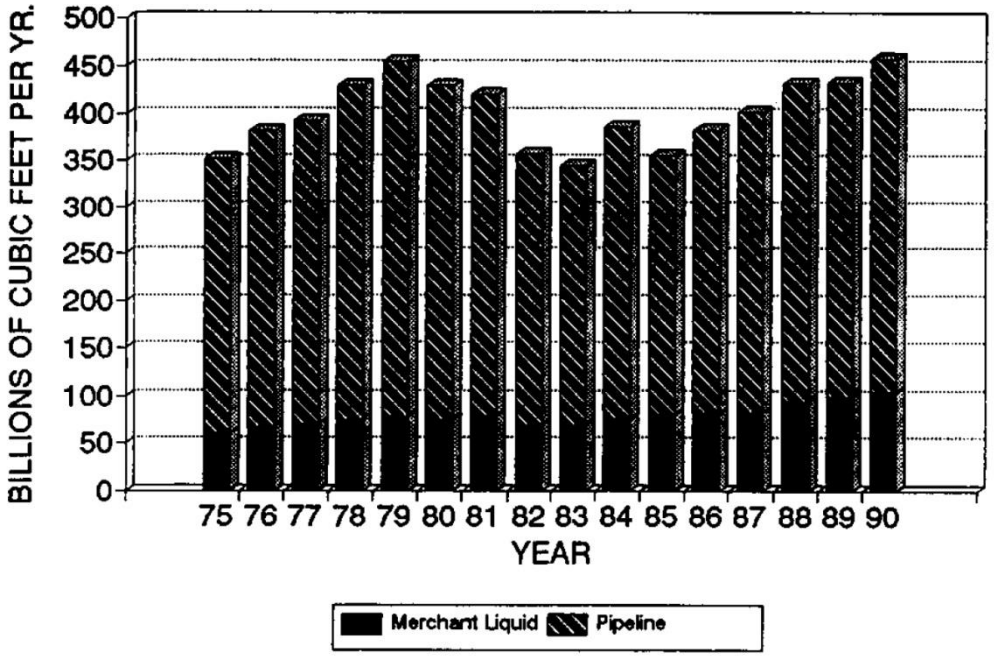

Figure 2-1. Oxygen production in USA during 1975-90.[10] (Reprinted with permission from Elsevier)

The commercialized methods to produce oxygen rely on three routes: cryogenic, pressure-swing adsorption (PSA) and membrane filtration. The cryogenic process can produce oxygen with high purity (>99 vol %).[11] It was generally designed for large scale oxygen plants with high capital costs and high energy consumption.[12] A PSA unit can produce oxygen with a purity above 90 vol % purity, and is preferable over the cryogenic process for small scale medical or domestic applications.[13, 14] The polymer membrane filtration method has a similar

mechanism to the PSA process, with oxygen adsorption-desorption in zeolites. This technology is used in the area of producing an enriched oxygen stream because of the relatively low purity of the generated oxygen.[15]

Theoretically, ceramic dense membranes for oxygen separation are based on oxygen ionic conduction in a solid phase without physical diffusion separation (if the tiny leakage from sealant is neglected). Thus, this method can produce ultra-high pure oxygen. This process needs to be operated at high temperatures (>600 °C) and uses chemical potential difference as the separation driving force. At high temperatures, the separation process could couple with many high temperature chemical reactions, such as natural gas reforming, coal gasification, oxyfuel combustion and solid oxide fuel cell operation. Oxygen separation using ceramic membranes potentially fits both small and large scale operation and has attracted significant research attention in recent years.

Two major issues impede the commercialization of oxygen separation using ceramic membranes: poor membrane stability and low oxygen flux rate. There is a dilemma in the selection of ceramic membrane materials for oxygen separation. The materials with high intrinsic oxygen permeation rate normally lack long term stability. For example, although $Ba_{0.5}Sr_{0.5}Co_{0.8}Fe_{0.2}O_3$ (BSCF) and $SrCo_{0.8}Fe_{0.2}O_3$ (SCF) are of very high oxygen permeation rates (>5 ml cm^{-2} min^{-1} at 900 °C), the stabilities of these two materials are poor, particularly when coupled with the operation of natural gas reforming.[16-18] Many researchers have attempted to improve membrane stability through developing new materials. However, the new materials developed for long term operation showed very small oxygen permeation rates, far less than the commercial requirement of oxygen permeation membrane (10 ml cm^{-2} min^{-1}).[19, 20] Another approach to improve the oxygen permeation rate is to optimize the geometries or micro structures of ceramic membranes. This approach would not be limited by materials and could potentially offset the deficiency of the materials with high stability but low oxygen permeation rate. Over the last three decades, many new membrane geometries and microstructures have been developed. The oxygen separation technology using ceramic membranes is approaching commercialization as the membrane performance is improved. The objective on this review is to understand the influences of oxygen permeation of membrane geometry and microstructure. Membrane fabrication and oxygen permeation mechanisms in different membranes will be also discussed.

2.2 Oxygen permeation mechanism through ceramic membranes

2.2.1 Modelling description of the oxygen permeation

Oxygen permeation through ionic conducting membranes is normally comprised of three steps: oxygen molecules decompose to oxygen ions, oxygen ions diffuse through the solid membrane and oxygen ions associate to oxygen molecules (Figure 2-2). Oxygen ions diffuse from oxygen rich side to oxygen lean side while electrons move in the opposite direction to maintain electrical neutrality. A typical model developed according to Wagner's theory is widely accepted to describe the oxygen permeation process in dense membranes.[21] For a mixed ionic/electronic conductor, the fluxes of the two charge carriers, oxygen ions and electrons, can be described using the following equations:[22, 23]

$$J_{O^{2-}} = -\frac{\delta_i}{4F^2}(\nabla\mu_i + 2F\nabla\varphi) \quad (1)$$

$$J_e = -\frac{\delta_e}{F^2}(\nabla\mu_e + 2F\nabla\varphi) \quad (2)$$

where $J_{O^{2-}}$ is the flux of oxygen ions, J_e is the flux of electrons, δ_i and δ_e are the conductivity of the oxygen ions and electrons, respectively, $\nabla\mu_i$ is the chemical potential difference of oxygen ions between the two sides of the membrane, and $\nabla\mu_e$ is the electrical potential difference between the two sides of the membrane, F is the Faraday constant and $\nabla\varphi$ is the electric potential difference between the two sides of the membrane.

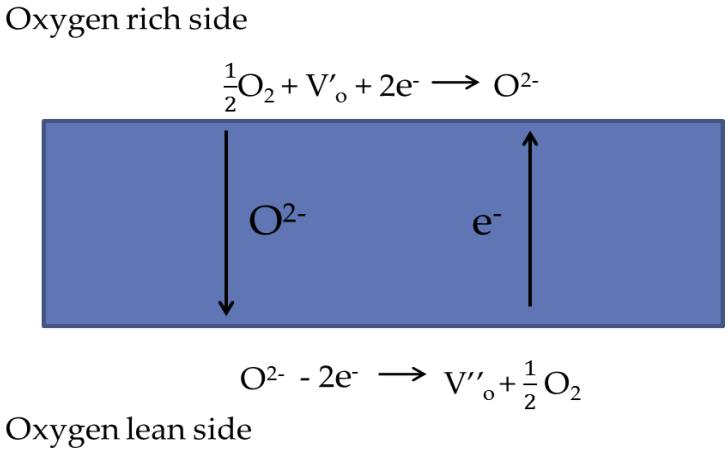

Figure 2-2. Oxygen permeation process.

According to Wagner's theory, the equations only describe the processes in steady state; therefore, one can have equations

$$2J_{O^{2-}} + J_e = 0 \tag{3}$$

and

$$\frac{1}{2}\nabla\mu_{O_2} = \nabla\mu_i - 2\nabla\mu_e \tag{4}$$

where $\nabla\mu_{O_2}$ is the chemical potential difference of oxygen molecules between the two sides of the membrane if the mixed conductor has very high electric conductivity, an electric field cannot build up. Therefore, $\nabla\varphi = 0$. Under these circumstances, a combination of equations 1 to 4 yields:

$$J_{O^{2-}} = -\frac{\delta_i\delta_e}{8F^2(\delta_i+\delta_e)}\nabla\mu_{O_2} \tag{5}$$

At steady state, the chemical potential can be correlated to the oxygen partial pressure in the gas phase. Thus,

$$J_{O_2} = -\frac{RT}{16F^2L}\int_{lnP''_{O_2}}^{lnP'_{O_2}} \frac{\delta_i\delta_e}{(\delta_i+\delta_e)}\, d\, lnP_{O_2} \tag{6}$$

where J_{O_2} is the oxygen flux (mol cm^{-2} s^{-1}), R is idea gas constant (Pa mol^{-1} K^{-1}), T is temperature (K), L is membrane thickness (cm), F is Faraday constant (C mol^{-1}) δ_i and δ_e are the conductivities of oxygen ions and electrons (S/cm), respectively and P''_{O_2} and P'_{O_2} are the oxygen partial pressures at the oxygen lean side and the oxygen rich side, respectively.

Equation (6) is known as Wagner equation that is used to describe the bulk diffusion of oxygen ions. However, in many cases, the bulk diffusion of oxygen ions is not the sole rate-limiting step. The descriptions of two surface reactions are also required. The surface reactions occurring on the membrane surfaces are shown below,[24, 25]

$$\frac{1}{2}O_2 + V_O^{\cdot\cdot} \xrightarrow{k_f/k_r} O_O^x + 2h^{\cdot} \qquad \text{(oxygen rich surface)} \tag{A}$$

$$O_O^x + 2h^{\cdot} \xrightarrow{k_r/k_f} \frac{1}{2}O_2 + V_O^{\cdot\cdot} \qquad \text{(oxygen lean surface)} \qquad \text{(B)}$$

where k_f and k_r are surface exchange coefficients of forward and reverse reactions, respectively, $V_O^{\cdot\cdot}$ is the lattice oxygen vacancy, O_O^x is the lattice oxygen and $h^{\cdot}$ is the lattice electron. In equilibrium, one can derive:

$$J_{O_2} = k_f P_{O_2}'^{0.5} C_v' - k_r \qquad (7)$$

$$J_{O_2} = k_r - k_f P_{O_2}''^{0.5} C_v'' \qquad (8)$$

where C_v' and C_v'' are the oxygen vacancy concentrations on the two surfaces of membranes. These two equations are based on assuming that reaction A and B are elementary reactions and taking the reaction orders as 0.5.

The reaction order relies on the determination of the nature of the elementary reactions in the process. Practically, there could be many sub-steps that are affected by these two reactions, such as gaseous oxygen mass transfer, oxygen adsorption and desorption, charge transfer.[26-29] The determination of reaction order, namely the power law between reaction rates to oxygen partial pressure, will be further discussed in 2.2.2.

One can also correlate the surface reactions and oxygen ion bulk diffusion in a global equation. According to the Einstein relation,

$$\delta_n = \frac{4F^2}{RT} C_v D_v \qquad (9)$$

where δ_n is the conductivity of a charge carrier, D_v is the oxygen vacancy diffusion coefficient, and C_v is the oxygen vacancy concentration. We set $\nabla\varphi = 0$ (ie, we assume that there is no electrical potential difference between the two membrane surfaces), and then integrate equation 1 and 9 yields

$$J_{O_2} = \frac{D_v}{2L}(C_v'' - C_v') \qquad (10)$$

By combining equations 7, 8 and 10, one can arrive at a unified equation to describe the whole oxygen permeation process.

$$J_{O_2} = \frac{\frac{k_r}{k_f}(P_{O_2}^{\prime\prime -0.5} - P_{O_2}^{\prime -0.5})}{\frac{1}{k_f P_{O_2}^{\prime -0.5}} + \frac{2L}{D_v} + \frac{1}{k_f P_{O_2}^{\prime\prime -0.5}}} \quad (11)$$

where $\frac{k_r}{k_f}(P_{O_2}^{\prime\prime -0.5} - P_{O_2}^{\prime -0.5})$ represents the driving force for oxygen permeation, in other words, the oxygen partial pressure corrected using surface reaction coefficients, $\frac{1}{k_f P_{O_2}^{\prime -0.5}}$ and $\frac{1}{k_f P_{O_2}^{\prime\prime -0.5}}$ which are known as resistances from surface reactions at the oxygen rich and lean sides, respectively. $\frac{2L}{D_v}$ can be considered as the resistance due to oxygen bulk diffusion.[24]

The diffusion coefficient and surface exchange coefficients are typically temperature dependent and can be described using the Arrhenius relation,[24, 25]

$$k_f = k_{f0}\exp(-\frac{E_f}{RT}) \quad (12)$$

$$k_r = k_{r0}\exp(-\frac{E_r}{RT}) \quad (13)$$

$$D_v = D_{v0}\exp(-\frac{E_D}{RT}) \quad (14)$$

where k_{f0}, k_{r0} and D_{v0} are pre-expotional factors, and E_f, E_r and E_D are activation energies for each step.

The surface exchange and bulk diffusion coefficients can be measured using oxygen isotopic exchange technology,[30-40] conductivity relaxation[41-44] or potential gradient measurement coupled with modelling fitting.[28, 45-47] The potential gradient measurement requires accurately identifying the rate-limiting step via modelling. However, the oxygen permeation is normally jointly rate-limited by both bulk diffusion and surface reactions when thin membranes are considered.[48] The last method, modelling regression, is largely dependent on the modelling concepts and experimental conditions. For example, for the same material of $La_{0.6}Sr_{0.4}Co_{0.2}Fe_{0.8}O_3$, researchers could have different regression values in terms of

activation energies and pre-exponential factor using modelling regression.[24, 25] It is also suggested that the coefficients measured by different methods are not comparable for the reasons given by Maier.[49] Maier states the difference could be due to experimental arrangements and conceptional errors.

2.2.2 Rate-limiting step of oxygen permeation

The rate-limiting step in the oxygen permeation process could vary with materials, temperature and operating conditions. A characteristic thickness defined by Bouwmeester was introduced to describe the rate-limiting step boundary between surface reactions and bulk diffusion.[50, 51]

$$L_c = \frac{D_v}{k_s} \tag{15}$$

where

$$k_s = \frac{k_f k_r}{k_f + k_r} \tag{16}$$

The physical meaning of L_c is that, if the membrane is thinner than the characteristic thickness, oxygen permeation tends to be more controlled by oxygen surface reactions while the oxygen permeation through a membrane which is thicker than the characteristic thickness tends to be more controlled by oxygen bulk diffusion. For a membrane which is much thinner than the characteristic thickness, further flux improvement cannot be gained by reducing the membrane thickness. When a membrane with a thickness close to L_c, the oxygen permeation will be jointly rate-limited by both surface reaction and oxygen bulk diffusion. L_c varies with temperature and material characteristics.[52] It should be noted that L_c is defined by tracer coefficients of surface exchange and bulk diffusion, in other words, it is only valid when no or small oxygen concentration gradient is present. Numerous studies have used the idea of a characteristic thickness to analyse the nature of certain materials since the concept was formed.[53-56] However, L_c cannot determine the exact role or proportion of surface reactions and oxygen bulk diffusion in understanding the rate-limiting step because within the region close to L_c , the oxygen permeation will be jointly controlled by surface reactions and oxygen

bulk diffusion. Furthermore, for many cases, the oxygen permeation was measured under a chemical potential gradient, under which conditions the concept of L_c is no longer valid.

Another way to identify the rate-limiting step is based on the power law index that describes a correlation between the oxygen partial pressure and oxygen bulk diffusion. For the conductivity of charge carriers in a membrane, it can be expressed by a power law relation defined by Wagner's theory:[21]

$$\delta_n = \delta_{n0} P_{O_2}^n \tag{17}$$

Assuming that only one charge carrier (oxygen ion or electrons) is dominant in oxygen bulk diffusion and lattice oxygen concentration difference equals the oxygen potential difference between membrane two sides, integration of equation 5 and 17 yield,

$$J_{O_2} = \frac{\beta}{L}(P_v''^n - P_v'^n) \tag{18}$$

where

$$\beta = \frac{RT\delta}{16F^2} \tag{19}$$

and P_v' and P_v'' are lattice oxygen concentrations on membrane surfaces at oxygen rich and lean sides, respectively, δ is the conductivity of a specific charge carrier, n is power law index. Although equation 18 only describes the oxygen bulk diffusion, the actual rate-limiting step can be estimated by the deviation from the power law index.[48, 57-61] There is no universal agreement on the value of power law index and n generally varies with different materials. One can use it to identify the rate-limiting step when the nature of the material is known. Otherwise, knowledge of n is insufficient to determine the rate-limiting step. For example, in supported or microchanneled membranes, an oxygen partial pressure gradient could occur along the axial direction of the microchannel array or porous support. During the oxygen permeation in those membranes, the elementary reactions are unknown as well as the rate limiting steps are generally related to more than one step. It is difficult to identify the power law index values for the oxygen permeation in those membranes.

In addition, the surface reactions can be described using the form of equation 18 as well,

$$J_{O_2} = \alpha(P'^{m}_{O_2} - P'^{m}_{v}) \quad \text{(Surface reaction at the oxygen rich side)} \tag{20}$$

$$J_{O_2} = \alpha(P''^{m}_{v} - P''^{m}_{O_2}) \quad \text{(Surface reaction at the oxygen lean side)} \tag{21}$$

where α is the surface reaction constant, m is the power law index. For different materials, the power law indices, n and m, are very different. For example, Bouwmeester et al. defined the n, m values to be 0.625 and 0.25 for erbia stabilized bismuth oxide.[62] Boukamp et al. measured the n value between 0.54 to 0.6 for bismuth based oxides using oxygen isotopic exchange technology.[63] Dou et al. reported an m value between 0.2 to 0.4 for lime stabilized zirconia.[64] Shiguang et al. obtained the n value 0.15 for $La_{0.2}Sr_{0.8}Co_{0.2}Fe_{0.8}O_3$ using modelling regression,[65] etc..

On the other hand, the Wagner equation also can also be modified as following:

$$J_{O_2} = -\frac{RT}{16F^2L^{\gamma}}\frac{\delta_i\delta_e}{(\delta_i+\delta_e)}\Delta\mu_{O_2} \tag{22}$$

where γ varys between 0 and 1. When $\gamma = 1$, the oxygen flux linearly changes with membrane thickness and it should only be rate-limited by ionic bulk diffusion. When $\gamma = 0$, oxygen flux is only related to the oxygen potential at the membrane surfaces, which is determined by the oxygen surface reactions.[51, 66] This method cannot be used for supported membranes and microchanneled membranes because the thickness (L) can be a variable during the oxygen permeation in such membranes.

Another method generally used to identify rate-limiting step is measuring activation energies of oxygen permeation.[24, 67] Based on the activation values, one can make a qualitative analysis of rate-limiting step. This is because the measurement in an oxygen permeation process can only show the activation energy of the rate-limiting step, which is appropriate for the rate limiting step analysis of supported membrane and microchanneled membranes. In many cases, oxygen permeation is not rate-limited by single step. Thus, the measured activation energy will be an integrated value which could only indicate that the oxygen permeation is jointly rate-limited by multi-steps in the process.[51, 52, 68] It is also believed that the oxygen permeation is rate-limited by bulk diffusion if the oxygen fluxes linearly change with membrane thicknesses. Table 2-1 summarizes the activation energies of oxygen permeation of different materials.

Determining the oxygen flux rate-limiting step could assist effective improvement of the oxygen permeation rate. If oxygen bulk diffusion dominantly controls the process, reducing membrane thickness is the most efficient method to improve its performance.[69, 70] In contrast, if the oxygen surface reactions are slower steps, the membrane surface kinetic can be improved by surface modifications, such as increasing membrane surface roughness,[71] coating catalysts [72, 73] or evolution layer.[74, 75] It has been reported noble metal catalysts, such as Ag, Pt and Pd can effectively improve the oxygen permeation rate.[72, 73, 76]

In fact, the improvement here represents the improvement of areal oxygen flux, and eventually, volumetric oxygen flux. A comparatively small scale oxygen plant or a unit in a process means less capital and operation investment because the ceramic membranes need a high temperature working environment. A high volumetric oxygen flux also provides the possibility that the oxygen separation can be modularized and suits from small scale to large scale industry. Among all the approaches to improve oxygen flux, changing membrane geometry is preferential because all the other approaches can be applied afterwards.

Table 2-1. Activation energies and rate-limiting steps of oxygen permeation.

Materials	Temperature range (°C)	Thickness (mm)	Activation energy (kJ mol^{-1})	Rate-limiting step	Ref.
$SrCo_{0.8}Fe_{0.2}O_{3-\delta}$	625-775	1	92	Bulk diffusion	77
$Ba_{0.5}Sr_{0.5}Fe_{0.8}Zn_{0.2}O_{3-\delta}$	820-950	1.15	53	Bulk diffusion	78
$La_{0.4}Sr_{0.6}Co_{0.2}Fe_{0.8}O_{3-\delta}$	750-900	>1.25	79.8	Bulk diffusion	52
		0.62	103	Jointly controlled	
$Ba_{0.5}Sr_{0.5}Co_{0.8}Fe_{0.2}O_{3-\delta}$	600-775	1.8	72.6	N/A	79
	775-950		40.9		
$BaCe_{0.2}Fe_{0.8}O_{3-\delta}$	800-950	1	62.2	Bulk diffusion	80
$La_{0.2}Sr_{0.8}Cu_{0.4}Co_{0.6}O_{3-\delta}$	750-960	0.8	109	Bulk diffusion	81
$Bi_{1.485}Y_{0.5}Cu_{0.015}O_{3-\delta}$	650-900	2	80	Bulk diffusion	82
$BaTi_{0.2}Co_{0.5}Fe_{0.3}O_{3-\delta}$	700-950	1	85.4	N/A	83
	600-700		156.1		
$La_{0.6}Sr_{0.4}Co_{0.2}Fe_{0.8}O_{3-\delta}$	875-975	1.65	115	Bulk diffusion	24
	750-875		191	Surface reaction	
$SrFe_{0.67}Co_{0.33}O_{3-\delta}$	900-1000	1.24	96	Jointly controlled	68
$La_{0.3}Sr_{0.7}CoO_{3-\delta}$	800-1050	1.15	57	Jointly controlled	51
$La_{0.6}Sr_{0.4}Fe_{0.8}Co_{0.2}O_{3-\delta}$	800-900	1	118	Surface reaction	67

2.3 Membrane geometries

2.3.1 Disk and tubular membranes

Conventionally oxygen permeation membranes in laboratories are shaped into disk or tubular form. The disk membrane is fabricated using a static pressure method. It is widely used because of the simple fabrication process. The oxygen fluxes using different materials are listed in Table 2-2. Tubular membranes are made by an extrusion method, which is comparatively complex. The formed tubes normally have outer diameter more than 5 mm and thickness more than 1 mm.[84, 85]

The methods to improve oxygen fluxes for the disk and tubular membranes are limited. Since the membranes are thick (above 1 mm in thickness), the improvement of oxygen flux can only rely on changing materials. Among all the oxygen ionic conducting materials, making dual phase membranes is the easiest method. The most common dual-phase material is the mixture of materials with fluorite and perovskite structures, which aims to improve the oxygen permeability. According to equation 3, the electronic flux must match the ionic flux in oxygen permeation. Thus, oxygen permeation requires both high ionic and electronic conductivities. The electronic and ionic transference number can be expressed using conductivities:

$$t_i = \frac{\delta_i}{\delta_i + \delta_e} \tag{23}$$

and

$$t_e = \frac{\delta_e}{\delta_i + \delta_e} \tag{24}$$

where t_i and t_e are ionic and electronic transference number, respectively.

Table 2-2. Oxygen fluxes of disk membranes

Materials	Thickness (mm)	Temperature (°C)	Oxygen fluxes (ml cm^{-2} min^{-1})	Ref.
$LaBaCo_2O_{5+\delta}$	0.7	900	0.08	86
$PrBaCo_2O_{5+\delta}$	0.7	900	0.67	
$NdBaCo_2O_{5+\delta}$	0.7	900	0.59	
$SmBaCo_2O_{5+\delta}$	0.7	900	0.17	
$GdBaCo_2O_{5+\delta}$	0.7	900	0.13	
$Ba_{0.5}Sr_{0.5}Fe_{0.8}Zn_{0.2}O_{3-\delta}$	1.45	950	0.35	20
$La_{0.15}Sr_{0.85}Ga_{0.3}Fe_{0.7}O_{3-\delta}$	1	950	0.09	
$La_{0.2}Sr_{0.8}Co_{0.2}Fe_{0.8}O_{3-\delta}$	1	850	0.46	65
$La_{0.1}Sr_{0.9}Co_{0.9}Fe_{0.1}O_{3-\delta}$	1	900	2.8	87
$Ba_{0.5}Sr_{0.5}Co_{0.8}Fe_{0.2}O_{3-\delta}$	1	900	1.396	88
$Ba_{0.5}Sr_{0.5}Co_{0.8}Fe_{0.2}O_{3-\delta}$	1	800	1.8	89
$La_{0.4}Sr_{0.6}Co_{0.2}Fe_{0.8}O_{3-\delta}$	0.8	900	1.8	52
$SrCo_{0.4}Fe_{0.6}O_{3-\delta}$	1.78	950	0.6	90
$SrCo_{0.4}Fe_{0.55}Zr_{0.05}O_{3-\delta}$	1.78	950	0.46	
$BaCo_{0.7}Fe_{0.2}Nb_{0.1}O_{3-\delta}$	1	900	1.7	91
60 wt% $Ce_{0.8}Gd_{0.2}O_{2-\delta}$ & 40 wt% $PrBaCo_{0.5}Fe_{1.5}O_{3-\delta}$	1	925	0.35	92
$La_{0.6}Sr_{0.4}Co_{0.2}Fe_{0.8}O_{3-\delta}$	0.9	950	0.42	93
$La_{0.6}Sr_{0.4}Ti_{0.2}Fe_{0.8}O_{3-\delta}$	1.6	950	0.17	94
$BaBi_{0.4}Co_{0.2}Fe_{0.4}O_{3-\delta}$	1.5	925	0.8	95
$SrFe_{0.95}W_{0.05}O_{3-\delta}$	1	950	0.22	96

Generally, the ionic conductivities of fluorite materials are much higher than perovskite materials while the electronic conductivities of fluorite materials are very low. For example, the oxygen ion transference numbers of $Gd_{0.2}Ce_{0.8}O_{2-\delta}$ (GDC, fluorite structure) are close to 1 in the temperature range 850-950 °C and one can even roughly treat it as a pure oxygen ionic conductor.[97] In contrast, the ionic conductivity and electronic conductivity of $La_{0.6}Sr_{0.4}Co_{0.2}Fe_{0.8}O_{3-\delta}$ (LSCF, perovskite structure) are 0.0018 and 178 S/cm at 850 °C, respectively, which means the electron transference number of LSCF is close to 1 and it is almost an electron conductor.[98] The oxygen permeation rate of GDC membrane is therefore very small because of the low electronic conductivity.[99, 100] Thus, one can mix two materials as dual-phase membrane to balance the conductivities and improve oxygen permeation rate.

2.3.2 Porous supported membranes

In conventional ceramic membranes for oxygen permeation, oxygen ions diffuse through lattice defects. The membrane is a dense body having a thickness of 1 mm to maintain enough mechanical strength for handling. This solid diffusion through a long distance is considered as the rate-limiting step in most cases. Porous supported membranes had been developed targeting this problem. The porous supported membrane is composed of a thin dense layer sitting on a comparatively thick porous support (generally made by same material). The typical structure of the membrane cross section is shown in Figure 2-3.

2.3.2.1 Fabrication and characterization of supported membrane

Porous supports can be prepared using the same method as disk membrane preparation. Ceramic powder is firstly mixed with organic pore former and organic binding by ball milling. Starch or carbon fibre is normally selected as pore former and ethylcellulose or polyvinyl alcohol can be the organic binder since they can be completely burned off during sintering. Pores will be formed by removing the pore former during heat treatment[101]. Depending on the type, particle size and content of the pore former, the pore microstructure and porosity will be changed. Figure 2-3 shows the pore microstructures made by using different pore formers.

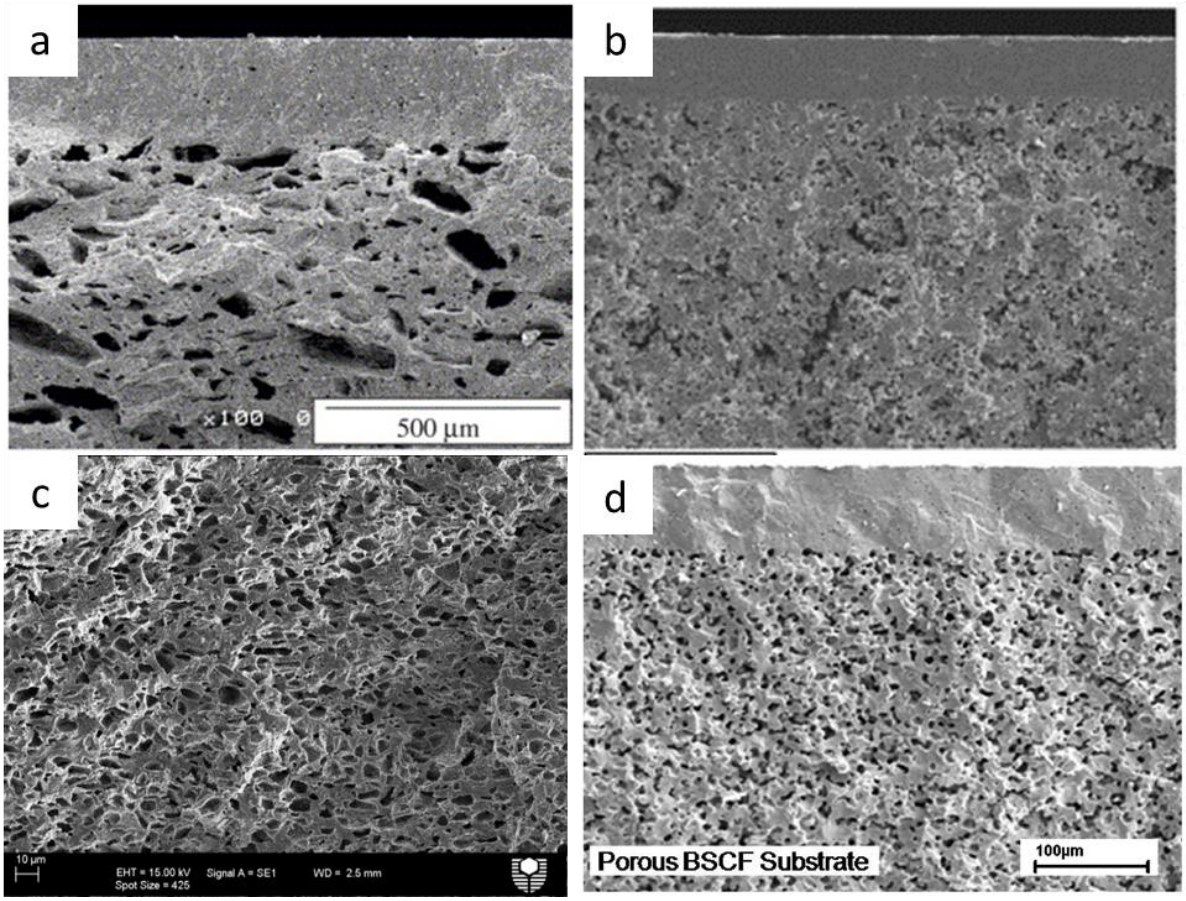

Figure 2-3. $SrCo_{0.5}Fe_{0.5}O_3$ porous support fabricated using 2.5 wt % carbon fibres with the diameter of 7 µm (a),[102] $La_{0.6}Sr_{0.4}Co_{0.2}Fe_{0.8}O_3$ porous support fabricated using 20 wt % rice starch with particle sizes of 2-8 µm (b)[103] and 15 wt% potato starch (c) and $Ba_{0.5}Sr_{0.5}Co_{0.8}Fe_{0.2}O_3$ porous support fabricated by using 15 wt % corn starch with particle sizes of 2-30 µm (d).[104] (Reprinted with permission from Elsevier)

Co-pressing is a common method to integrate the porous and dense layer.[102] Firstly, a certain amount of ceramic powder is put into a mould and flattened with gentle pressure to make a supporting layer. The mixture without pore former is then placed above the flattened layer and co-pressed under a specific pressure. Finally, the resulting raw membrane is sintered at high temperatures to densify the top layer. Although this method is easy to operate, it may not always make the dense layer very thin because it is difficult to control the uniformity of the top powder layer.

In contrast, tape-casting can make the dense layer with excellent uniformity and the prepared membranes show good reproducibility.[104] This method starts with slurry preparation. Ceramic powder is mixed with a dispersant (Duramax 3005), a pore former and water.[105] There is no

pore former applied if the slurry is prepared for the dense layer. All the slurries need to be degased under vacuum to remove bubbles. Dense layer slurry is firstly tape casted in the mould with a required thickness followed by a drying step and the porous layer slurry is then cast as above, followed with drying and high temperature sintering.[103]

Another method to make a supported membrane is slip casting. This method is actually based on the same principle as tape-casting. The first step is the fabrication of a porous support using one of the processes mentioned above (either pressing or tape-casting). The prepared porous support needs to be pre-sintered in order to match the shrinkage of the dense layer. A ceramic suspension slurry is prepared by mixing ceramic powder, dispersant and solvent together. A solvent with a high wettability is preferred. Then, the slurry is coated onto the porous support by slip casting;[106,107] this may be repeated for a few times, followed by high temperature sintering.

The most common problem in the preparation of porous supported membrane is the different thermal expansion and shrinkage between the two layers during high temperature sintering.[108] It could cause membrane cracking and deformation. In a study by Schulze-Kuppers, et al, the curvature of a porous supported membrane after sintering was clearly observed.[109] Moreover, the oxygen permeation of a porous supported membrane is highly correlated to the porosity and inner connection of the porous support.[109] The process that manufactures the porous supported membrane with optimized pore structure and cracking/deformation-free body takes a long time to optimize.

2.3.2.2 Modelling description of oxygen permeation in a porous supported membrane

In a porous supported membrane, oxygen permeation is generally not rate-limited by only one step because the reactions occur not only at a plane interface. Chang et al. estimated the contribution of surface reactions to overall oxygen permeation by model fitting and showed that the oxygen permeation in $SrCo_{0.4}Fe_{0.5}Zr_{0.1}O_3$ coated with porous layer was jointly controlled by bulk diffusion and surface reaction.[75]

The porous supported membrane can be either symmetric or asymmetric, which means the porous support can be attached on one side or both sides. The porous support offers two potential routes for oxygen flux, as shown in Figure 2-4. One is that the gaseous oxygen

diffuses through pores to the dense layer. The other one is that oxygen ions form on the surface of the pore walls and then migrate via the pore wall to the dense layer surface beneath the pores. Eventually, the oxygen ions diffuse through a thin dense layer which is much shorter than oxygen diffusion in a dense membrane.

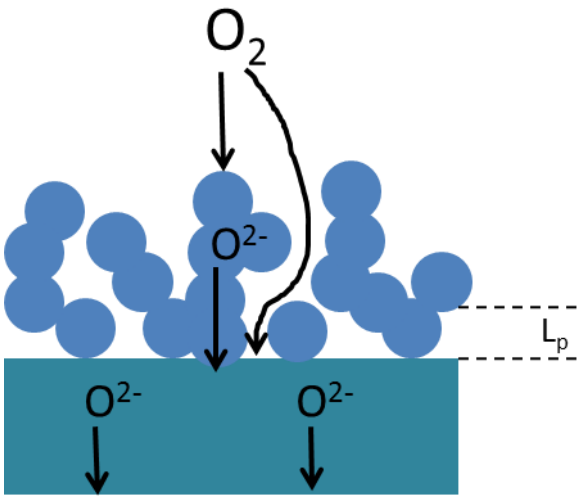

Figure 2-4. Oxygen permeation paths in porous supported membrane. Oxygen diffuse through white area (pores), oxygen ions diffuse through blue area (solid).

In oxygen molecules diffusion within pores, three types of mechanisms need to be considered: Knudsen diffusion ($\lambda/D_p > 10$), molecular diffusion ($\lambda/D_p < 0.01$) and transition region diffusion ($0.01 < \lambda/D_p < 10$), where λ is the mean free path of oxygen molecules and D_p is the pore size of the porous support.[110] Generally, the gas diffusion in pores can be divided into two cases, molecular diffusion dominant or a combination of molecular diffusion and Knudsen diffusion. Chang et al. described gas diffusion in a porous support mainly dominated by molecular diffusion based on Fick's diffusion law.[110]

$$J_{O_2,gas} = \frac{\varepsilon D_{O_2N_2}}{RT\tau}\frac{dP_{O_2}}{dL} \quad (25)$$

where $J_{O_2,gas}$ is the oxygen flux through gas phase diffusion, $D_{O_2N_2}$ is the oxygen diffusion coefficient in a N_2-O_2 binary system, L is the thickness of the porous support, ε is the porosity of the porous support and τ is tortuosity of the pores. Van Hassel also described gas diffusion in a porous support using the dusty gas model (DGM), which is based on joint control of Knudsen diffusion and molecular diffusion.[111]

$$J_{O_2,gas} = \frac{\varepsilon}{RT\tau} \frac{1}{\frac{1}{D_{kn}} + \frac{1-x_{O_2}}{D_{O_2N_2}}} \frac{dP_{O_2}}{dL} \quad (26)$$

where D_{kn} is the Knudsen diffusion coefficient of oxygen, τ is tortuosity of the porous support, x_{O_2} is the oxygen mole fraction at the interface between the porous support and the dense layer. The Knudsen diffusion coefficient is given by:

$$D_{kn} = \frac{2}{3} r \sqrt{\frac{8RT}{\pi M_{O_2}}} \quad (27)$$

where r is the pore radius, M_{O_2} is the molecular weight of oxygen. The tortuosity τ represents the increased ratio of diffusion distance due to the tortuous porous support. It has been used in almost all the mass transfer models in porous media to predict the mass transfer with different boundary conditions, such as the Stefan-Maxwell model (SMM), the Binary Friction model (BFM) and the conventional Fick's model. However, the evaluation of tortuosity is still controversial. Yasemin et al. compared DGM, SMM and BFM models in an SOFC anode system and found that those models had excellent agreement to the prediction of a H_2-H_2O-Ar ternary system unless the tortuosity of the porous support is severe.[112]

In any surface of the porous support, oxygen flux must match the sum of oxygen diffusion through the porous support and the oxygen exchanged on the dense layer. Such a circumstance was interpreted by Van Hassel using following differential equations.[111]

At the oxygen rich side, the oxygen exchange on the dense layer can be described as:

$$\frac{dJ_{O_2,rs}}{dL_{pr}} = \varepsilon k_f P'^m_{O_2} \frac{\mu_g - \mu'_s}{RT} \quad (28)$$

where L_{pr} is the characteristic length at the oxygen rich side, μ_g and μ'_s are the oxygen chemical potentials in the gas phase and solid phase at the oxygen rich side, respectively. The oxygen diffusion through the porous support can be described as:

$$J_{O_2,rb} = -\frac{1-\varepsilon}{\tau} \frac{\delta_i}{16F^2} \frac{d\mu_s}{dL_{pr}} \quad (29)$$

At the oxygen lean side, the oxygen ions would continuously exchange between the solid phase and the gas phase. Thus, the oxygen exchanged on the dense layer can be described as:

$$\frac{dJ_{O_{2,ls}}}{dL_{pl}} = \varepsilon k_r P''^{m}_{O_2} \frac{\mu''_s - \mu_g}{RT} \tag{30}$$

where L_{pl} is the characteristic length at the oxygen lean side, μ''_s is the oxygen chemical potential in the solid phase at the oxygen lean side. The oxygen diffused through the porous support can be described as:

$$J_{O_{2,lb}} = -\frac{1-\varepsilon}{\tau}\frac{\delta_i}{16F^2}\frac{d\mu_s}{dL_{pl}} \tag{31}$$

Oxygen flux through the dense layer can be described by modifying equation 22:

$$J_{O_{2,ds}} = \frac{\delta_i}{16F^2}\frac{\Delta\mu_s}{L_s} \tag{32}$$

where L_s is the thickness of the dense layer and assume the electrical conductivity of the material is much higher than ionic conductivity. Thus, we could have overall equations describing the oxygen permeation at oxygen rich and lean sides, respectively.

At the oxygen rich side:

$$\frac{\delta_i}{16F^2}\frac{\Delta\mu_s}{L_s} = \varepsilon k_f P'^{m}_{O_2} \frac{\mu_g - \mu'_s}{RT} - \frac{1-\varepsilon}{\tau}\frac{\delta_i}{16F^2}\frac{d\mu_s}{dL_{pr}} \tag{33}$$

At oxygen lean side:

$$\frac{\delta_i}{16F^2}\frac{\Delta\mu_s}{L_s} = \varepsilon k_r P''^{m}_{O_2} \frac{\mu''_s - \mu_g}{RT} - \frac{1-\varepsilon}{\tau}\frac{\delta_i}{16F^2}\frac{d\mu_s}{dL_{pl}} \tag{34}$$

To solve those equations, the oxygen pressure drop in the porous support gas phase was neglected:

$$\mu_g = RTlnP_{O_2} \tag{35}$$

The pressure drop in the gradually changing structure of a porous support applied at the oxygen lean side is not mentioned here, because this structure was not widely used in porous supported membranes for oxygen permeation, due to the complexity of fabrication.

It is noted that the concept of a characteristic length was used in the modelling above. The characteristic length is defined as a linear distance away from the interface between the porous support and the dense layer (Figure 2-4).[113, 114] The oxygen surface exchange current decreases rapidly along the axial direction that is away from the interface of porous support and dense layer. Characteristic length represents that the solid surface far away from the characteristic length contributes negligible oxygen flux. This is because when oxygen bulk diffusion is much slower than the surface reaction, the oxygen ionic diffusion from the surface far away from the dense layer interface is too slow, and thus, by the surface away from the interface of porous support and dense layer, the contribution of oxygen flux becomes smaller and smaller. Physically, it also indicates that, in idea condition (oxygen partial pressure in gas phase remains constant), the most effective surface for oxygen permeation in supported membranes should be the interface between the porous support and the dense layer. The characteristic length was defined using following equation:

$$L_p = \left(\frac{1-\varepsilon}{\tau}\frac{L_c}{S}\right)^{0.5} \quad (36)$$

where L_p is the characteristic length, L_c is the characteristic thickness, S is the specific surface area per unit volume. According to equation 36, the characteristic length would decrease with an increase of the specific surface area of the porous support; in other words, the porous support with smaller pore size would have a thinner characteristic length scale. However, the large specific surface area (small pore size) will have large exchange current density due to more active surface area, and therefore, reduce the resistance of surface reaction.[114, 115]

Most modelling descriptions are based on one boundary condition that the oxygen pressure drop in the porous support was neglected and therefore, the potential drop in the porous support was also neglected. In an ideal porous structure, the pores are interlinked to facilitate gas diffusion from the entrance of the porous support to the porous support-dense layer interface. However, in most cases, the porous supports do not have an ideal structure.[116] A study using X-ray computer tomography technology showed that in their porous supports, the

majority of pores could not be interconnected.[117] It also has been showed that the non-interconnected pores overwhelmingly exist in porous support when less than 20 vol% graphite was used as pore former in a tape casting process for the preparation of $La_9Sr_1Si_6O_{26.5}$/NiO porous supports.[118] The non-ideal porous structure could be the main reason creating deviation between the experimental data and modelling. X-ray computer tomography technology (XCT) and electron back-scattered diffraction (EBSD) technologies would be helpful to identify the porosity, tortuosity and pore size distribution of porous supports.[119]

2.3.3 Hollow fibre membranes

Since polymeric hollow fibre membranes were invented last century, most commercial interests have concentrated on bioseparations,[120] drinking water purification,[121, 122] wastewater treatment [123, 124] and gaseous separations.[125-128] The most common technique to fabricate those membranes is phase inversion.

Kang Li first integrated the phase inversion process with inorganic oxygen separation membranes, and expanded the applications to high temperature gas separations,[129, 130] membrane reactors [131-134] and intermediate temperature solid oxide fuel cells (SOFCs).[135-137] Compared with conventional dense disk membranes, the inorganic hollow fibre membranes made by the phase inversion method show many advantages, such as very thin walls (<300 μm) to reduce ion diffusion distance, large volumetric surface area and much better thermal shock resistance. It also had been mentioned that the inorganic hollow fibre membrane can be sealed at both ends using low temperature sealant.[133]

The easy management of sealing had been shown in Tan's study. A hollow fibre module composed of a few fibres was located in a tubular furnace with one end sealed by organic sealant; the organic sealant was located in thermal insulator and far away from high temperature zone. A temperature gradient was observed along the axis of the hollow fibre module, where the high temperature zone was kept at 1000 °C while it was only less than 400 °C 10 cm away from the high temperature zone.[138, 139] Another method to make the hollow fibre into a U-shape, and simply leave the bottom part in a high temperature zone, while the gas inlet and outlet are at low temperature for sealing.[140, 141]

Hollow fibre membranes achieved the highest oxygen flux among all membranes with different geometries. The oxygen fluxes using hollow fibre membrane have been summarized in Table 2-3. The oxygen permeation through hollow fibre membranes embedded with finger-like pores includes multiple surface reactions, as shown in Figure 2-5. There is no study that reports the influencing of finger-like pores on oxygen permeation. The only explanation of high oxygen flux is attributed to the thin membrane wall.

Table 2-3. Oxygen fluxes of hollow fibre membranes.

Materials	**Wall thickness (μm)**	**Temperature (°C)**	**Oxygen flux (ml cm^{-2} min^{-1})**	**Ref.**
$Ba_{0.5}Sr_{0.5}Co_{0.8}Fe_{0.2}O_{3-\delta}$	240	950	11.3	142
$BaZr_xCo_yFe_zO_{3-\delta}$	216	900	7.6	143
$La_{0.6}Sr_{0.4}Co_{0.2}Fe_{0.8}O_{3-\delta}$	307	900	1.38	144
$Ba_{0.5}Sr_{0.5}Co_{0.8}Fe_{0.2}O_{3-\delta}$	440	950	5	145
$La_{0.6}Sr_{0.4}Co_{0.2}Fe_{0.8}O_{3-\delta}$	190	1000	4.5	146
$La_{0.6}Sr_{0.4}Co_{0.2}Fe_{0.8}O_{3-\delta}$	380	1000	2.19	147
$SrCo_{0.9}Nb_{0.1}O_{3-\delta}$	280	900	3.9	148
$La_{0.7}Sr_{0.3}FeO_{3-\delta}$	220	1000	1.75	149
$BaZr_xCo_yFe_zO_{3-\delta}$	170	950	5	150

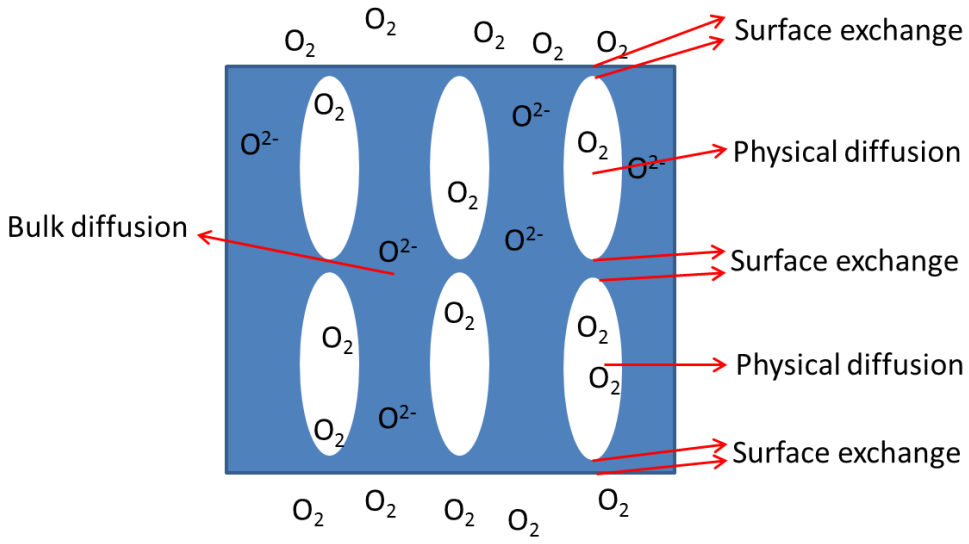

Figure 2-5. Oxygen permeation in hollow fibre membrane with symmetric microchannels. Hollow fibre membranes are in a tubular shape and this graph only shows the cross section of a single wall of hollow fibre.

2.3.3.1 Fabrication and micro structure control of hollow fibre membranes

The fabrication of ceramic hollow fibre membranes starts with slurry preparation. Generally, the slurry is composed of ceramic powder, polyethersulfone (PESF, Radel A-300), polyvinylpyrrolidone (PVP, MW=40000) and 1-methyl-2-pyrrolidinone (NMP); all the organic additives will be burned off in the following sintering process. It had been reported that the sulfur from PESF could react with perovskite and form sulfates during high temperature sintering.[151] Accordingly, some researchers fabricated hollow fibre using sulfur-free polymer binder. However, the microchannelled structures were not clear or even disappeared due to the different pore formation behaviour during the phase inversion process.[152-154]

The phase inversion extrusion process is shown in Figure 2-6. The ball milled slurry was loaded in the extrusion mould after degasing to remove bubbles. For single layer hollow fibre extrusion, only one kind of slurry is required, the slurry is extruded by pressure through the middle orifice while internal coagulant flows through the central orifice (Figure 2-6b and c). The slurry will be solidified when it contacts with internal and external coagulants to form solid fibres. If multi-layer hollow fibre is required, another slurry made by different ceramic materials can be extruded through the outer orifice. Thus, by modifying extrusion mould to

multiple orifices, one could have hollow fibres with dual-layer or even triple layers.[135, 136, 155-157] Jin's group also fabricated multichannel hollow fibre using a mould with 4 orifices (Figure 2-7g).[158]

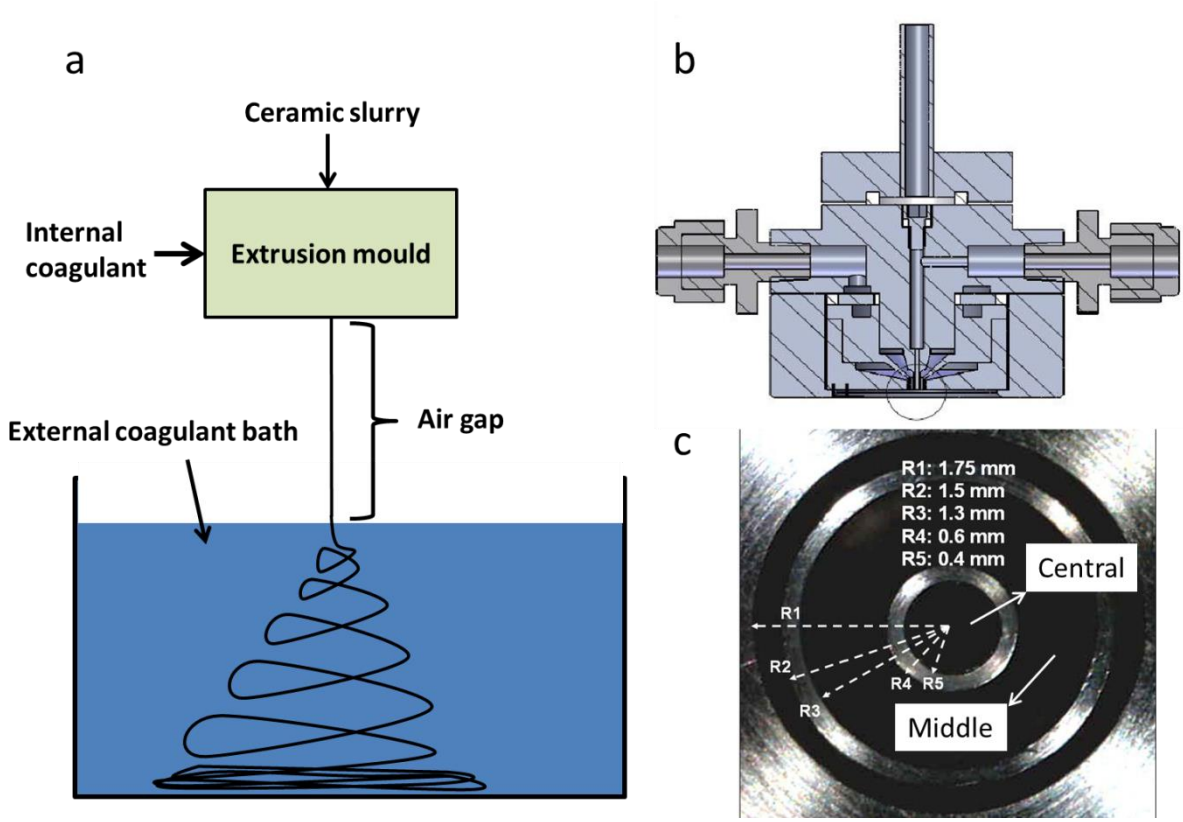

Figure 2-6. Graphic illustration of a) The hollow fibre phase inversion process, b) extrusion mould and c) triple orifice spinneret for dual-layer ceramic membrane co-extrusion (b and c are copied from).[159] (Reprinted with permission from Elsevier)

After phase inversion, the raw hollow fibres contain two kinds of pore structures, sponge-like pore and finger-like pore. The sponge-like pore would disappear after high temperature sintering and leave a hollow fibre with dense surfaces on both sides. Thus, the ceramic hollow fibre membranes generally contain internal finger-like pore.

During the phase inversion extrusion process, the morphology of hollow fibres can be controlled by adjusting these parameters: slurry components, air gap, internal coagulant composition and extrusion pressure (extrusion speed).[160] For example, hollow fibres with symmetric structure that were composed of two groups of microchannels sandwiched by three dense layers can be obtained using water as both internal and external coagulants and

certain air gap lengths (Figure 2-6a).[144, 161, 162] However, the hollow fibre structure tended to be asymmetric when the air gap was increased, and it had only one group of finger-like pore left when the air gap increased to 150 mm (Figure 2-7b-d).[163-165] Zhang et al. made highly asymmetric hollow fibre with only one group of microchannels by using water and ethanol as internal and external coagulants, respectively.[166] In addition, the microchannelled structure in hollow fibre membrane would also change with internal coagulant components.[167] One could have ultrathin hollow fibres (<200 μm) with one side surface open. As shown in Figure 2-7e and f, the hollow fibre contains only one group of microchannels and all the channels are open to inner side. It was achieved by using an internal coagulant solution with very high NMP content.[146, 167-169] The ultrathin hollow fibres with open surface can also be achieved using acid to remove the dense skin layer after sintering of the raw membranes.[170]

2.3.3.2 Phase inversion mechanism

The phase inversion method was initially developed for polymer membrane fabrication. To better understand the mechanism of pore structure formation in phase inversion, it is important to understand pore structure formation in polymer membrane. Phase inversion is a process that converts a one phase polymer solution into a two phase system including a solid phase and a liquid phase. The solid phase is constructed by solidifying polymer while the pore structure is formed by the liquid phase.[171] The phase inversion can be achieved using different processes, such as vapour induced precipitation,[172] immersion into a precipitation bath and volatile solvents.[173] The second process, immersion into a precipitation bath, has been used to make ceramic hollow fibre membranes because it is fast and convenient.

The precipitation of polymer is related to the solubility of polymer in the non-solvent. It can be illustrated in a ternary phase diagram (Figure 2-8). In the PES-H_2O-NMP system, if the water concentration passes through the precipitation curve, the polymer will precipitate. Otherwise, the system could be either in a stable miscible solution or an unstable transition state. Thus, the diffusion rate of water into the polymer solution results in either instantaneous or delayed precipitation of polymer. A proposed two-step mechanism divides the formation process of microchannels into initiation and growth.[174] In the NMP-PESF-water system, the surface of the polymer solution first contacts with water and forms a skin-layer because the ternary system immediately passes through the precipitation curve. The thickness of the skin layer keeps increasing until the water diffusion into the sub-layer is

restrained. This causes delayed precipitation of the polymer sub-layer. The water droplets diffusing through the skin-layer to the sub-layer become nuclei, which are responsible for the initiation of microchannels. Then, a liquid-liquid phase separation will be induced by the nuclei, forming a polymer-rich phase and a polymer-poor phase. As the water concentration increases in the polymer-rich phase by the convection between water and NMP, the region immediately passes over the precipitation curve and the phase is solidified. Otherwise, a continuous phase separation will keep increasing the region of polymer-poor phase, growing finger-like pore. This mechanism had been widely accepted by researchers.[175-177]

In this process, the skin layer is critical for the formation of finger-like pore. The skin-layer restrains the subsequent water diffusion because the formation of finger-like pore relies on water diffusional flows rather than convective flows and an instantaneous demixing is responsible for the skin layer formation.[171, 176] Thus, a good insolubility between polymer and non-solvent as well as good miscibility between the solvent and non-solvent are preferable for the instantaneous demixing. After that, the microchannels are formed by the rapid convection of solvent and non-solvent, as was confirmed by Guillen using high speed camera.[178] A skin layer was formed before microchannel initiation. After immersing the polymer solution in a water bath for 1 second, the finger-like pore had formed to lengths of more than 100 μm.[178] The various miscibilities are summarized in Table 2-4. The miscibility parameter δ has been divided into a dispersive term δ_d ($mPa^{0.5}$), a polar term δ_p and a hydrogen bond term δ_h. It can be calculated by using following equation:[179]

$$\delta = \sqrt{\delta_d^2 + \delta_p^2 + \delta_h^2} \qquad (37)$$

The large miscibility difference between two solvents indicates a large driving force of mixing. Thus, it can be concluded that water is a strong non-solvent that is favourable to the formation of finger-like pore.

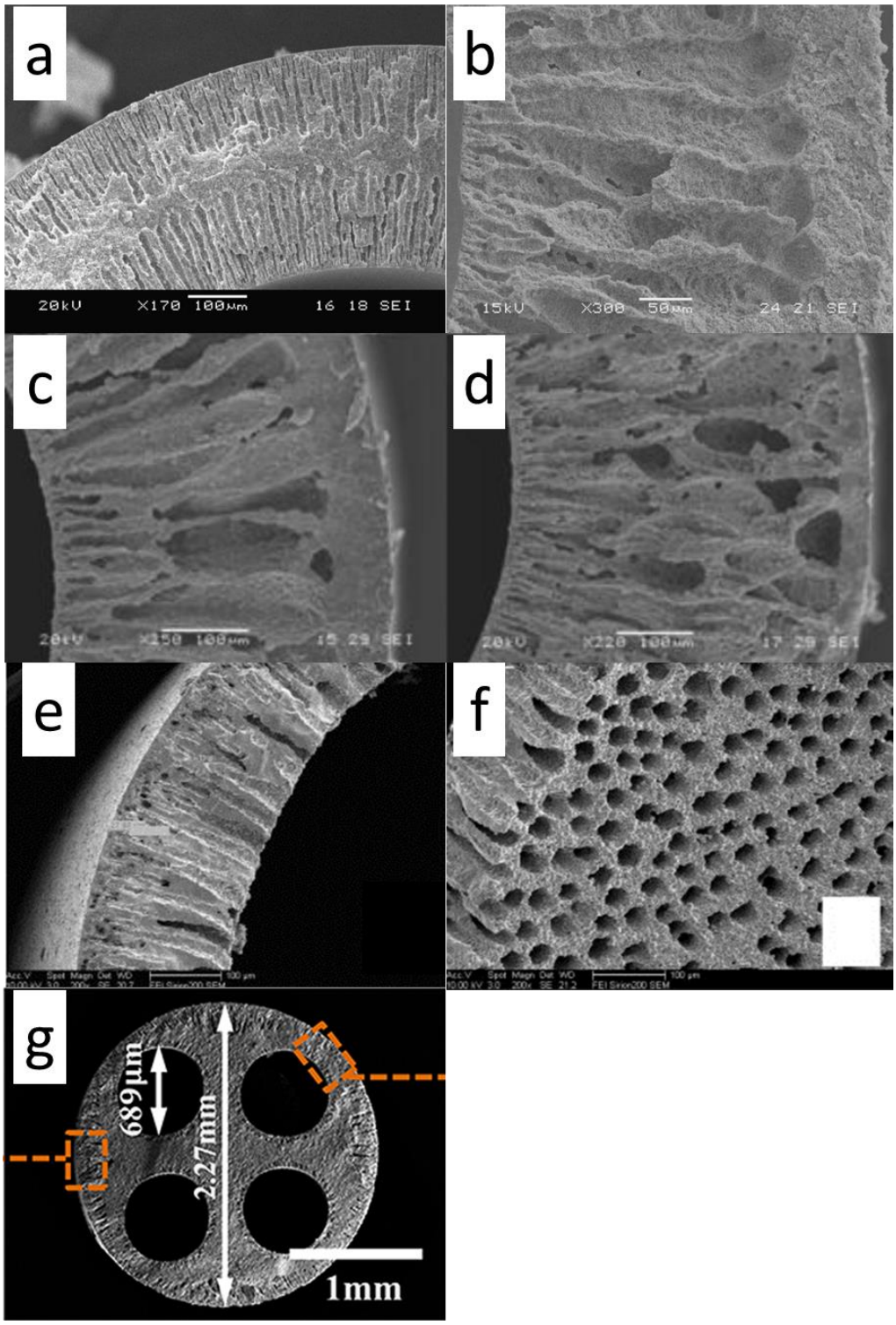

Figure 2-7. Finger-like pore structure in hollow fibres fabricated by using a) 0.17 ml s^{-1} internal water flow rate and 0 mm air gap,[161] b) 0.17 ml s^{-1} internal water flow rate and 150 mm air gap, c) 0.2 ml s^{-1} internal water flow rate and 70 mm air gap, d) 0.2 ml s^{-1} internal water flow rate and 130 mm air gap,[163] e) ultrathin hollow fibre with one group of microchannels,[169] f) open surface of ultrathin hollow fibre[169] and g) multichannel hollow fibre.[158] (Reprinted with permission from Elsevier)

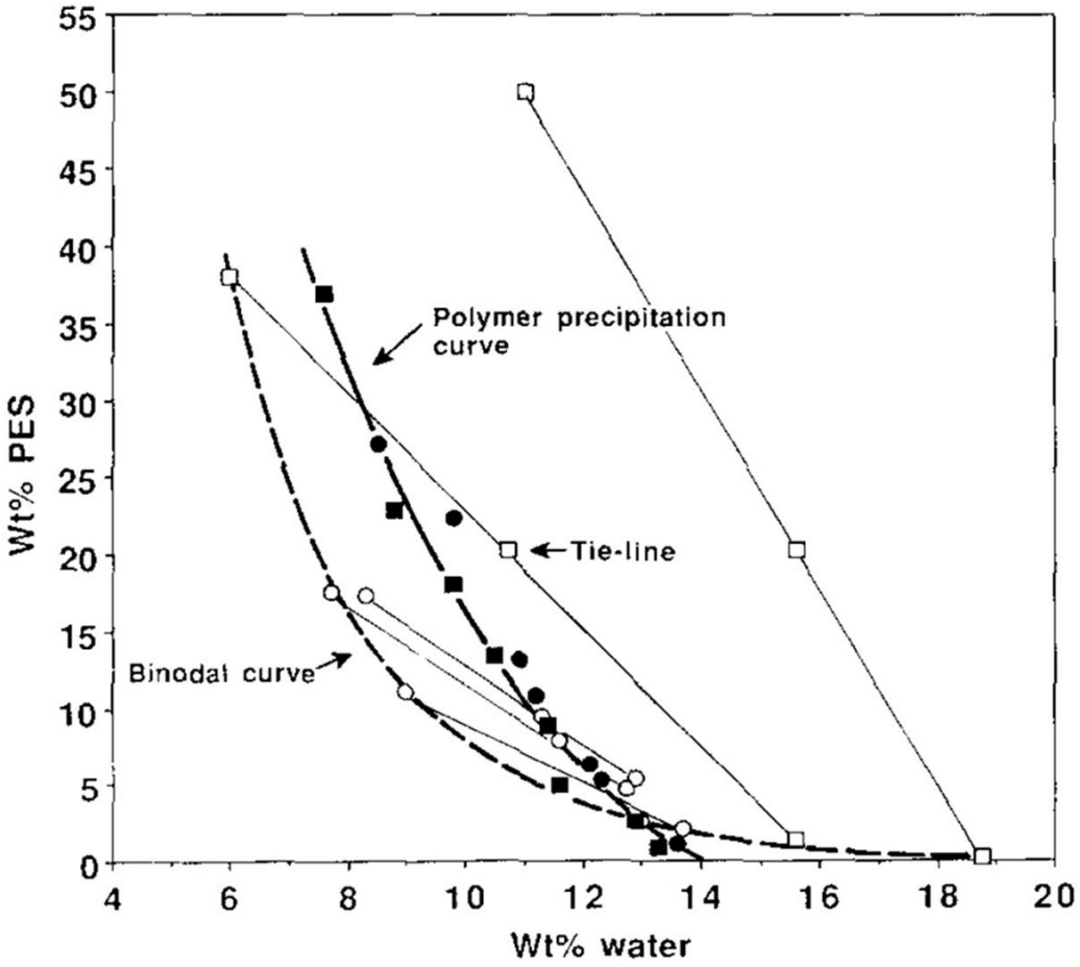

Figure 2-8. Polymer precipitation curve and binodal curve of PES/NMP/H_2O system at 25°C.[179]

Table 2-4. Miscibility parameters.[180]

	δ_d (mPa$^{0.5}$)	δ_p (mPa$^{0.5}$)	δ_h (mPa$^{0.5}$)	δ (mPa$^{0.5}$)
NMP	18.0	12.3	7.2	22.9
Water	15.5	16.0	42.3	47.8
Ethanol	15.8	8.8	19.4	26.5
Isopropanol	15.8	6.1	16.4	23.5
THF	16.8	5.7	8.0	19.4
DMF	17.4	13.7	11.3	24.8

Moreover, many researchers found that a high concentration of polymer solution could depress the formation of microchannels and the membrane tended to form sponge-like

pores.[181, 182] This was attributed to the increase of solution viscosity.[183] A similar approach to increase the solution viscosity is adding polymer, such as PVP with high molecular weight and polyethylene glycol (PEG).[184-186]

2.3.3.3 Modelling description of oxygen permeation in hollow fibre membranes

Li's group built a model based on the established mathematical description of conventional disk membrane. In this model, the oxygen permeation in hollow fibre membranes was expressed using differential equations.[147, 187, 188]

Equation 10 in this chapter can be written as:

$$\frac{1}{2\pi r}\frac{dN_{O_2}}{dl} = \frac{D_v}{2}\frac{dC_v}{dr} \qquad (38)$$

where N_{O_2} is the oxygen flux in hollow fibre membranes, r is the radius of the hollow fibre, l is the axial length scale of the hollow fibre.

Integrating the right side of equation 38 yields:

$$dN_{O_2} = \pi D_v \frac{\int_{C_v'}^{C_v''} dC_v}{\int_{R_{in}}^{R_o} \frac{dr}{r}} = \pi D_v \frac{C_v'' - C_v'}{ln\frac{R_o}{R_{in}}} dl \qquad (39)$$

where R_o and R_{in} are the outer and inner radius of the hollow fibre, respectively.

The oxygen surface reactions on hollow fibre surfaces would remain the same as reactions A and B in section 2.2.1. Therefore, the oxygen flux due to surface reaction can be expressed as:

$$dN_{O_2} = 2\pi R_o\left(k_f p_{O_2}'^{0.5} C_v' - k_r\right)dl \qquad (40)$$

and

$$dN_{O_2} = 2\pi R_{in}\left(k_r - k_f p_{O_2}''^{0.5} C_v''\right)dl \qquad (41)$$

Combining equations 38-41 yields:

$$dN_{O_2} = \frac{k_r(p'^{0.5}_{O_2} - p''^{0.5}_{O_2})}{\frac{p''^{0.5}_{O_2}}{2\pi R_O} + \frac{k_f \ln(\frac{R_O}{R_{in}}) p'^{0.5}_{O_2} p''^{0.5}_{O_2}}{\pi D_v} + \frac{p'^{0.5}_{O_2}}{2\pi R_{in}}} dl \quad (42)$$

Equation 42 is the global equation for oxygen permeation in hollow fibre membranes. At oxygen lean side, hollow fibre membrane can either use sweep gas or vacuum to maintain the oxygen potential difference. The hollow fibre geometry is also easy for vacuum operation. In vacuum operation, it was generally operated with vacuum on the inner side of the hollow fibre for easy operation. Since hollow fibre membranes have a certain length scale, the pressure in the inner side of a hollow fibre is not constant along the axial direction. The pressure profile should be mentioned for correct modelling. It can be described using the Hagen-Poiseuille equation:[139, 187]

$$\frac{dP_{O_2}}{dl} = -\frac{8\mu RT}{n\pi R_{in}^4 p''_{O_2}} N_{O_2} \quad (43)$$

where P_{O_2} is the applied vacuum level (absolute pressure), μ is viscosity of oxygen and n is the number of hollow fibres.

However, it is difficult to see the differences between oxygen permeation in hollow fibre membranes composed of microchannels and dense membranes in those models. The model cannot describe the oxygen permeation difference caused by microstructure difference of hollow fibre membranes. Compared with establishing model to analyse the oxygen permeation in hollow fibre membrane, an experimental analysis will be more convincing.

2.4 Novel membrane microstructure developed in this thesis

In summary, the supported and hollow fibre membranes were developed to improve oxygen flux. The major problems of the supported membranes are the complex fabrication process and the poor thermal compatibility between porous support and dense layer. These problems greatly limit the use of the supported membrane in practical applications. Hollow fibre membranes showed high oxygen flux due to the thin membrane walls. The oxygen transports in hollow fibre membranes with asymmetric pores consist of many steps and each step could introduce extra resistance for oxygen permeation. It can be expected that the resistance of oxygen permeation can be largely reduced if the skin layers of the hollow fibre membranes

are removed. In this thesis, a simple process, mesh-templated phase inversion process, has been developed to remove the membrane skin layer formed in phase inversion process. The formed membranes showed novel microchanneled microstructures and high oxygen fluxes that will be demonstrated in the following chapters.

2.5 References

1. A. Leo, S. Liu and J. C. D. d. Costa, *International Journal of Greenhouse Gas Control*, 2009, **3**, 357-367.
2. H. Stadler, F. Beggel, M. Habermehl, B. Persigehl, R. Kneer, M. Modigell and P. Jeschke, *International Journal of Greenhouse Gas Control*, 2011, **5**, 7-15.
3. C.-s. Chen, S.-j. Feng, S. Ran, D.-c. Zhu, W. Liu and H. J. M. Bouwmeester, *Angewandte Chemie International Edition*, 2003, **42**, 5196-5198.
4. S. S. Hashim, A. R. Mohamed and S. Bhatia, *Renewable and Sustainable Energy Reviews*, 2011, **15**, 1284-1293.
5. R. Agrawal, M. S.-K. Chen, A. R. Smith, R. M. Thorogood and T. J. Ward, Google Patents, 1997.
6. S. Smart, C. Lin, L. Ding, K. Thambimuthu and J. D. Da Costa, *Energy & Environmental Science*, 2010, **3**, 268-278.
7. U. Balachandran, J. Dusek, R. L. Mieville, R. Poeppel, M. Kleefisch, S. Pei, T. Kobylinski, C. Udovich and A. Bose, *Applied Catalysis A: General*, 1995, **133**, 19-29.
8. U. Balachandran, J. Dusek, P. Maiya, B. Ma, R. Mieville, M. Kleefisch and C. Udovich, *Catalysis Today*, 1997, **36**, 265-272.
9. L. Van Dijk and G. Roncken, *Water Science and Technology*, 1997, **35**, 35-41.
10. R. Thorogood, *Gas separation & purification*, 1991, **5**, 83-94.
11. T. E. Cormier, R. Agrawal, A. L. Prentice and D. W. Woodward, Google Patents, 1991.
12. B. Ha, U.S. Patent 5231837,, 1993.
13. J. Schlaechter, U.S. Patent 4534346 1985.

14. W. C. Kratz and S. Sircar, U.S. Patent 4477264, 1984.

15. H. Wang, L. Huang, B. A. Holmberg and Y. Yan, *Chemical Communications*, 2002, 1708-1709.

16. M. Arnold, T. M. Gesing, J. Martynczuk and A. Feldhoff, *Chemistry of Materials*, 2008, **20**, 5851-5858.

17. S. McIntosh, J. F. Vente, W. G. Haije, D. H. A. Blank and H. J. M. Bouwmeester, *Solid State Ionics*, 2006, **177**, 833-842.

18. B. J. Mitchell, R. C. Rogan, J. W. Richardson Jr, B. Ma and U. Balachandran, *Solid State Ionics*, 2002, **146**, 313-321.

19. H. Luo, K. Efimov, H. Jiang, A. Feldhoff, H. Wang and J. Caro, *Angewandte Chemie International Edition*, 2011, **50**, 759-763.

20. H. Wang, C. Tablet, A. Feldhoff and J. Caro, *Advanced Materials*, 2005, **17**, 1785-1788.

21. C. Wagner, *Progress in Solid State Chemistry*, 1975, **10, Part 1**, 3-16.

22. L. Heyne, in *Solid electrolytes*, Springer, 1977, pp. 169-221.

23. Y. S. Lin, W. Wang and J. Han, *AIChE journal*, 1994, **40**, 786-798.

24. S. J. Xu and W. J. Thomson, *Chemical Engineering Science*, 1999, **54**, 3839-3850.

25. A. A. Asadi, A. Behrouzifar, M. Iravaninia, T. Mohammadi and A. Pak, *Industrial & Engineering Chemistry Research*, 2012, **51**, 3069-3080.

26. A. Ghadimi, M. A. Alaee, A. Behrouzifar, A. A. Asadi and T. Mohammadi, *Desalination*, 2011, **270**, 64-75.

27. Z. Shao, G. Xiong, H. Dong, W. Yang and L. Lin, *Separation and Purification Technology*, 2001, **25**, 97-116.

28. J. Hong, P. Kirchen and A. F. Ghoniem, *Journal of Membrane Science*, 2012, **407–408**, 71-85.

29. A. M. Svensson, S. Sunde and K. Nis¸ancioĞlu, *Journal of The Electrochemical Society*, 1998, **145**, 1390-1400.

30. T. Ishigaki, S. Yamauchi, K. Kishio, J. Mizusaki and K. Fueki, *Journal of Solid State Chemistry*, 1988, **73**, 179-187.

31. S. Carter, A. Selcuk, R. J. Chater, J. Kajda, J. A. Kilner and B. C. H. Steele, *Solid State Ionics*, 1992, **53–56, Part 1**, 597-605.

32. T. Ishihara, J. A. Kilner, M. Honda, N. Sakai, H. Yokokawa and Y. Takita, *Solid State Ionics*, 1998, **113–115**, 593-600.

33. R. E. van Doorn, I. C. Fullarton, R. A. de Souza, J. A. Kilner, H. J. M. Bouwmeester and A. J. Burggraaf, *Solid State Ionics*, 1997, **96**, 1-7.

34. E. N. Armstrong, K. L. Duncan, D. J. Oh, J. F. Weaver and E. D. Wachsman, *Journal of The Electrochemical Society*, 2011, **158**, B492-B499.

35. E. N. Armstrong, K. L. Duncan and E. D. Wachsman, *Journal of The Electrochemical Society*, 2011, **158**, B283-B289.

36. C. C. Kan, H. H. Kan, F. M. Van Assche, E. N. Armstrong and E. D. Wachsman, *Journal of The Electrochemical Society*, 2008, **155**, B985-B993.

37. R. J. Chater, S. Carter, J. A. Kilner and B. C. H. Steele, *Solid State Ionics*, 1992, **53–56, Part 2**, 859-867.

38. R. A. De Souza and J. A. Kilner, *Solid State Ionics*, 1998, **106**, 175-187.

39. J. A. Kilner, R. A. De Souza and I. C. Fullarton, *Solid State Ionics*, 1996, **86–88, Part 2**, 703-709.

40. R. A. De Souza, *Physical Chemistry Chemical Physics*, 2006, **8**, 890-897.

41. F. Ciucci, *Solid State Ionics*, 2013, **239**, 28-40.

42. P. M. Geffroy, Y. Hu, A. Vivet, T. Chartier and G. Dezanneau, *Journal of The Electrochemical Society*, 2014, **161**, F153-F160.

43. P. Ried, P. Holtappels, A. Wichser, A. Ulrich and T. Graule, *Journal of The Electrochemical Society*, 2008, **155**, B1029-B1035.

44. P. F. Haworth, S. Smart, J. M. Serra and J. C. Diniz da Costa, *Physical Chemistry Chemical Physics*, 2012, **14**, 9104-9111.

45. J. E. ten Elshof, M. H. R. Lankhorst and H. J. M. Bouwmeester, *Journal of The Electrochemical Society*, 1997, **144**, 1060-1067.

46. S. Diethelm, A. Closset, K. Nisançioglu, J. Van herle, A. J. McEvoy and T. M. Gün, *Journal of The Electrochemical Society*, 1999, **146**, 2606-2612.

47. M. Schroeder, *Physical Chemistry Chemical Physics*, 2005, **7**, 166-172.

48. K. Huang and J. B. Goodenough, *Journal of The Electrochemical Society*, 2001, **148**, E203-E214.

49. J. Maier, *Solid State Ionics*, 1998, **112**, 197-228.

50. H. J. M. Bouwmeester, H. Kruidhof and A. J. Burggraaf, *Solid State Ionics*, 1994, **72, Part 2**, 185-194.

51. C. H. Chen, H. J. M. Bouwmeester, R. H. E. van Doorn, H. Kruidhof and A. J. Burggraaf, *Solid State Ionics*, 1997, **98**, 7-13.

52. C.-s. Chen, Z.-p. Zhang, G.-s. Jiang, C.-g. Fan, W. Liu and H. J. M. Bouwmeester, *Chemistry of Materials*, 2001, **13**, 2797-2800.

53. P. M. Geffroy, J. M. Bassat, A. Vivet, S. Fourcade, T. Chartier, P. Del Gallo and N. Richet, *Journal of Membrane Science*, 2010, **354**, 6-13.

54. A. J. Samson, M. Søgaard and P. Vang Hendriksen, *Journal of Membrane Science*, 2014, **470**, 178-188.

55. X. Zhu, Y. Cong and W. Yang, *Journal of Membrane Science*, 2006, **283**, 38-44.

56. E. Capoen, G. Nowogrocki, R. J. Chater, S. J. Skinner, J. A. Kilner, M. Malys, J. C. Boivin, G. Mairesse and R. N. Vannier, *Solid State Ionics*, 2006, **177**, 489-492.

57. H. Arashi and H. Naito, *Solid State Ionics*, 1992, **53–56, Part 1**, 431-435.

58. P. Zeng, Z. Chen, W. Zhou, H. Gu, Z. Shao and S. Liu, *Journal of Membrane Science*, 2007, **291**, 148-156.

59. F. T. Akin, Y. S. Lin and Y. Zeng, *Industrial & Engineering Chemistry Research*, 2001, **40**, 5908-5916.

60. T. H. Lee, Y. L. Yang, A. J. Jacobson, B. Abeles and M. Zhou, *Solid State Ionics*, 1997, **100**, 77-85.

61. Z. Zhang, Y. Chen, M. O. Tade, Y. Hao, S. Liu and Z. Shao, *Journal of Materials Chemistry A*, 2014, **2**, 9666-9674.

62. H. Bouwmeester, H. Kruidhof, A. Burggraaf and P. Gellings, *Solid State Ionics*, 1992, **53**, 460-468.

63. B. A. Boukamp, I. C. Vinke, K. J. De Vries and A. J. Burggraaf, *Solid State Ionics*, 1989, **32–33, Part 2**, 918-923.

64. S. Dou, C. Masson and P. Pacey, *Journal of the Electrochemical Society*, 1985, **132**, 1843-1849.

65. S. Li, W. Jin, N. Xu and J. Shi, *Solid State Ionics*, 1999, **124**, 161-170.

66. H. J. Bouwmeester and A. J. Burggraaf, *Membrane Science and Technology*, 1996, **4**, 435-528.

67. F. Iguchi, N. Sata, H. Yugami and H. Takamura, *Solid State Ionics*, 2006, **177**, 2281-2284.

68. S. Aasland, I. L. Tangen, K. Wiik and R. Ødegård, *Solid State Ionics*, 2000, **135**, 713-717.

69. W. K. Hong and G. M. Choi, *Journal of Membrane Science*, 2010, **346**, 353-360.

70. B. He, K. Zhang, Y. Ling, J. Xu and L. Zhao, *Journal of Membrane Science*, 2014, **464**, 55-60.

71. T. Kida, S. Ninomiya, K. Watanabe, N. Yamazoe and K. Shimanoe, *ACS Applied Materials & Interfaces*, 2010, **2**, 2849-2853.

72. X. Tan, Z. Wang, H. Liu and S. Liu, *Journal of Membrane Science*, 2008, **324**, 128-135.

73. C. Yacou, J. Sunarso, C. X. C. Lin, S. Smart, S. Liu and J. C. Diniz da Costa, *Journal of Membrane Science*, 2011, **380**, 223-231.

74. Y. Wang, H. Hao, J. Jia, D. Yang and X. Hu, *Journal of the European Ceramic Society*, 2008, **28**, 3125-3130.

75. X. Chang, C. Zhang, Z. Wu, W. Jin and N. Xu, *Industrial & engineering chemistry research*, 2006, **45**, 2824-2829.

76. D. Han, J. Sunarso, X. Tan, Z. Yan, L. Liu and S. Liu, *Energy & fuels*, 2012, **26**, 4728-4734.

77. L. Qiu, T. H. Lee, L. M. Liu, Y. L. Yang and A. J. Jacobson, *Solid State Ionics*, 1995, **76**, 321-329.

78. J. Martynczuk, M. Arnold and A. Feldhoff, *Journal of Membrane Science*, 2008, **322**, 375-382.

79. Z. Shao, W. Yang, Y. Cong, H. Dong, J. Tong and G. Xiong, *Journal of Membrane Science*, 2000, **172**, 177-188.

80. X. Zhu, H. Wang and W. Yang, *Chemical communications*, 2004, 1130-1131.

81. S. Kim, Y. L. Yang, R. Christoffersen and A. J. Jacobson, *Solid State Ionics*, 1997, **104**, 57-65.

82. J. Han, Y. Zeng and Y. S. Lin, *Journal of Membrane Science*, 1997, **132**, 235-243.

83. J. Tong, W. Yang, R. Cai, B. Zhu, G. Xiong and L. Lin, *Separation and Purification Technology*, 2003, **32**, 289-299.

84. F. Liang, H. Jiang, H. Luo, J. Caro and A. Feldhoff, *Chemistry of Materials*, 2011, **23**, 4765-4772.

85. S. Li, H. Qi, N. Xu and J. Shi, *Industrial & Engineering Chemistry Research*, 1999, **38**, 5028-5033.

86. K. Zhang, L. Ge, R. Ran, Z. Shao and S. Liu, *Acta Materialia*, 2008, **56**, 4876-4889.

87. H. Kusaba, Y. Shibata, K. Sasaki and Y. Teraoka, *Solid State Ionics*, 2006, **177**, 2249-2253.

88. Z. Shao, H. Dong, G. Xiong, Y. Cong and W. Yang, *Journal of Membrane Science*, 2001, **183**, 181-192.

89. A. C. van Veen, M. Rebeilleau, D. Farrusseng and C. Mirodatos, *Chemical Communications*, 2003, 32-33.

90. L. Yang, L. Tan, X. Gu, W. Jin, L. Zhang and N. Xu, *Industrial & Engineering Chemistry Research*, 2003, **42**, 2299-2305.

91. Z. Geng, W. Ding, H. Wang, C. Wu, P. Shen, X. Meng, Y. Gai and F. Ji, *Journal of Membrane Science*, 2012, **403–404**, 140-145.

92. B. Jiang, H. Cheng, L. Luo, X. Lu and Z. Zhou, *Journal of Materials Science & Technology*, 2014, **30**, 1174-1180.

93. Y. Zou, W. Zhou, S. Liu and Z. Shao, *Journal of the European Ceramic Society*, 2011, **31**, 2931-2938.

94. J. H. Park, K. Y. Kim and S. D. Park, *Desalination*, 2009, **245**, 559-569.

95. Z. Shao, G. Xiong, Y. Cong and W. Yang, *Journal of Membrane Science*, 2000, **164**, 167-176.

96. O. A. Savinskaya and A. P. Nemudry, *Journal of Membrane Science*, 2014, **459**, 45-51.

97. V. Kharton, F. Figueiredo, L. Navarro, E. Naumovich, A. Kovalevsky, A. Yaremchenko, A. P. Viskup, A. Carneiro, F. Marques and J. Frade, *Journal of Materials Science*, 2001, **36**, 1105-1117.

98. V. V. Kharton, A. V. Kovalevsky, A. P. Viskup, A. L. Shaula, F. M. Figueiredo, E. N. Naumovich and F. M. B. Marques, *Solid State Ionics*, 2003, **160**, 247-258.

99. H. L. Tuller, *Solid State Ionics*, 1997, **94**, 63-74.

100. V. V. Kharton, E. N. Naumovich and A. A. Vecher, *J Solid State Electrochem*, 1999, **3**, 61-81.

101. G. Etchegoyen, T. Chartier and P. Del-Gallo, *Journal of the European Ceramic Society*, 2006, **26**, 2807-2815.

102. M. Ikeguchi, K. Ishii, Y. Sekine, E. Kikuchi and M. Matsukata, *Materials Letters*, 2005, **59**, 1356-1360.

103. J. M. Serra, J. Garcia-Fayos, S. Baumann, F. Schulze-Küppers and W. A. Meulenberg, *Journal of Membrane Science*, 2013, **447**, 297-305.

104. S. Baumann, J. M. Serra, M. P. Lobera, S. Escolástico, F. Schulze-Küppers and W. A. Meulenberg, *Journal of Membrane Science*, 2011, **377**, 198-205.

105. M. Boaro, J. M. Vohs and R. J. Gorte, *Journal of the American Ceramic Society*, 2003, **86**, 395-400.

106. W. Jin, S. Li, P. Huang, N. Xu and J. Shi, *Journal of Membrane Science*, 2001, **185**, 237-243.

107. K. Watanabe, M. Yuasa, T. Kida, K. Shimanoe, Y. Teraoka and N. Yamazoe, *Solid State Ionics*, 2008, **179**, 1377-1381.

108. O. Büchler, J. M. Serra, W. A. Meulenberg, D. Sebold and H. P. Buchkremer, *Solid State Ionics*, 2007, **178**, 91-99.

109. F. Schulze-Küppers, S. Baumann, W. A. Meulenberg, D. Stöver and H. P. Buchkremer, *Journal of Membrane Science*, 2013, **433**, 121-125.

110. X. Chang, C. Zhang, X. Dong, C. Yang, W. Jin and N. Xu, *Journal of Membrane Science*, 2008, **322**, 429-435.

111. B. A. van Hassel, *Solid State Ionics*, 2004, **174**, 253-260.

112. Y. Vural, L. Ma, D. B. Ingham and M. Pourkashanian, *Journal of Power Sources*, 2010, **195**, 4893-4904.

113. S. B. Adler, J. A. Lane and B. C. H. Steele, *Journal of The Electrochemical Society*, 1996, **143**, 3554-3564.

114. H. Deng, M. Zhou and B. Abeles, *Solid State Ionics*, 1994, **74**, 75-84.

115. T. H. Lee, Y. L. Yang, A. J. Jacobson, B. Abeles and S. Milner, *Solid State Ionics*, 1997, **100**, 87-94.

116. K. Zhang, J. Sunarso, Z. Shao, W. Zhou, C. Sun, S. Wang and S. Liu, *RSC Advances*, 2011, **1**, 1661-1676.

117. P. L. Rachadel, J. Motuzas, G. Ji, D. Hotza and J. C. Diniz da Costa, *Journal of Membrane Science*, 2014, **454**, 382-389.

118. S. Beaudet Savignat, M. Chiron and C. Barthet, *Journal of the European Ceramic Society*, 2007, **27**, 673-678.

119. P. Niehoff, S. Baumann, F. Schulze-Küppers, R. S. Bradley, I. Shapiro, W. A. Meulenberg, P. J. Withers and R. Vaßen, *Separation and Purification Technology*, 2014, **121**, 60-67.

120. R. Ghosh, *Journal of Chromatography A*, 2002, **952**, 13-27.

121. S. Nakatsuka, I. Nakate and T. Miyano, *Desalination*, 1996, **106**, 55-61.

122. M. Inoue and K. Kawashima, Google Patents, 1987.

123. T. Melin, B. Jefferson, D. Bixio, C. Thoeye, W. De Wilde, J. De Koning, J. van der Graaf and T. Wintgens, *Desalination*, 2006, **187**, 271-282.

124. K. Kitazato, Y. Sunaoka and S. Tsuda, Google Patents, 1992.

125. W. J. Koros and G. K. Fleming, *Journal of Membrane Science*, 1993, **83**, 1-80.

126. J. M. S. Henis and M. K. Tripodi, *Separation Science and Technology*, 1980, **15**, 1059-1068.

127. D. Wang, W. K. Teo and K. Li, *Separation and Purification Technology*, 2002, **27**, 33-40.

128. D. Wang, W. K. Teo and K. Li, *Journal of Applied Polymer Science*, 2002, **86**, 698-702.

129. M. A. Rahman, F. R. García-García, M. D. I. Hatim, B. F. K. Kingsbury and K. Li, *Journal of Membrane Science*, 2011, **368**, 116-123.

130. M. D. Irfan Hatim, X. Tan, Z. Wu and K. Li, *Chemical Engineering Science*, 2011, **66**, 1150-1158.

131. X. Tan, S. Liu and K. Li, *Journal of Membrane Science*, 2001, **188**, 87-95.

132. S. Liu, X. Tan, K. Li and R. Hughes, *Catalysis Reviews*, 2001, **43**, 147-198.

133. S. Liu, X. Tan, K. Li and R. Hughes, *Journal of Membrane Science*, 2001, **193**, 249-260.

134. X. Tan and K. Li, *Industrial & Engineering Chemistry Research*, 2005, **45**, 142-149.

135. M. H. D. Othman, N. Droushiotis, Z. Wu, K. Kanawka, G. Kelsall and K. Li, *Journal of Membrane Science*, 2010, **365**, 382-388.

136. N. Droushiotis, U. Doraswami, D. Ivey, M. H. D. Othman, K. Li and G. Kelsall, *Electrochemistry Communications*, 2010, **12**, 792-795.

137. M. H. D. Othman, N. Droushiotis, Z. Wu, G. Kelsall and K. Li, *Advanced Materials*, 2011, **23**, 2480-2483.

138. X. Tan, Z. Pang and K. Li, *Journal of Membrane Science*, 2008, **310**, 550-556.

139. X. Tan, Y. Liu and K. Li, *AIChE Journal*, 2005, **51**, 1991-2000.

140. Y. Wei, H. Liu, J. Xue, Z. Li and H. Wang, *AIChE Journal*, 2011, **57**, 975-984.

141. Y. Wei, J. Tang, L. Zhou, J. Xue, Z. Li and H. Wang, *AIChE Journal*, 2012, **58**, 2856-2864.

142. D. Han, X. Tan, Z. Yan, Q. Li and S. Liu, *Ceramics International*, 2013, **39**, 431-437.

143. T. Schiestel, M. Kilgus, S. Peter, K. J. Caspary, H. Wang and J. Caro, *Journal of Membrane Science*, 2005, **258**, 1-4.

144. K. Li, X. Tan and Y. Liu, *Journal of Membrane Science*, 2006, **272**, 1-5.

145. S. Liu and G. R. Gavalas, *Journal of Membrane Science*, 2005, **246**, 103-108.

146. B. Zydorczak, Z. Wu and K. Li, *Chemical Engineering Science*, 2009, **64**, 4383-4388.

147. Z. Wang, N. Yang, B. Meng, X. Tan and K. Li, *Industrial & Engineering Chemistry Research*, 2008, **48**, 510-516.

148. B. Meng, Z. Wang, Y. Liu, X. Tan, J. C. D. da Costa and S. Liu, *Separation and Purification Technology*, 2011, **78**, 175-180.

149. X. Tan, L. Shi, G. Hao, B. Meng and S. Liu, *Separation and Purification Technology*, 2012, **96**, 89-97.

150. F. Liang, H. Jiang, T. Schiestel and J. r. Caro, *Industrial & Engineering Chemistry Research*, 2010, **49**, 9377-9384.

151. X. Tan, Z. Wang and K. Li, *Industrial & Engineering Chemistry Research*, 2010, **49**, 2895-2901.

152. J. Sunarso, S. Liu, Y. S. Lin and J. C. Diniz da Costa, *Energy & Environmental Science*, 2011, **4**, 2516-2519.

153. C. Buysse, A. Kovalevsky, F. Snijkers, A. Buekenhoudt, S. Mullens, J. Luyten, J. Kretzschmar and S. Lenaerts, *Journal of Membrane Science*, 2011, **372**, 239-248.

154. P. Haworth, S. Smart, J. Glasscock and J. C. Diniz da Costa, *Separation and Purification Technology*, 2012, **94**, 16-22.

155. N. Droushiotis, M. H. D. Othman, U. Doraswami, Z. Wu, G. Kelsall and K. Li, *Electrochemistry Communications*, 2009, **11**, 1799-1802.

156. M. H. D. Othman, Z. Wu, N. Droushiotis, U. Doraswami, G. Kelsall and K. Li, *Journal of Membrane Science*, 2010, **351**, 196-204.

157. T. Li, Z. Wu and K. Li, *Journal of Membrane Science*, 2014, **449**, 1-8.

158. J. Zhu, Z. Liu, S. Guo and W. Jin, *Chemical Engineering Science*, 2015, **122**, 614-621.

159. Z. Wu, B. Wang and K. Li, *Journal of Membrane Science*, 2010, **352**, 63-70.

160. D. Wang, W. Teo and K. Li, *Journal of membrane science*, 2002, **204**, 247-256.

161. B. F. K. Kingsbury and K. Li, *Journal of Membrane Science*, 2009, **328**, 134-140.

162. X. Tan, Y. Liu and K. Li, *Industrial & Engineering Chemistry Research*, 2004, **44**, 61-66.

163. B. F. K. Kingsbury, Z. Wu and K. Li, *Catalysis Today*, 2010, **156**, 306-315.

164. F. R. García-García and K. Li, *Applied Catalysis A: General*, 2013, **456**, 1-10.

165. F. R. García-García, M. A. Rahman, B. F. K. Kingsbury and K. Li, *Applied Catalysis A: General*, 2011, **393**, 71-77.

166. X. Zhang, B. Lin, Y. Ling, Y. Dong, D. Fang, G. Meng and X. Liu, *Journal of Alloys and Compounds*, 2010, **494**, 366-371.

167. X. Tan, N. Liu, B. Meng and S. Liu, *Journal of Membrane Science*, 2011, **378**, 308-318.

168. N. H. Othman, Z. Wu and K. Li, *Journal of Membrane Science*, 2014, **468**, 31-41.

169. N. Liu, X. Tan, B. Meng and S. Liu, *Separation and Purification Technology*, 2011, **80**, 396-401.

170. Z. Wang, H. Liu, X. Tan, Y. Jin and S. Liu, *Journal of Membrane Science*, 2009, **345**, 65-73.

171. H. Strathmann, K. Kock, P. Amar and R. W. Baker, *Desalination*, 1975, **16**, 179-203.

172. A. Goete, Google Patents, 1960.

173. R. Kesting, *Journal of Applied Polymer Science*, 1973, **17**, 1771-1785.

174. T.-H. Young and L.-W. Chen, *Journal of Membrane Science*, 1991, **57**, 69-81.

175. T.-H. Young and L.-W. Chen, *Desalination*, 1995, **103**, 233-247.

176. C. A. Smolders, A. J. Reuvers, R. M. Boom and I. M. Wienk, *Journal of Membrane Science*, 1992, **73**, 259-275.

177. C. Stropnik, L. Germič and B. Žerjal, *Journal of Applied Polymer Science*, 1996, **61**, 1821-1830.

178. G. R. Guillen, G. Z. Ramon, H. P. Kavehpour, R. B. Kaner and E. M. V. Hoek, *Journal of Membrane Science*, 2013, **431**, 212-220.

179. W. W. Y. Lau, M. D. Guiver and T. Matsuura, *Journal of Membrane Science*, 1991, **59**, 219-227.

180. B. Sellergren and K. J. Shea, *Journal of Chromatography A*, 1993, **635**, 31-49.

181. Z. Zhang, Q. An, Y. Ji, J. Qian and C. Gao, *Desalination*, 2010, **260**, 43-50.

182. Z. Li and C. Jiang, *Journal of Polymer Science Part B: Polymer Physics*, 2005, **43**, 498-510.

183. I. Cabasso, E. Klein and J. K. Smith, *Journal of Applied Polymer Science*, 1977, **21**, 165-180.

184. J. Barzin, S. S. Madaeni, H. Mirzadeh and M. Mehrabzadeh, *Journal of Applied Polymer Science*, 2004, **92**, 3804-3813.

185. M. M. Dal-Cin, C. M. Tam, M. D. Guiver and T. A. Tweddle, *Journal of Applied Polymer Science*, 1994, **54**, 783-792.

186. Q.-Z. Zheng, P. Wang, Y.-N. Yang and D.-J. Cui, *Journal of Membrane Science*, 2006, **286**, 7-11.

187. X. Tan and K. Li, *AIChE Journal*, 2002, **48**, 1469-1477.

188. X. Tan and K. Li, *AIChE Journal*, 2007, **53**, 838-845.

Chapter 3. A microchanneled ceramic membrane for highly-efficient oxygen separation

3.1 Introduction

Ion transport membranes (ITMs) for the separation of oxygen from air have attracted considerable research interest because they can produce oxygen at lower costs than those incurred during the conventional cryogenic distillation process. More economic and environmental benefits can be derived when the oxygen separation is integrated with high temperature processes such as natural gas conversion and hydrogen/synthesis gas production from fossil fuels and renewable energy.[1-5] Low or zero emission from power plants can be realized when employing ceramic membranes to supply oxygen for oxyfuel combustion, because CO_2 can then be effectively captured after steam condensation.[6] However, slow oxygen permeation through conventional ITMs limits the overall process rate, and consequently there is currently intensive research into the oxygen permeation process. Oxygen exchange on the membrane surface and bulk diffusion within the dense membrane are considered to be two rate limiting steps of oxygen permeation within different operating temperature ranges.[7, 8] Some researchers concentrated on modifying membrane surfaces in order to improve the oxygen surface exchange by applying catalysts.[9, 10] Because of the strong temperature dependence of oxygen transport through ion conducting ceramics, oxygen permeation is generally realised at high temperatures (e.g. 900-1000 °C) in order to achieve high permeation rates, which are ultimately limited by the bulk diffusion resistance.[11] During the bulk diffusion process, the oxygen permeation flux (OPF, J_{O_2}) is inversely proportional to the membrane thickness (L) according to Wagner's equation:

$$J_{O_2} = \frac{\delta_e \delta_i}{16F^2 L(\delta_e+\delta_i)} \ln\left(\frac{P'_{O_2,feed}}{P''_{O_2,sweep}}\right) \qquad (3\text{-}1)$$

where F is Faraday constant, δ_e and δ_i are electronic and ionic conductivities, respectively, $P'_{O_2,feed}$ and $P''_{O_2,sweep}$ are oxygen partial pressures at oxygen feed side and sweep gas side, respectively. Therefore, reducing the membrane thickness is an effective way to achieve high OPFs.

There are two main types of ceramic membrane configurations: plate and tube. Plate membranes, such as disc membranes used in laboratory experiments, typically have a thickness of about 1 mm in order to ensure they have adequate mechanical strength, with the consequence that there is a long oxygen bulk diffusion distance. Ceramic membranes with thin dense layers (less than 100 μm) supported on porous substrates were developed to increase high OPFs via reducing oxygen ion diffusion distances.[12] In the design of supported membranes, the match of thermal expansion and chemical compatibility between the dense layer and the porous support needs to be carefully considered because of the high sintering and operating temperatures used (up to 1250 °C).[13] Furthermore, the asymmetric membranes need to be sintered at high temperatures to obtain the dense layers, leading to a porous support with low porosity and isolated pores causing gas diffusion resistance in the supports.[14] In addition, the low porosity of such supports makes it difficult to deposit catalysts for oxygen surface exchange at the interface between the porous support and the dense layer.

Tubular membranes prepared by paste extrusion also suffer from the thick dense layer similar to that in plate membranes, and therefore hollow fibre membranes with outer diameters of less than 3 mm are attractive because it is then possible to achieve a membrane thickness of less than 500 μm. A phase inversion process is employed to form the hollow fibre membranes by spinning a ceramic slurry into coagulants, and the hollow fibre membrane wall has a complicated microstructure. Phase inversion starts from both sides of the membrane wall, caused by the internal and external coagulants, leading to the complicated structure: skin layers on two sides and a central layer sandwiched by two groups of finger-like pores (Figure 3-1a).[15] After sintering, the central layer as well as the two skin layers turn into dense layers that perform oxygen separation via ion transport. However, the two groups of pores partly interrupt the oxygen ion transport, and tripled surface exchange processes are required to complete the oxygen permeation. Two methods have been proposed to tackle the problem: Wang et al. used acids to erode the skin layers and open the finger-like pores; [16] alternatively a certain amount of solvent was added to the internal coagulant to prevent the formation of an inner skin layer or to dissolve any newly-formed skin layer.[15] Nevertheless, the methods suffer from complicated processes and/or low mechanical strength due to ultra-thin fibre walls (about 100 μm) and high porosities (up to 46.9%).[4, 16, 17]

Herein, we report plate membranes with a novel microstructure prepared by a mesh-assisted phase inversion process. Ceramic slurry containing dissolved polymer was cast into a mould for the formation of plate membranes, and a coagulant was applied on top of the cast slurry. Consequently, the phase inversion only started from the top of the slurry, resulting in one group of pore channels sandwiched by a skin layer and a bottom layer (Figure 3-1). The resulting membrane showed a simpler microstructure compared with hollow fibre membranes. Furthermore, we removed the skin layer to open the pore channels. Accordingly, the membrane structure was substantially simplified, and the novel microstructure of these membrane results in high OPFs because of the substantially shortened oxygen permeation distance and the enlarged membrane surface area located within pore channels.

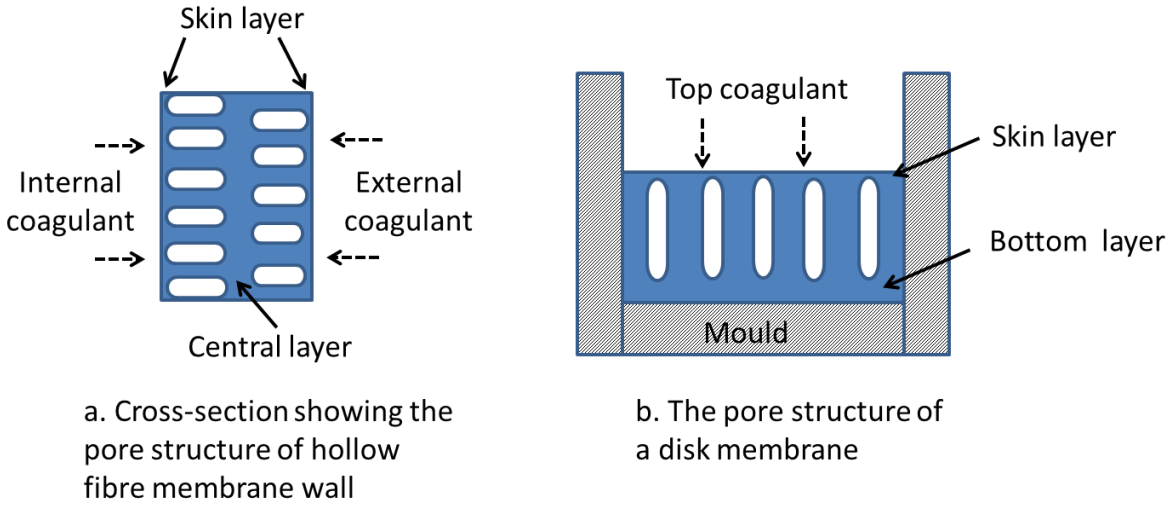

Figure. 3-1. Structural comparison of hollow fibre membranes and plate membranes prepared by phase inversion processes.

3.2 Experimental

3.2.1 Membrane preparation and characterization

The ceramic membranes were prepared by a modified phase inversion process with subsequent sintering. Typically, 4.3 g of Polyethersulfone (PESF) and 0.7 g of Polyvinylpyrrolidone (PVP, MW=40000) were dissolved in 30 g of 1-Methyl-2-pyrrolidinone (NMP, 99%) in a beaker by magnetic stirring (chemicals were purchased from Sigma-Aldrich Australia). Then, 65 g of $La_{0.6}Sr_{0.4}Co_{0.2}Fe_{0.8}O_{3-\delta}$ (LSCF-6428, Fuel Cell

Materials, USA) powder with a BET surface area of 5.5 cm^2/g was mixed with the above solution in a Teflon jar. The mixture was ball milled for 48 hours by a planetry ball-miller (MTI Corporation, USA) at a speed of 300 RPM to form a homogeneous slurry. Next, 0.4 ml of the prepared slurry was transfered into an aluminium mould by a syringe. After degassing, a stainless steel mesh was immersed just below the slurry surface. 5 ml of tap water was poured on top of the slurry to induce phase inversion for 20 min. Finally, the stainless steel mesh was gently lifted off from the solidified slurry, thereby removing the skin layer. After drying at 80 °C for 60 min, the membrane was heated in a box furnace (ModuTemp Pty. Ltd., Australia) at 600 °C for 1 h to remove organic components and then sintered in air at 1350 °C for 5 h. The microstructure of the prepared membranes was observed by SEMs (Zeiss Neon 40EsB FIBSEM and Zeiss Evo 40XVP), and the mesh images were observed by a optical microscopy (Nikon Eclipss, ME600). Porosity was tested by using Archimedes‘ method.

3.2.2 Oxygen permeation test

To test oxygen permeation, the disc membrane was seated on a quartz tube by using ceramic adhesive (552-VFG, Aremco Products Inc., USA) as a sealant. The test was performed in a tubular furnace. Argon was used as a sweep gas, and air was used as a feed gas on the other side of the membrane with a constant flow rate of 270 ml min^{-1} in this experiment. The oxygen concentration in the sweep gas was measured by online gas chromatography (GC, GC-2014, Shimazu) with a packed column of molecular sieve 5Å, and the oxygen permeation flux was calculated using the following equation.

$$J_{O_2} = \frac{\mathrm{J}_{Sweep}(C_{O_2} - C_{N_2} * \frac{21}{79})}{\mathrm{A}} \qquad (3\text{-}2)$$

where J_{O_2} is oxygen permeation flux, J_{Sweep} is the flow rate of sweep gas, C_{O_2} is the concentration of permeated oxygen in sweep gas, C_{N_2} is the concentration of leaking nitrogen in sweep gas and A is the effective permeation area of the membrane. The thicknesses of all membranes were in the range of 0.80-0.85 mm. Oxygen leakage from the test system was below 1%, which was measured by the detected nitrogen levels.

3.3 Results and discussion

The preparation process of microstructured $La_{0.6}Sr_{0.4}Co_{0.2}Fe_{0.8}O_{3-\delta}$ (LSCF) membranes is schematically represented in Figure 3-2. Stainless steel mesh was immersed under the slurry surface after casting the slurry into a mould, and then tap water was poured on top of the slurry as a coagulant. After phase inversion, the thin skin layer above the mesh can be successfully removed by simply lifting off the mesh from the solidified slurry, leaving the opened pore channels terminating with a thin layer. After sintering, the thin layer became a dense layer, and the opened pore channels were retained in the membranes with some shrinkage due to sintering.

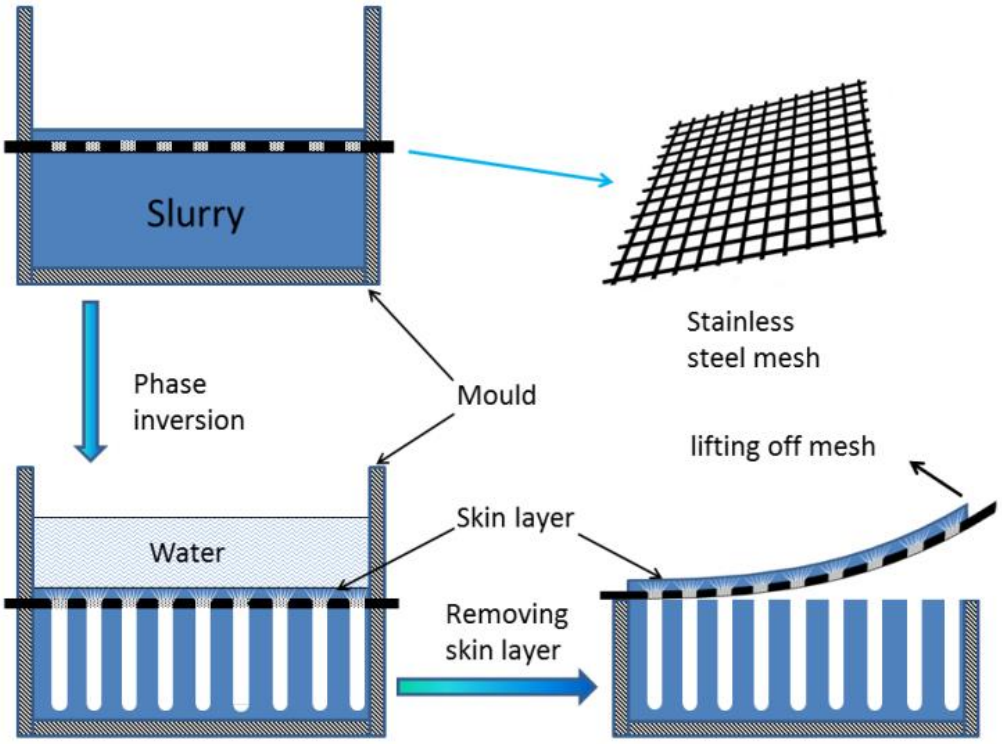

Figure 3-2. Schematic representation of the preparation of new membranes by a templating phase-inversion process.

For comparison, a membrane with a skin layer was prepared by the same process without applying the mesh. Figure 3-3 shows the surfaces and cross sections of the membranes with and without a skin layer. As shown in Figure 3-3a and 3-3b, the skin layer on the top of membrane as well as the bottom layer was densified after sintering at 1350 °C to form dense layers for oxygen separation. In Figure 3-3c and 3-3d, the skin layer was completely removed

by the mesh, and all pore channels were opened. In addition, these pore channels have uniform sizes of about 30 μm in diameter, and are referred to as microchannels. Interestingly, the microchannels were templated by the mesh because one mesh aperture produces one microchannel, corresponding to the wire mesh trace on the membrane surface, indicating the possibility of controlling the pore size *via* mesh aperture size. Significantly, microchannels traverse the membrane ending with a thin dense layer (about 100 μm) on the other side of the membrane, retaining an approximately uniform diameter throughout their length (Figure 3-3d). In contrast, for the membrane with a skin layer (Figure 3-3b), the pore channels are irregular. Numerous small pores start growing after the skin layer, and only some pores approach the bottom layer with greatly-increased pore sizes. This irregular structure occurs because these small pores compete in extracting 1-Methyl-2-pyrrolidone (NMP) solvent from the slurry into pores to develop themselves. Some pores stop growing when they fail in the competition, and some pores continue growing and become bigger by subsuming other pores. In this study, the stainless steel mesh has a significant role of combining small pores into large pores or templating microchannels when small pores pass through the mesh apertures during the phase inversion (Figure 3-4). The skin layer removed by lifting off the mesh, below a dense layer of about 15 μm in thickness, there are many small pore channels before the mesh wire trace. They start combining or disappearing when they approach the mesh, and finally are forced into large pores channel by the mesh, templating microchannels. The uniform mesh apertures template uniform microchannels. The uniform microchannels have a unified and balanced ability to extract NMP from the slurry, which promotes the formation of uniform and long channels. Therefore, the stainless steel mesh is used not only to remove the skin layer, but also to regulate/template the microchannel development.

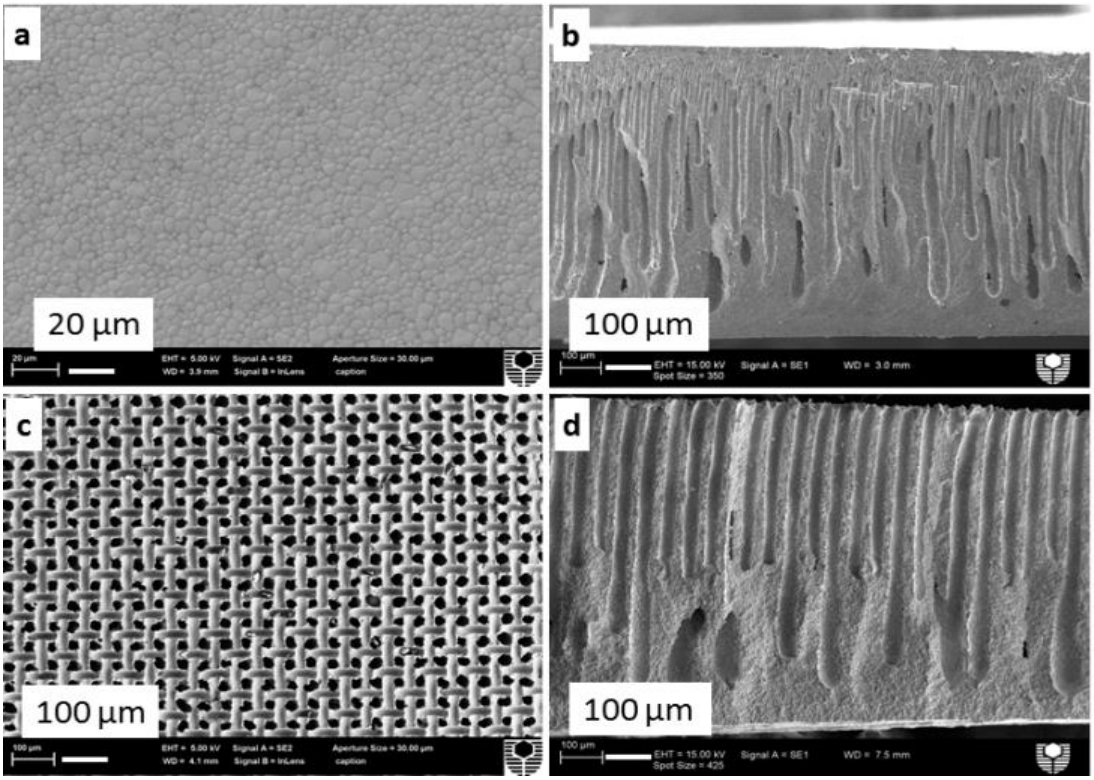

Figure 3-3. Scanning Electron Microscopy (SEM) images of the surface (a and c) and cross section (b and d) of membranes with (a and b) and without (c and d) a skin layer.

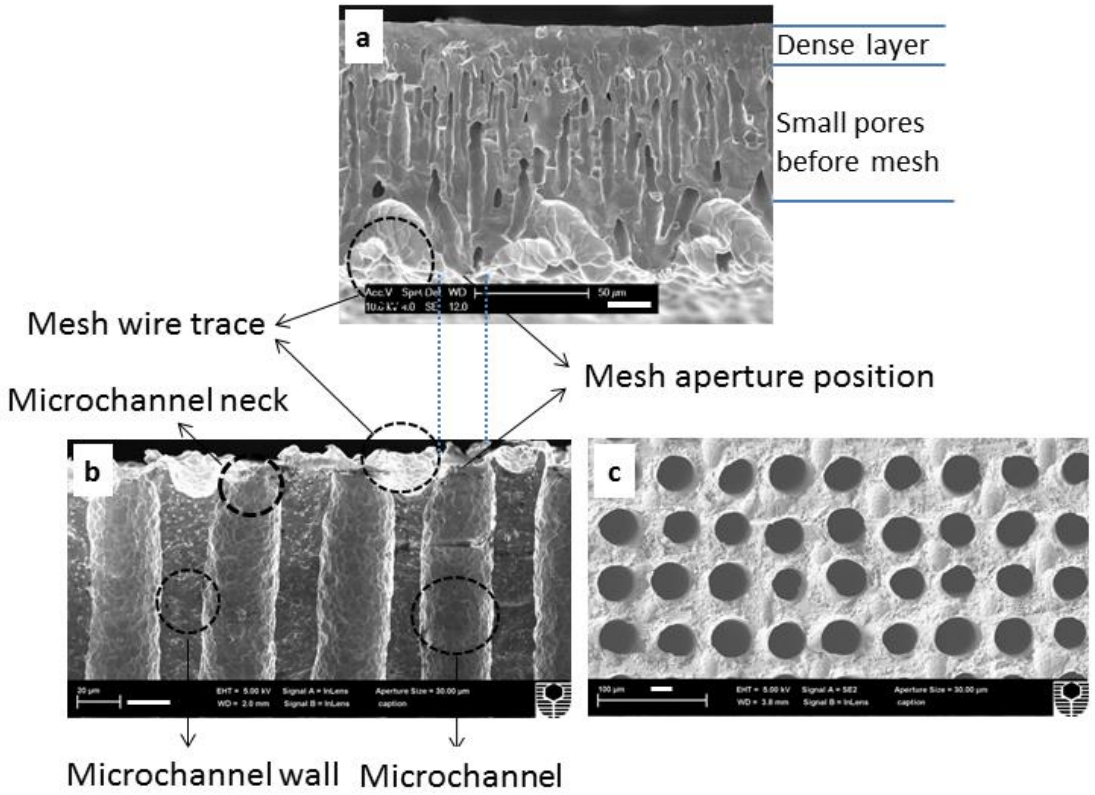

Figure 3-4. SEM images of the cross section of the skin layer removed from the microchanneled membranes by a mesh (a), the top of microchanneled membrane (b) and the membrane surface after polishing away the neck part (c). Scale bar is 20 μm.

To further investigate the possibility of controlling the diameter of microchannels, stainless steel meshes with square aperture sizes of 35, 45 and 55μm were used. The membranes show an increased channel diameter as the mesh aperture size is increased (Figure 3-5). However, the pore shape does not mimic the shape of the mesh apertures. This is because the meshes are made by weaving round stainless steel wires, and a neck of the microchannel forms on the membrane surface (Figure 3-4b). As a result, the surface of the membrane shows the neck parts of the microchannels. After polishing away the neck parts, uniform round pores are revealed (Figure3-4c). The porosity of the membranes varies slightly with increasing pore size, with measured values of 25.2%, 29.4 % and 27.8% for the membranes templated by the meshes with aperture sizes of 35, 45 and 55μm, respectively. This is counter-intuitive, because the porosity would be expected to increase linearly given that the mesh aperture area increases with mesh aperture size (for a constant wire diameter); a possible explanation is that some pores experience greater resistance during the pore channel development, and the resulting shorter pores cause the observed porosity variation.

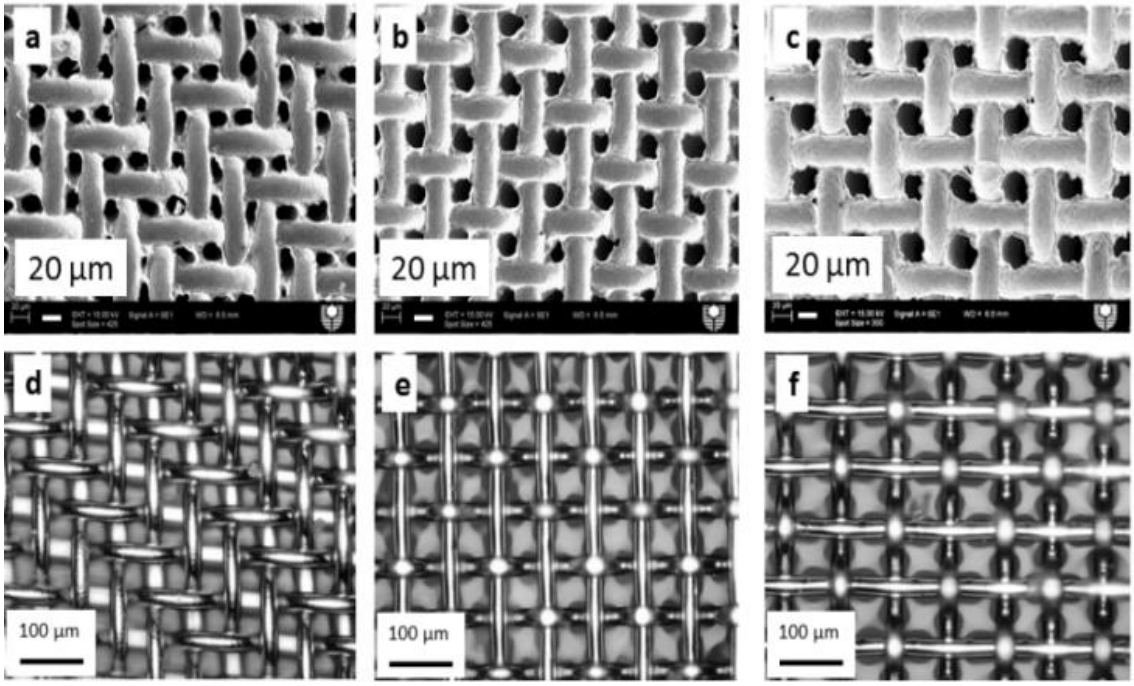

Figure 3-5. The surface SEM images of membranes templated by the meshes with different aperture sizes: a, 35µm; b, 45µm; c, 55µm, and optical microscopy images of the corresponding stainless steel meshes (d-f).

To demonstrate the high oxygen permeation performance of the new membranes, microchanneled membranes templated by the mesh with an aperture size of 45µm were tested. It is known that oxygen exchanges on the sweep gas side and the feed gas side make different contributions to the overall oxygen permeation process [8]. In consideration of the asymmetric membrane structure, the membrane was tested in two configurations: sweep gas was applied to the microchannel side (SOP model) and the dense side (SOD model), as shown in Figure 3-7. In addition, the membrane with a skin layer was also tested for comparison.

Figure 3-6 shows the OPFs of membranes with and without a skin layer over the temperature range of 700-1100 °C. The membranes without a skin layer clearly produced higher OPFs than the membrane with a skin layer. For example, the microchanneled membrane without a skin layer shows an OPF of 3.1 ml cm^{-2} min^{-1} at 1100 °C, which is 2.6 times that of the membrane with a skin layer (1.2 ml cm^{-2} min^{-1}). It is believed that the oxygen permeation is controlled by a surface reaction step at low temperatures, whereas at high temperatures it is determined by the combination of bulk diffusion and surface reaction.[8, 18] Compared with the membranes with a skin layer, the membrane without a skin layer possesses a shorter oxygen

ion bulk diffusion distance and a larger membrane surface area located within the microchannels, which are directly accessible to the oxygen gas. Thus, the high OPFs are attributed to the new membrane microstructure.

As expected, the membrane without a skin layer showed different oxygen permeation performances when it was tested under the SOP and SOD models. The test under the SOD model showed higher OPFs than that under the SOP model, especially at high temperatures (i.e. 3.1 and 2.2 ml cm^{-2} min^{-1} for the SOD model and the SOP model, respectively at 1100 °C). According to Wagner's equation:

$$J_{O_2} = \frac{\delta_e \delta_i}{16F^2 L(\delta_e+\delta_i)} \ln\left(\frac{P'_{O_2,feed}}{P''_{O_2,sweep}}\right) \qquad (3\text{-}3)$$

The OPF is influenced by oxygen partial pressures on the feed gas side and the sweep gas side. For the feed gas side, both models have the same oxygen partial pressure P_A considering the high concentration of oxygen in air and low oxygen permeation fluxs. On the contrary, for the sweep gas side the oxygen partial pressure within micochannels (P_P) for the SOP model is higher than the oxygen partial pressure in the sweep gas (P_S) for the SOD model due to diffusion resistance within the micro-channels, i.e. $P_P > P_S$. Accordingly, P_A/P_P is smaller than P_A/P_s. The OPF in the SOP model is determined by P_A/P_P while the OPF in the SOD model is determined by P_A/P_s. Therefore, the test under the SOP model has a lower oxygen effective partial pressure difference than the test under the SOD model, which is possibly due to the diffusion resistance of molecular oxygen within the microchannels on the sweep gas side (Figure 3-7). A similar phenomenon was observed in conventional membranes supported on porous ceramics.[19] The gas diffusion effect can also be observed from the influence of the sweep gas flow rate on the OPF (Figure 3-8). The OPF of the test under the SOD model kept increasing with the flow rate of the sweep gas even at 450 ml min^{-1}, because increasing the flow rate of the sweep gas could effectively reduce the oxygen partial pressure on the sweep gas side of the membrane. On the contrary, the OPF of the test under the SOP model increased slightly with gas flow rate and subsequently became stable when the sweep gas flow rate reached 360 ml min^{-1}. Therefore, the oxygen permeation process under the SOP model can be concluded to be limited by oxygen diffusion within the microchannels.

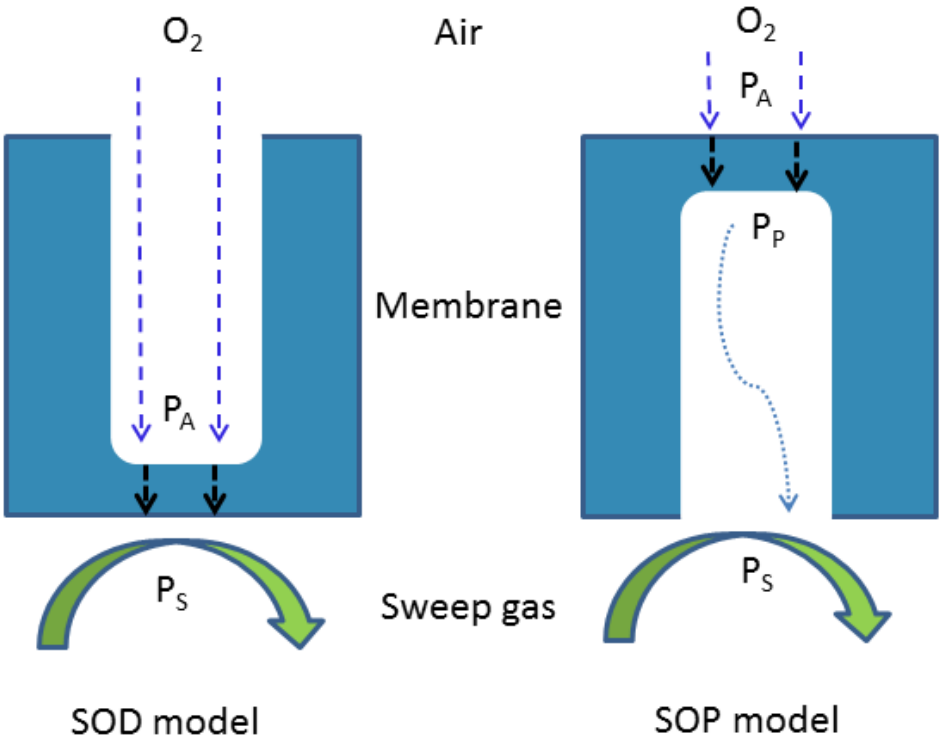

Figure 3-6. Schematic representation of different test models of oxygen permeation through the microchanneled membrane.

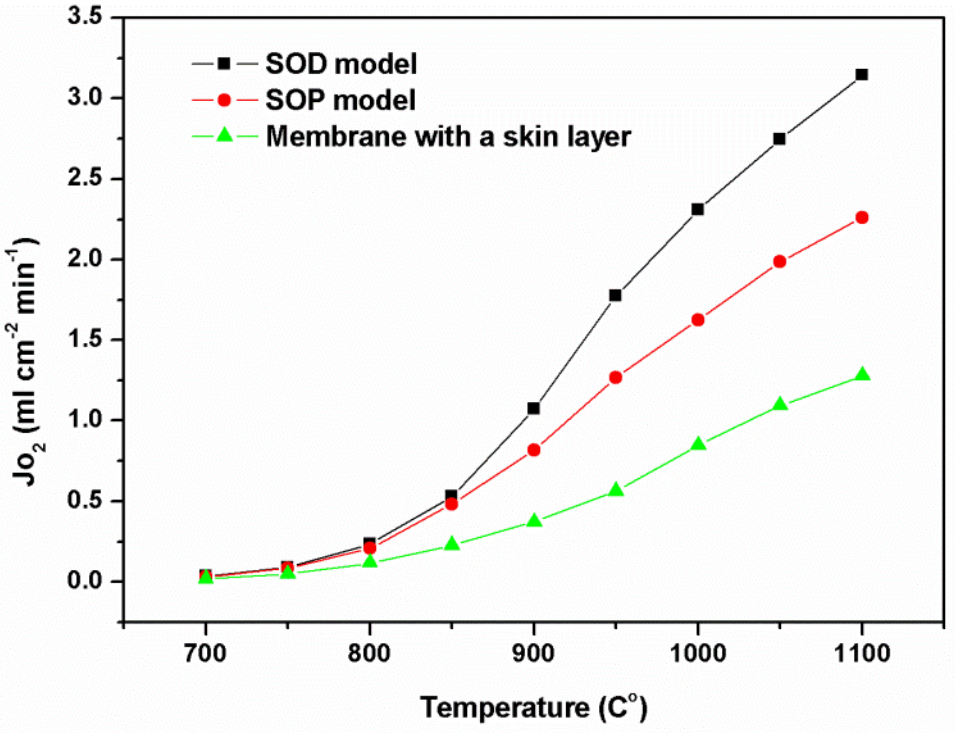

Figure 3-7. The OPF dependence on temperature at a sweep gas flow rate of 270 ml min^{-1} for the microchanneled membranes under the SOD model and the SOP model, and the membrane with a skin layer.

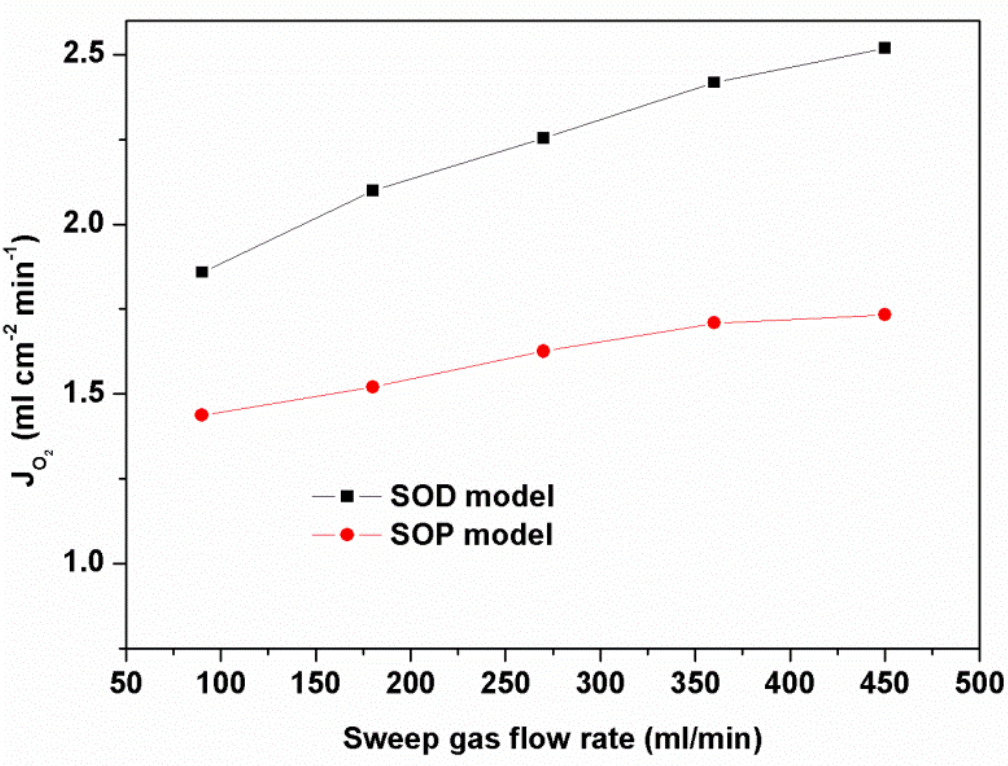

Figure 3-8. The effect of sweep gas flow rate on the OPF at 1000 °C tested under the SOP model and SOD model over the microchanneled membrane.

In order to compare the new membranes and conventional dense membranes, dense disc membranes were prepared by pressing the same LSCF powders and sintering at the same temperature, resulting in the almost dense membranes with the same thickness as the microchanneled membranes. The OPF of the new membrane is above 5 times of that of the dense disc membrane at all testing temperatures (Figure 3-9). We also found that the membrane with a skin layer showed higher OPFs than the dense membrane. This indicates that the extra surface reaction processes in the membrane with a skin layer compete well with the long bulk diffusion distance of the dense membrane in the achievement of high OPFs. For the same membrane material, the microchanneled membrane demonstrated much higher OPFs than that reported for conventional dense membranes (Figure 3-10a).[20-22] The oxygen permeation performances of the microchanneled membranes are even comparable with those of hollow fibre membranes with wall thicknesses of 250-300 μm (Figure 3-10b),[16, 23] and are only lower than those of ultra-thin hollow fibre membranes (90 - 200 μm).[15, 24] For mechanical strength, the microchanneled membrane showed a three-point bending strength of 96.5MPa, much higher than 19.42 MPa measured from the disk membrane fabricated using $SrCo_{0.4}Fe_{0.6}O_3$.[25]

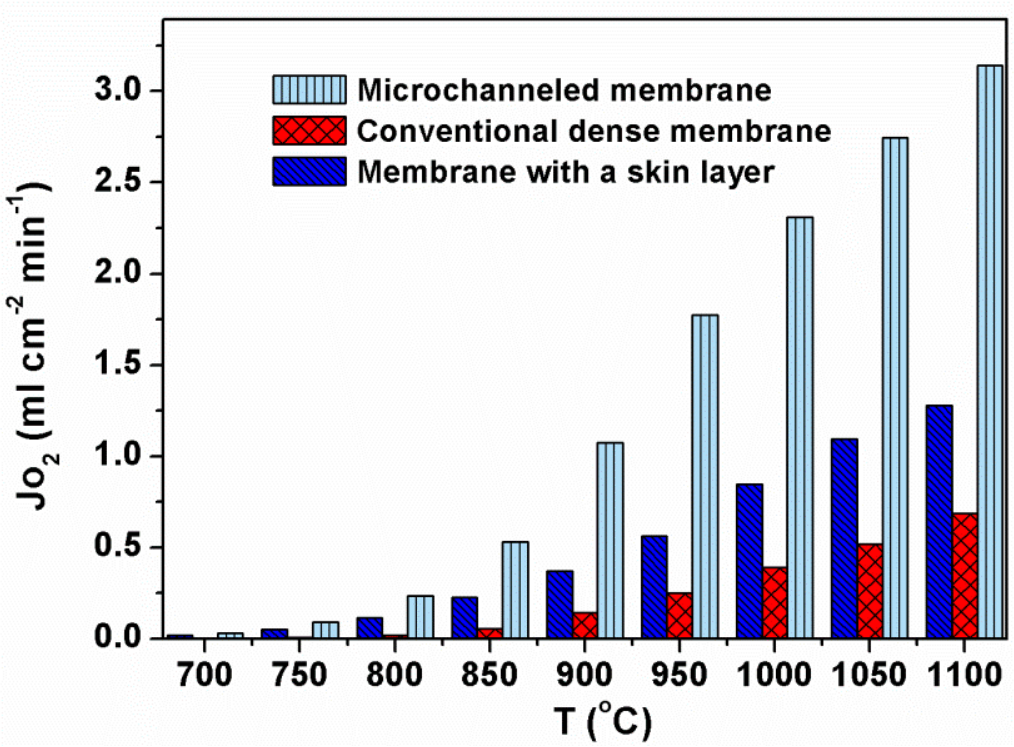

Figure 3-9. The OPF comparison of different membranes in this study.

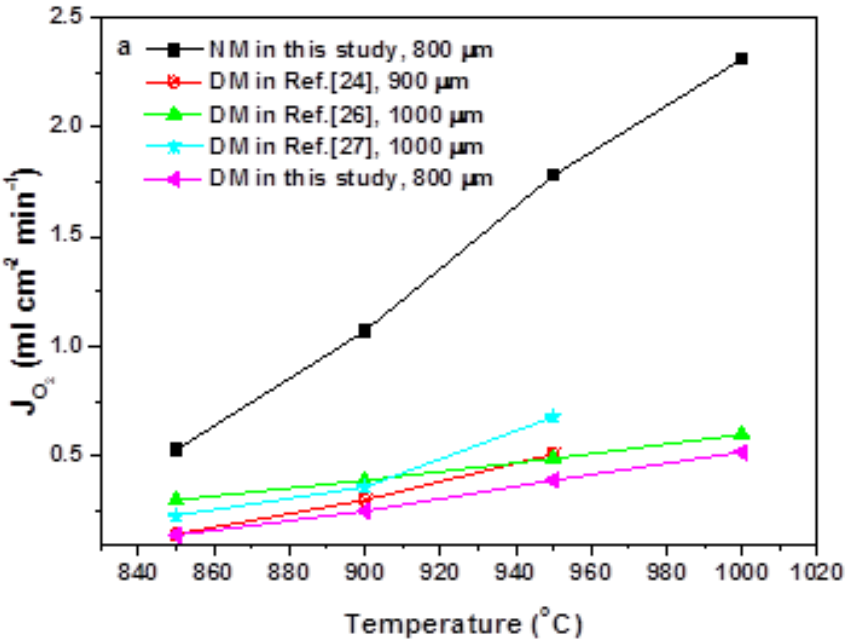

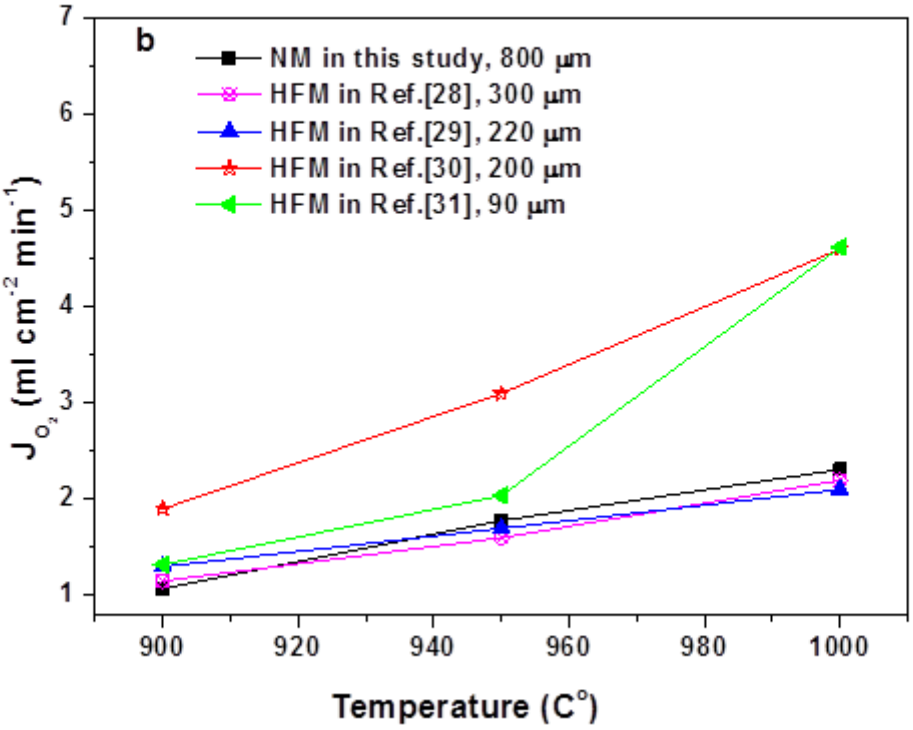

Figure 3-10. The OPF comparisons of the new membrane (NM) developed in this study with (a) conventional dense membranes (DM)[24, 26, 27] and (b) hollow fibre membranes (HFM).[28-31] The thicknesses of membranes were indicated in the figure.

3.4 Conclusions

A microchanneled membrane has been developed by a modified phase inversion process. With the aid of a mesh, the skin layer of the membrane was removed to open pore channels. Moreover, the pore channel development during phase inversion was templated by the mesh apertures, resulting in a short oxygen ion transfer distance and an enlarged membrane surface area. The oxygen permeation membrane with the novel microstructure showed a high OPF of 3.1 ml cm^{-2} min^{-1} at 1100 °C, which is more than 5 times of that of a conventional dense membrane as a result of the novel membrane microstructure. The microchanneled membranes can potentially enhance a range of applications involving gas-phase reactions, such as solid oxide fuel cells, micro-reactors and gas-catalytic processes.[32] The developed technique can also be used to prepare polymer membranes with improved performances in (ultra)filtration and desalination.[33]

3.5 References

1. C. Y. Park, T. H. Lee, S. E. Dorris and U. Balachandran, *International Journal of Hydrogen Energy*, 2010, **35**, 4103-4110.
2. W. L. Zhu, W. Han, G. X. Xiong and W. S. Yang, *Catalysis Today*, 2005, **104**, 149-153.
3. X. Y. Tan and K. Li, *Ind. Eng. Chem. Res.*, 2006, **45**, 142-149.
4. X. L. Dong, W. Q. Jin, N. P. Xu and K. Li, *Chemical Communications*, 2011, **47**, 10886-10902.
5. H. H. Wang, C. Tablet, A. Feldhoff and J. Caro, *Advanced Materials*, 2005, **17**, 1785-1788.
6. S. Engels, F. Beggel, M. Modigell and H. Stadler, *Journal of Membrane Science*, 2010, **359**, 93-101.
7. J. Hong, P. Kirchen and A. F. Ghoniem, *Journal of Membrane Science*, 2012, **407**, 71-85.
8. S. J. Xu and W. J. Thomson, *Chemical Engineering Science*, 1999, **54**, 3839-3850.
9. C. Yacou, J. Sunarso, C. X. C. Lin, S. Smart, S. M. Liu and J. C. D. da Costa, *Journal of Membrane Science*, 2011, **380**, 223-231.
10. D. Poulidi, C. Anderson and I. S. Metcalfe, *Solid State Ionics*, 2008, **179**, 1347-1350.
11. A. Leo, S. M. Liu and J. C. D. da Costa, *Journal of Membrane Science*, 2009, **340**, 148-153.
12. K. Watenabe, M. Yuasa, T. Kida, Y. Teraoka, N. Yamazoe and K. Shimanoe, *Advanced Materials*, 2010, **22**, 2367-2370.
13. A. Julian, E. Juste, P. M. Geffroy, V. Coudert, S. Degot, P. Del Gallo, N. Richet and T. Chartier, *Journal of Membrane Science*, 2009, **333**, 132-140.
14. S. Baumann, J. M. Serra, M. P. Lobera, S. Escolastico, F. Schulze-Kuppers and W. A. Meulenberg, *Journal of Membrane Science*, 2011, **377**, 198-205.

15. B. Zydorczak, Z. T. Wu and K. Li, *Chemical Engineering Science*, 2009, **64**, 4383-4388.

16. Z. G. Wang, H. Liu, X. Y. Tan, Y. G. Jin and S. M. Liu, *Journal of Membrane Science*, 2009, **345**, 65-73.

17. X. Y. Tan, N. Liu, B. Meng and S. M. Liu, *Journal of Membrane Science*, 2011, **378**, 308-318.

18. K. Watanabe, M. Yuasa, T. Kida, K. Shimanoe, Y. Teraoka and N. Yamazoe, *Chemistry of Materials*, 2008, **20**, 6965-6973.

19. X. F. Chang, C. Zhang, X. L. Dong, C. Yang, W. Q. Jin and N. P. Xu, *J. Membr. Sci.*, 2008, **322**, 429-435.

20. Y. Zou, W. Zhou, S. M. Liu and Z. P. Shao, *Journal of the European Ceramic Society*, 2011, **31**, 2931-2938.

21. A. A. Asadi, A. Behrouzifar, M. Iravaninia, T. Mohammadi and A. Pak, *Ind. Eng. Chem. Res.*, 2012, **51**, 3069-3080.

22. P. Y. Zeng, R. Ran, Z. H. Chen, H. X. Gu, Z. P. Shao, J. C. D. da Costa and S. M. Liu, *J. Membr. Sci.*, 2007, **302**, 171-179.

23. X. Y. Tan, Z. G. Wang and K. Li, *Ind. Eng. Chem. Res.*, 2010, **49**, 2895-2901.

24. Y. Zou, W. Zhou, S. Liu and Z. Shao, *Journal of the European Ceramic Society*, 2011, **31**, 2931-2938.

25. S. Lia, W. Jin, N. Xu and J. Shi, *Journal of Membrane Science*, 2001, **186**, 195-204.

26. A. A. Asadi, A. Behrouzifar, M. Iravaninia, T. Mohammadi and A. Pak, *Industrial & Engineering Chemistry Research*, 2012, **51**, 3069-3080.

27. P. Zeng, R. Ran, Z. Chen, H. Gu, Z. Shao, J. C. D. da Costa and S. Liu, *Journal of Membrane Science*, 2007, **302**, 171-179.

28. X. Tan, Z. Wang and K. Li, *Industrial & Engineering Chemistry Research*, 2010, **49**, 2895-2901.

29. Z. Wang, H. Liu, X. Tan, Y. Jin and S. Liu, *Journal of Membrane Science*, 2009, **345**, 65-73.

30. N. Liu, X. Tan, B. Meng and S. Liu, *Separation and Purification Technology*, 2011, **80**, 396-401.

31. B. Zydorczak, Z. Wu and K. Li, *Chemical Engineering Science*, 2009, **64**, 4383-4388.

32. M. H. D. Othman, N. Droushiotis, Z. T. Wu, G. Kelsall and K. Li, *Advanced Materials*, 2011, **23**, 2480-2483.

33. G. R. Guillen, Y. J. Pan, M. H. Li and E. M. V. Hoek, *Ind. Eng. Chem. Res.*, 2011, **50**, 3798-3817.

This work has been published on Journal of Materials Chemistry A. I sincerely acknowledge the co-authors in this study, Dr. Dehua Dong, Professor Gordon Parkinson, Professor Chun-Zhu Li, for their assistance and guidance.

Chapter 4. Microstructure control of oxygen permeation membranes with templated microchannels

4.1 Introduction

The phase-inversion process has been widely used to prepare polymer membranes for many applications, such as gas separation, pervaporation, reverse osmosis for desalination, (ultra)filtration and membrane distillation.[1-4] Membranes formed by phase-inversion generally have three types of microstructure: a skin layer, finger-like pores and sponge-like pores.[5] The skin layer has small pores, acting as the membrane function layer, for example salt rejection in desalination. The finger-like pores could reduce the flowing resistance of fluids passing through the membranes.

Finger-like pores and sponge-like pores are formed beneath the skin layer through the convection of coagulant and solvent: coagulant penetrates into the slurry and solvent enters into the coagulant bath through the skin layer.[6] High convection rates result in the formation of finger-like pores while sponge-like pores are generally formed after a slow convection process.[2, 7] The convection rate is determined by the driving force of the convection and the resistance of pore growth.[8] The driving force is related to the miscibility between the coagulant and the solvent, and a higher miscibility leads to a higher convection rate.[7, 9, 10] A number of coagulants have been investigated as a partner of solvents such as 1-Methyl-2-pyrrolidinone (NMP), dimethyl formamide (DMF) and tetrahydrofuran (THF), and water is a good coagulant for the formation of finger-like pores because of the high miscibility of water with these solvents.[9] Some researchers added a solvent to the water to adjust the miscibility so as to study the effect of coagulant property on membrane microstructure.[10] The resistance is determined by the viscosity of the polymer solution, which depends on polymer concentration.[11] Temperature also influences the convection rate through changing polymer solution viscosity, with increasing temperature reducing the solution viscosity.[12]

In contrast to polymer membranes, ceramic membranes with oxygen ion conductivity show 100% selectivity to oxygen and complete rejection of nitrogen in oxygen separation from air.

[13, 14] The phase-inversion process has also been developed for the formation of ceramic membranes by adding ceramic powders into the polymer solution. The polymer-ceramic composite membranes can be transformed into ceramic membranes after burning off the polymer and sintering the ceramic green bodies, and the ceramic membranes have demonstrated high performances in oxygen separation, solid oxide fuel cells and catalytic reactions.[15-17] However, the method has mainly been used to prepare hollow fibre ceramic membranes having very thin walls (less than 500 μm) to reduce the oxygen permeation/gas diffusion distance. The hollow fibre membranes are formed by extruding/spinning slurry into a coagulant bath with simultaneously applying bore coagulant. As a result, phase-inversion occurs on both sides of the membranes, forming a complicated microstructure: two skin layers, and a central layer sandwiched by two groups of finger-like pores.[15] The skin layers and the central layer are densified through removing the sponge-like pores by sintering to form the dense layers that achieve oxygen separation through ion transport. The existence of finger-like pores embedded within membranes partly interrupts oxygen ion diffusion. Moreover, they reduce the mechanical strength of the membranes, which is a major concern for the practical application of hollow fibre membranes.[18]

Chapter 3 describes the development of a novel microchanneled ceramic membrane formed by a mesh-assisted phase-inversion process.[19] The flat membrane was formed by casting slurry into a mould and subsequently applying a coagulant on top of the slurry. The plate membrane has a simplified microstructure through removing the skin layer by the use of a mesh. Furthermore, it produced uniform microchannels instead of finger-like pores beneath the mesh. The location and sizes of the microchannels were templated by the mesh apertures. Open microchannels traverse the membrane, with the other end terminating at a thin dense layer. The microchanneled structure not only substantially reduces the oxygen permeation distance within the thin layer, but also provides a large membrane surface area located within the microchannels. As a result, the oxygen permeation flux increased by a factor of greater than 5 compared with that of conventional dense membranes. During the membrane preparation, coagulant and slurry affect the microchannel growth *via* convection rate. Although the preparation process of hollow fibre membranes using phase-inversion has been well-studied, the parameters studied, such as gas-gap and the flow rate of internal coagulant, are not applicable to the template phase-inversion process, and moreover do not cover the parameters studied here, such as the method of applying coagulant and solids loading. Furthermore, the templated uniform microchannels in the membranes studied here provide a

strong basis to help identify the influences of the various parameters. In this chapter, the effects on microchannel structure of the method of applying coagulant, coagulant solubility, phase-inversion time, solid loading and polymer concentration in the slurry are investigated to control the membrane microstructure for achieving highly-efficient oxygen separation. The formation mechanism of microchannels is also proposed to understand the structure formation.

4.2 Experimental

4.2.1 Materials

Commercial $La_{0.6}Sr_{0.4}Co_{0.2}Fe_{0.8}O_{3-\delta}$ powder (LSCF-6428, Fuel Cell Materials, Ohio, USA) with a surface area of 5.1 m^2/g was used as a membrane material. Polyethersulfone (PESF, Radel-A300) and Polyvinylpyrrolidone (PVP, MW=40000) provided by Sigma-Aldrich were used as polymer and dispersant, respectively. NMP (99%) purchased from Acros organics was the solvent in this study. Tap water, ethanol (99%, Thermal Fisher Scientific Inc.), the mixture of water and ethanol (weight ratio of 7:3) and isopropanol (99.5%, Thermal Fisher Scientific Inc.) were used as coagulants. Ceramic adhesive (552-VFG, Aremco Products Inc., USA) was employed as a sealant.

4.2.2 Membrane preparation

In order to investigate the effects of polymer concentration and solid loading on membrane microstructure, PESF concentration was defined as the weight ratio of PESF to NMP, and solid loading was defined as the weight ratio of LSCF to LSCF+NMP+PESF. Firstly, PESF and PVP (added at a concentration equal to 0.7 wt% of the LSCF powder) were dissolved into NMP solvent by magnetic stirring. Then, the prepared polymer solution was mixed with the calculated amount of LSCF powder based on the solid loading in a teflon jar. The mixture was ball-milled for 48 hours at a rotation rate of 300 RPM to form a homogeneous slurry. The slurry viscosities were measured at 23 °C using Brookfield DV-2 Pro viscometer.

The green body of the membrane was prepared by a mesh-assisted phase-inversion process, as described in Chapter 3.[19] In the process, after casting the slurry in a module and subsequently inserting into a vacuum chamber to remove bubbles, a stainless steel mesh with

aperture size of 45 μm was immersed just below the slurry surface. After immersion in a coagulant bath for 20 mins or a specific time (referred to as phase-inversion time), the mesh was lifted off to remove the skin layer, forming the membrane green body with open microchannels. The membrane green body was rinsed with water to exchange with the NMP solvent in the pore channels. After drying at 100 °C in an oven for 1 h, the membrane green body was sintered into a ceramic membrane at 1350 °C for 5 hours. To investigate the coagulant effect on the membrane microstructure, the coagulants were applied in different ways and with different compositions, as described below.

4.2.3 Membrane characterization and oxygen permeation test

The membrane microstructure was observed by scanning electron microscopy (SEM, Zeiss Evo 40XVP). Porosity was measured using Archimedes' method. The oxygen permeation test system is shown in Figure. 4-1. The membrane was placed at one end of a quartz tube and sealed by the ceramic adhesive. As the membrane have an asymmetric structure, air flowed to the microchannel side as a feed gas while argon was used as a sweep gas on the dense side of membranes for all tests. The flow rates of the two gases were set at 270 ml min^{-1}. The flow rate of argon was controlled by a mass flow controller (MFC, AALBORG) while a rotameter was used to control the air flow rate. Oxygen concentration in the sweep gas was measured by online gas chromatography (GC, GC-2014, Shimadzu) with a packed column of molecular sieve 5A, and the oxygen permeation flux was calculated using the following equation.

$$J_{O_2} = \frac{F_{Sweep}(C_{O_2} - C_{N_2}\frac{21}{79})}{A} \qquad (4\text{-}1)$$

where J_{O_2} is the oxygen permeation flux, F_{Sweep} is the flow rate of sweep gas, C_{O_2} is the concentration of permeated oxygen in sweep gas, C_{N_2} is the concentration of nitrogen that leaked from the test system into the sweep gas and A is the effective permeation area of the membrane. The effective area is about 0.8 cm^2 in this study. As it is hard to achieve absolute gas-sealing in the test system, the amount of oxygen contributed by leaking was deducted during the calculation. The concentration of the leaked oxygen ($C_{N_2}\frac{21}{79}$) was calculated according to the concentration of the leaked nitrogen (C_{N_2}) measured in the sweep gas and the ratio of oxygen and nitrogen concentrations in air (21/79). The leaked oxygen in all tests was

controlled to within 1% of the total amount of oxygen in the sweep gas to ensure the accuracy of the permeation results.

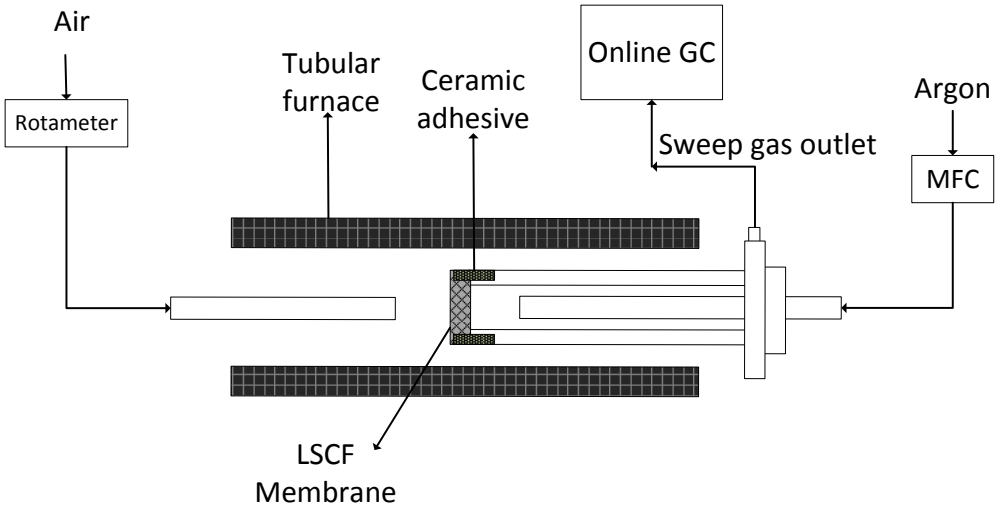

Figure 4-1. Oxygen permeation test system

4.3 Results and discussion

4.3.1 The influence of applying coagulant

The phase-inversion process was initially conducted in a water bath as in a conventional phase-inversion process, as shown in Figure 4-2a. The SEM image of the final ceramic in Figure. 4-3a shows that microchannels only traverse less than the half of the membrane thickness, which might be a consequence of the thickness of the membrane (about 0.8 mm in thickness) compared to that of polymer membranes (about 0.3 mm in thickness)[11] and hollow fibre ceramic membranes (e.g. 0.2 mm in thickness).[20] However, it is believed that microchannel (finger-like pore) growth depends on the driving force of the convection of coagulant and solvent.[6]

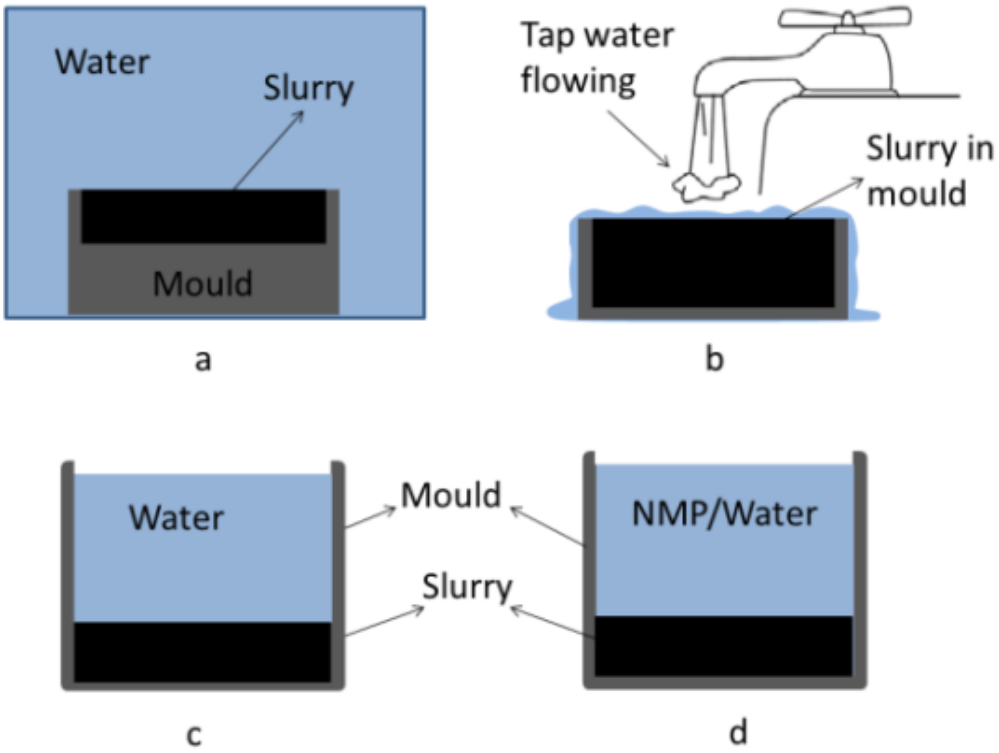

Figure 4-2. Phase-inversion using different methods of applying coagulant: (a) conventional water bath; (b) flowing water; (c) 5ml of water; (d) 5ml of 25 wt% NMP/water.

Compared with the miscibility between coagulant and solvent, the concentration of coagulant at the interface between slurry and coagulant has a more direct effect on the driving force of the convection and therefore microchannel growth. To our knowledge, there has been no reported study investigating this effect.

In order to investigate the effect, three methods of applying coagulant were designed, as shown in Figure 4-2. Figure 4-2b shows that flowing water was used as a coagulant bath, which retained a constant and high concentration of water at the interface during phase-inversion. Secondly, 5 ml of water was applied on the slurry surface, and there was a natural gradient of water concentration decreasing from the top of the water bath to the interface as the convection proceeded (Figure. 4-2c). This is very different from conventional phase-inversion using a water bath (a large amount of water, e.g. several litres). In conventional phase-inversion, NMP solvent exiting from the slurry can be diluted by a large amount of water or flow down to the bottom of the water bath because of a slightly higher density compared to water. Lastly, 5 ml of 25 wt% NMP/water mixture was used to decrease the concentration of water in the coagulant as well as at the interface (Figure. 4-2d).

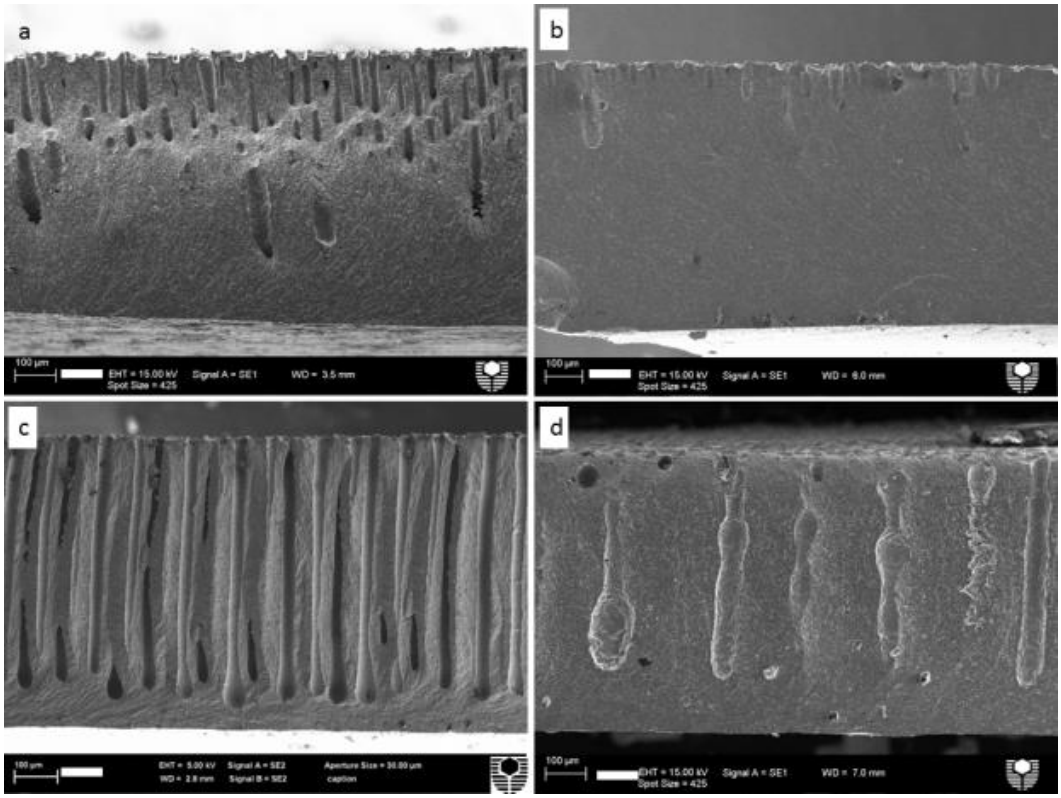

Figure 4-3. SEM images of membrane cross sections (a-d) made using the different methods of applying coagulant demonstrated in Figure. 4-2(a-d) correspondingly. The scale bars are 100 μm.

Figure. 4-3 shows the microstructure of the final ceramic membranes prepared by the different methods of applying coagulant. Long microchannels almost traversing the membrane were formed using 5 ml of water (Figure. 4-3c). In contrast, the coagulant with high and low water concentrations at the interface produces very short and/or small numbers of microchannels (Figure. 4-3b and 4-3d). The high concentration of water at the interface results in a thick skin layer, which restrains the convection process and leads to the formation of short pore channels; a skin layer cannot be formed at the low concentration of water in coagulant and the formation of a skin layer is essential for the formation of microchannels (finger-like pores).[10] Therefore, a thin skin layer formed at a suitable water concentration at the interface is critical to forming long microchannels within membranes.

4.3.2 The effect of coagulant

As the miscibility between solvent and coagulant drives the convection of solvent and

coagulant, the coagulant solubility is expected to affect the microchannel formation in this study. Four coagulants were used, and their solubility parameters are listed in Table 4-1.[21, 22] The solubility parameter δ has been divided into a dispersive term δ_d, a polar term δ_p and a hydrogen bond term δ_h. For the mixture of water and ethanol, the values were calculated according to the following equations: [9]

$$\delta_d = x_w\delta_{d,w} + x_e\delta_{d,e} \qquad (4\text{-}2)$$

$$\delta_h = x_w\delta_{h,w} + x_e\delta_{h,e} \qquad (4\text{-}3)$$

$$\delta_p = x_w\delta_{p,w} + x_e\delta_{p,e} \qquad (4\text{-}4)$$

Where x_w and x_e are the volume fractions of water and ethanol in the mixture. The solubility was calculated using the following equation:

$$\delta = \sqrt{\delta_d^2 + \delta_p^2 + \delta_h^2} \qquad (4\text{-}5)$$

Δδ is the solubility difference between the substance and NMP, and the difference determines the miscibility between coagulant and NMP. The higher Δδ indicates the larger driving force of the convection of NMP and coagulant. As shown in Figure. 4-4, the largest Δδ of water coagulant resulted in the longest microchannels, while the smallest solubility difference between NMP and isopropanol coagulant produced the shortest and the least amount of microchannels due to the lowest driving force. In addition, the lower driving force of the convection required the longer time to complete the phase-inversion (Table 4-1). Therefore, the solubility of coagulant greatly affects the membrane microstructure via driving microchannel growth.

Table 4-1. Solubility parameters and phase-inversion time.[23, 24]

Substance	δ_d	δ_p	δ_h	δ	$\Delta\delta$ to NMP	Phase-inversion time (mins)
NMP	18.0	12.3	7.2	22.9	N/A	N/A
Water	15.5	16.0	42.3	47.8	24.9	20
Water/ethanol(7:3)	15.6	13.8	35.4	41.0	18.1	20
Ethanol	15.8	8.8	19.4	26.5	3.6	25
Isopropanol	15.8	6.1	16.4	23.5	0.6	35

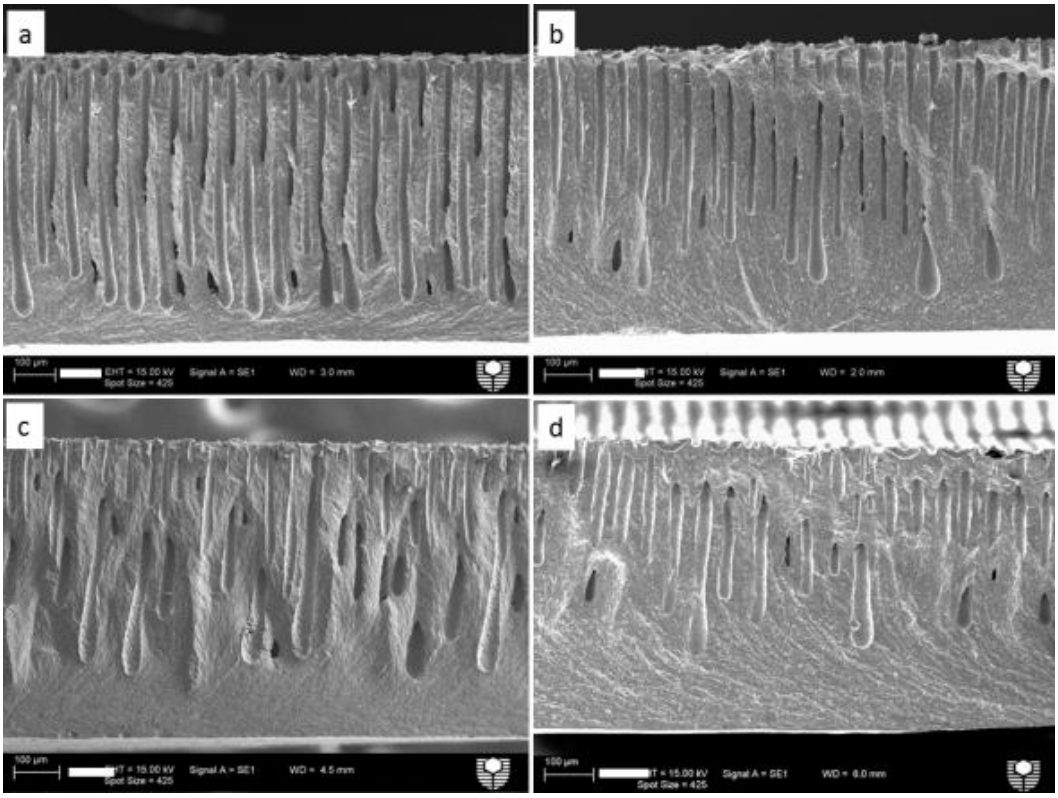

Figure 4-4. SEM images of membrane cross sections made with different coagulants: a, water; b, water/ethanol mixture (volume ratio of 7:3); c, ethanol; d, isopropanol. The scale bars are 100 μm.

4.3.3 The effect of phase-inversion time

As microchannels (finger-like pores) are formed during the rapid convection process, and sponge-like pore formation occurs at low convection rates, phase-inversion time is expected

to affect the membrane microstructure. To confirm that the microchannel structure was formed during the phase-inversion time and no further structure change occurred during rinsing with water and drying, immediately after one of the membranes was formed, it was removed and frozen with dry ice (-78.5 °C) and dried under vacuum. The SEM images of the membranes prepared by the two ways show there was no difference in microchanneled structure except the membrane thickness (Figure 4-5). When plenty of water was used to exchange with NMP in the microchannels, the high concentration of water quickly solidified the interface between the slurry and channels comparable to skin layer formation and therefore finalized this membrane microstructure. During the conventional drying process, membrane green bodies experience the capillary force induced by the evaporation of NMP/water liquid, which causes shrinkage of the green bodies, referred to as drying shrinkage. However, this did not occur during freeze-drying green bodies under vacuum. As a result, the membrane green bodies treated by freeze-drying are thicker than those dried by conventional liquid evaporation, resulting in the thicker ceramic membranes.

Figure. 4-5 also shows the membrane microstructure formed after different phase-inversion times. It is noted that the membrane could not be completely solidified within a time of less than 20 mins because that would not give enough time for the phase-inversion to propagate to the bottom of slurry. It can be seen in Figure 4-5 that the longest pore channels were formed in the membrane after phase-inversion for 20 mins (Figure. 4-5a). However, the microchannels became short when the phase-inversion time increased to 90 mins (Figure. 4-5b). Some microchannels even disappeared after phase-inversion for 240 mins (Figure. 4-5c). This phenomenon reveals that the formation of microchannels is reversible during the phase-inversion, and Jin et al. reported the same phenomenon in the preparation of ceramic supports as anodes of solid oxide fuel cells by a phase-inversion process.[9] It is possible that microchannels were formed within 20 mins via rapid convection, whereafter the convection of NMP and water would continue with decreasing NMP diffusion rate. When the amount of water entering into the slurry becomes more than the amount of NMP diffusing into the pore channels, the slurry volume would increase and the pore channel volume decrease, leading to the microchannel structure degradation. Therefore, under certain conditions, the microchannel formation is reversible. In consideration of long microchannel formation, the optimized phase-inversion time is 20 mins in this study.

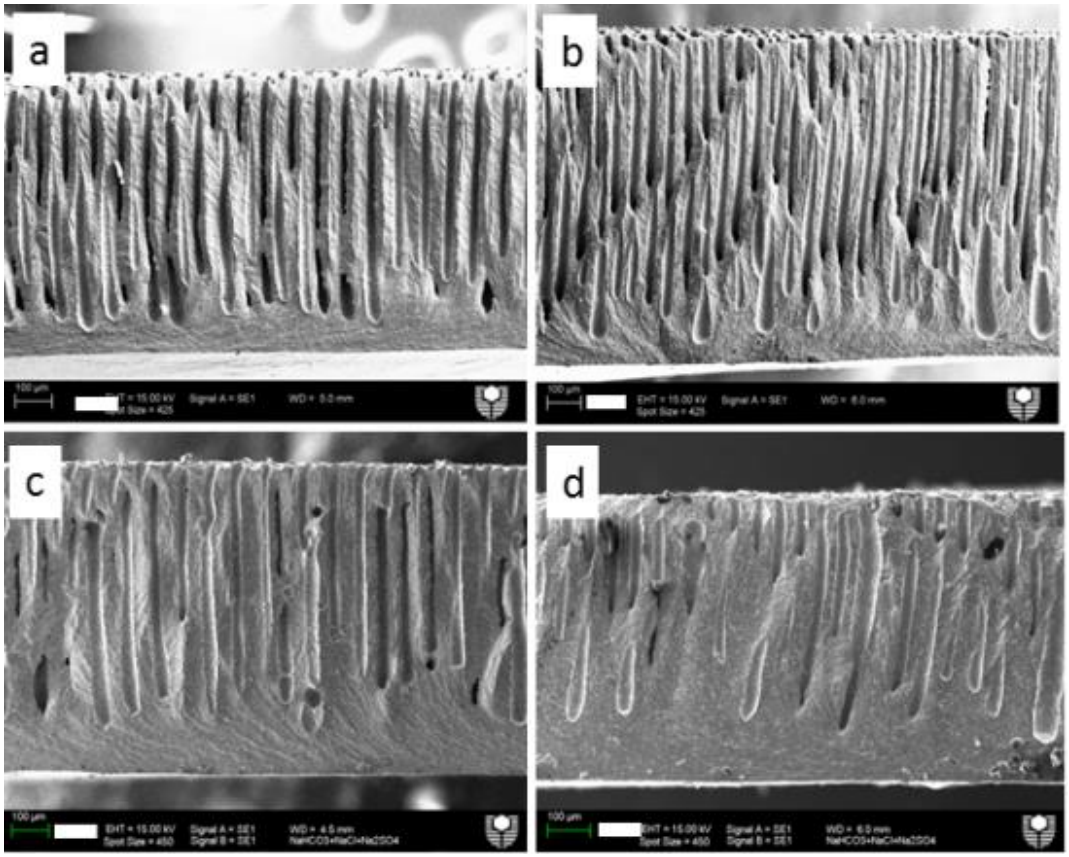

Figure. 4-5. SEM images of the cross section of membranes formed at different phase-inversion times: (a and b), 20 mins by conventional drying (a) and freeze-drying (b); (c), 90 mins; (d), 240 mins. The scale bars are 100 µm.

4.3.4 The effect of PESF concentration

To investigate the formation of microchanneled ceramic membranes, PESF was dissolved in NMP solvent, and ceramic powders were dispersed in the solution to form a slurry. During phase-inversion, PESF precipitated from solvent and solidified the slurry. Microchannels were formed by the high rates of the convection between NMP and water. PESF concentration affected the slurry viscosity and in turn the microchannel structure in terms of the resistance to the microchannel growth. When the PESF concentration in the PESF/NMP solution was below 15 wt%, the formed membrane was not strong enough for handling at the solid loading of 60 wt%. The PESF concentration was investigated in the range from 15 to 35 wt% in this study.

Figure 4-6 shows the cross section of membranes prepared at different PESF concentrations.

The longest and most uniform microchannels were obtained at the PESF concentration of 20 wt%. It is attributed to the lowest viscosity of slurry and therefore the lowest resistance of microchannel growth (Figure 4-7), which confirms that high convection rates are beneficial for producing microchannel structure. Increasing the PESF concentration generally increased the slurry viscosity as is the case in polymer solution.[2] However, the slurry viscosity decreased when the PESF concentration was increased from 15 wt% to 20 wt%. This is because a certain amount of PESF polymer absorbed on the ceramic particle surfaces, acting as a dispersant for ceramic particles. As a result, the slurry viscosity was decreased. Excessive PESF increased viscosity when PESF adsorption on ceramic particles was saturated.[25]

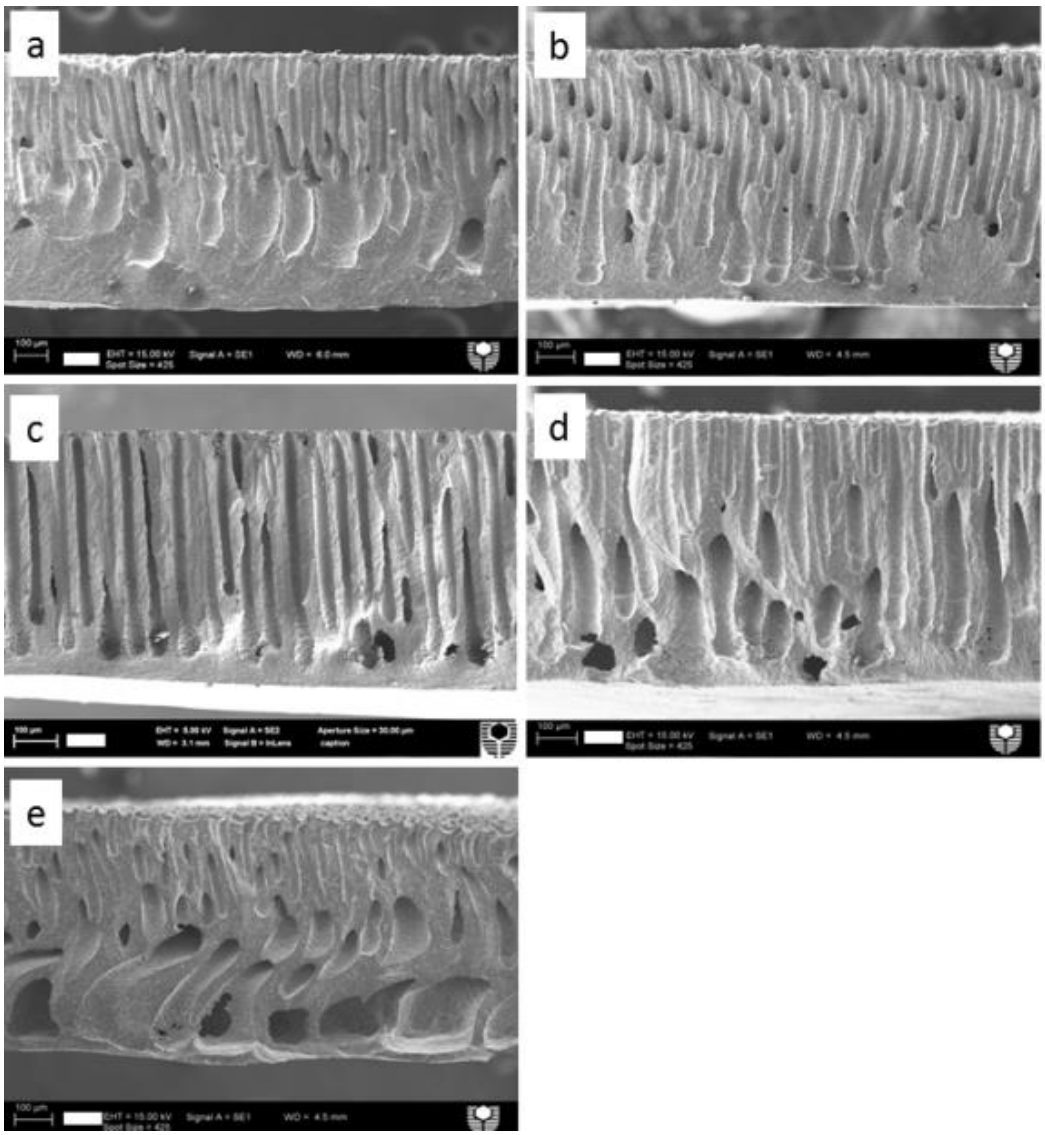

Figure 4-6. SEM images of cross sections of membranes made from slurries with different PESF concentrations: (a) 15 wt%, (b) 17 wt%, (c) 20%, (d) 25% and (e) 35%. Solid loading of slurry was set at 60 wt%. The scale bars are 100 μm.

Another change in the pattern of the microchannel structure with PESF concentration is observed in Figure. 4-6. With the increase of PESF concentration, the thickness of the dense layer at the bottom of membrane was reduced, which is opposite to that in polymer membrane formation by phase-inversion.[26-28] There are two possible reasons causing the different effects: PESF was burned off during ceramic membrane preparation, leaving a thinner layer at a higher PESF concentration; the presence of hydrophilic ceramic particles in the polymer solution promoted water permeation into the microchannel walls, and in turn the phase-inversion at the bottom. Furthermore, a thicker skin layer was formed at a higher PESF concentration,[11, 26] and it restrained the flow of NMP from the microchannels into the water bath. However, this has less effect on water flow from the water bath into the microchannels because it has a smaller molecular dimension than that of NMP.[29] As a result, the accumulated NMP and water at the bottom of the slurry forms macrovoids, resulting in a higher porosity (Figure. 4-7). Thereby, The microchannels turned into macrovoids as the PESF concentration was increased, and the same result was reported in a previous study.[30]

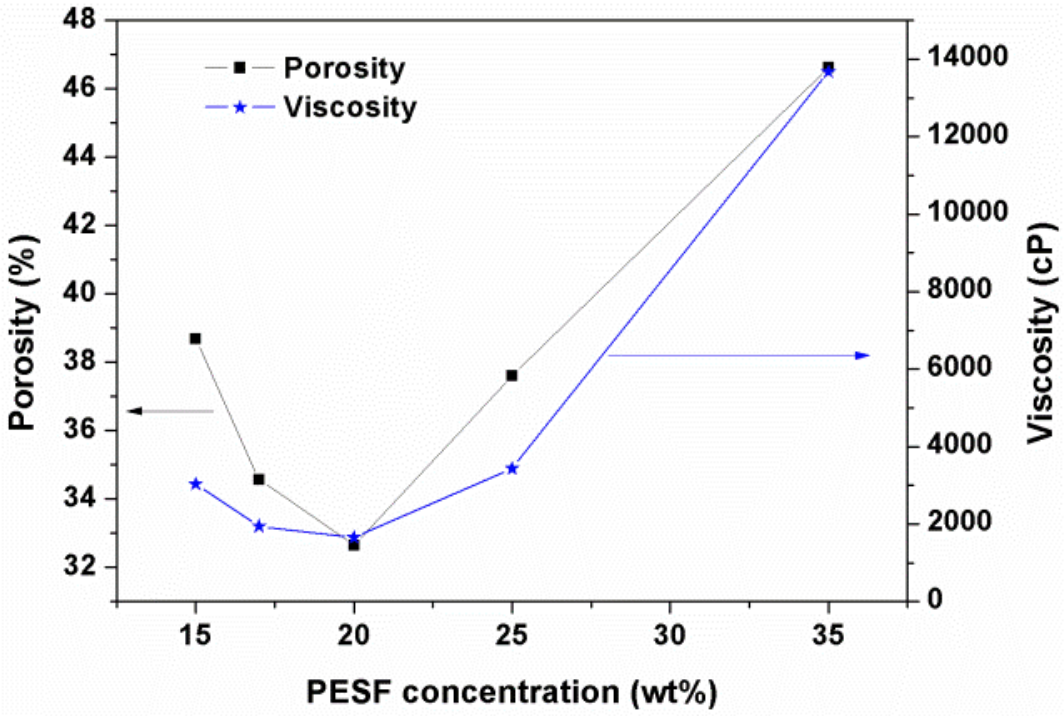

Figure 4-7. Slurry viscosity and membrane porosity as functions of PESF concentration.

As the oxygen permeation rate is determined by the oxygen ion bulk diffusion and membrane surface reaction,[31] both the thickness of the dense layer and membrane surface area affect the

oxygen permeation rate. The oxygen permeation fluxes (OPFs) of the membranes are shown in Figure. 4-8 as a function of PESF concentration. Although the membrane made with a 35 wt% PESF slurry has the thinnest dense layer (about 50μm) and the highest porosity (46.6%), the OPF of the membrane (0.018 mol m^{-2} s^{-1} at 1050 °C) is lower than that (0.030 mol m^{-2} s^{-1}) of the membrane made with a 20 wt% PESF solution. This is attributed to the large membrane surface area within numerous uniform microchannels of the 20 wt% PESF membranes because when microchannels are in similar length scale, the membrane with smaller porosity should present larger surface area. Therefore, at a PESF concentration of 20 wt%, the formed membrane has the optimized microchannel structure for oxygen permeation.

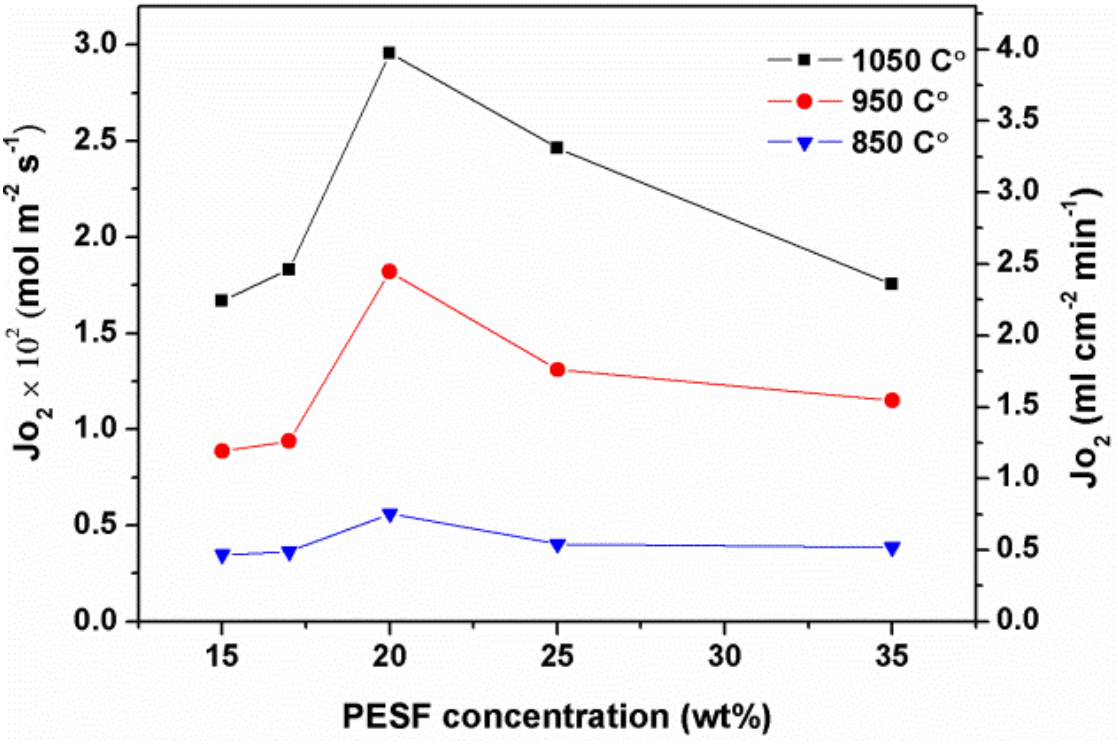

Figure 4-8. OPFs of the membranes formed from slurries with different PESF concentrations.

4.3.5 The effect of solid loading

Solid loading affects slurry viscosity and is therefore likely to influence membrane microstructure in a similar manner to the PESF concentration. With a fixed PESF concentration of 15 wt%, the solid loading effect was investigated from 60 to 80 wt% because the membranes collapsed during sintering when the solid loading was less than 60

wt%. Interestingly, increasing solid loading reduced the slurry viscosity up to a solid loading of 70 wt%, whereas slurry viscosity generally increases with solid loading. This is consistent with the suggested role of PESF by adsorbing on the ceramic particle surfaces, as mentioned above. Above the solid loading of 70 wt%, slurry viscosity increases with solid loading because of the lack of PESF as a dispersant. According to the magnitudes of viscosity variation in Figure 4-7 and Figure 4-9, the polymer concentration has a much more significant effect on slurry viscosity than the ceramic powder loading.[5] This is the reason that the PESF concentration was fixed at 15 wt% in this study, where the slurry has a moderate viscosity and the formed microchannels crossed about a half of the membrane thickness. Accordingly, the membrane microstructure variation caused by solid loading can be easily observed by SEM imaging and characterized by OPFs.

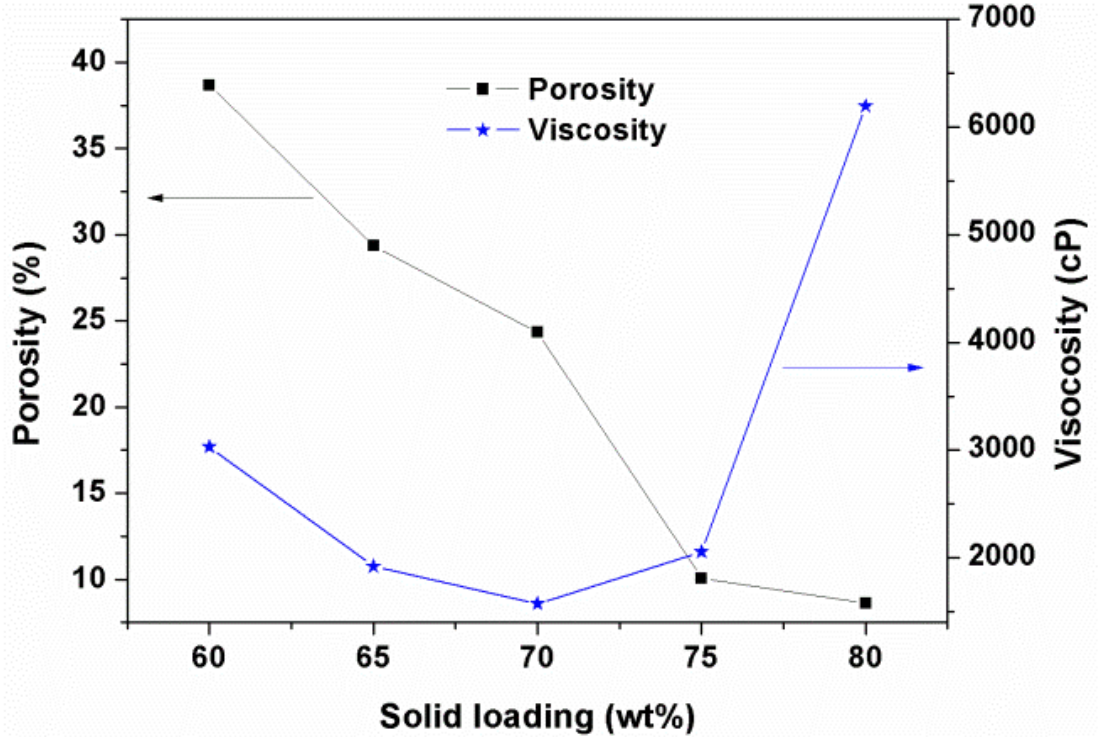

Figure 4-9. Slurry viscosity and membrane porosity as functions of solid loading.

The ceramic membrane porosity decreased from 38.8% to 8.6% when the solid loading was increased from 60 to 80 wt%. The porosity of 24.4 % at the solid loading of 70 wt% is similar to or less than that of a conventional porous ceramic support, but it should have higher gas diffusion efficiency in terms of eliminating the pore tortuosity that occurs in conventional porous ceramic supports.[32]

Figure 4-10 shows that the longest and most uniform microchannels in membranes were formed from a slurry with a solid loading of 70 wt% and the lowest viscosity (Figure. 4-9). From Figures 4-6 and 4-10, at a solid loading of 60 wt% and a PESF concentration of 15 wt%, microchannels merged into big channels, which are not found at higher PESF concentrations or higher solid loadings. The possible reason is that the rapidly- formed microchannel wall at the low PESF concentration or solid loading is not strong and can be collapsed during the subsequent slow phase-inversion process. As expected, the highest OPF of the membranes was achieved at a solid loading of 70 wt% owing to the uniform and long microchannels. It reached 0.027, 0.015 and 0.005 mol m^{-2} s^{-1} (3.63, 2.02 and 0.71 ml cm^{-2} min^{-1}) at 1050, 950 and 850 °C, respectively (Figure. 4-11), these values being much higher than those of disc/plate membranes with the same LSCF material reported in the literature.[19]

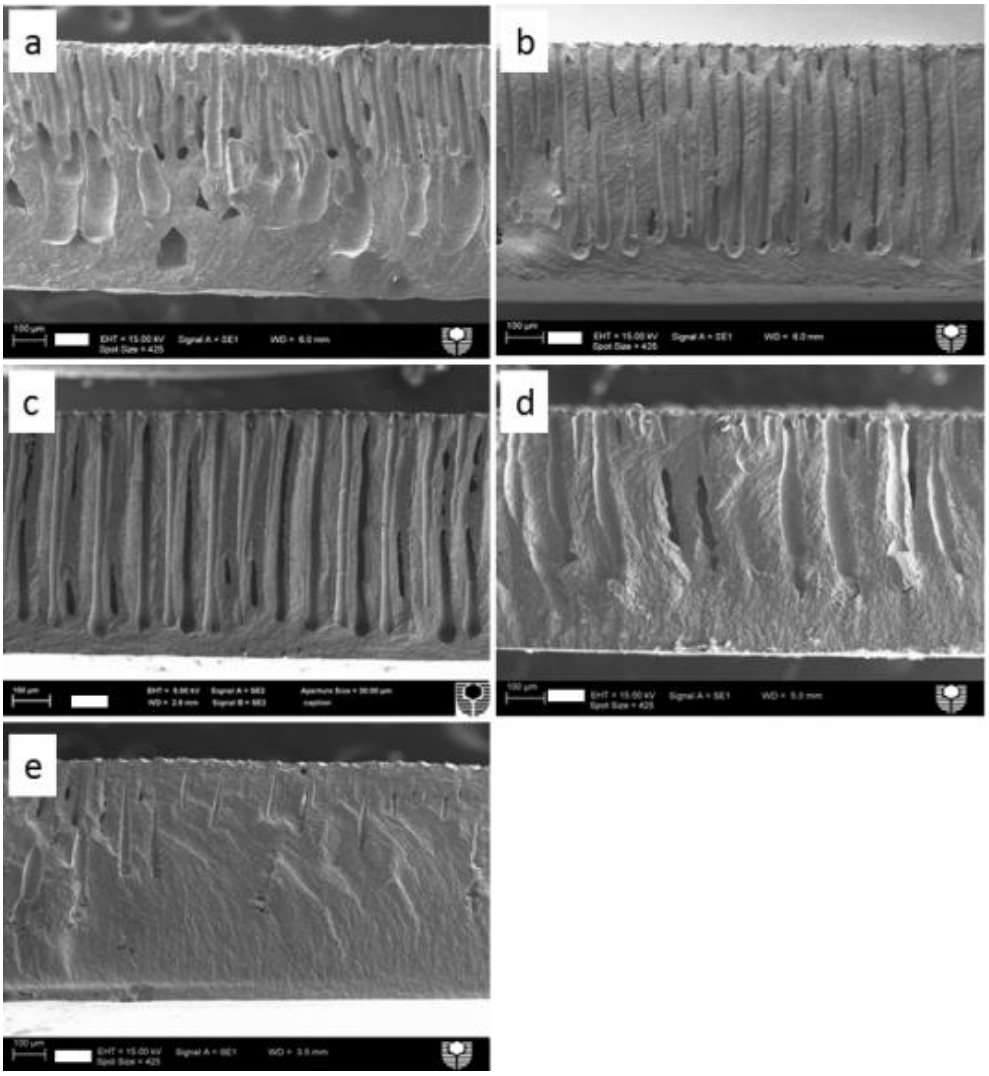

Figure 4-10. Cross section images of membranes made from slurries with different solid loadings: (a), 60 wt%; (b), 65 wt%; (c), 70 wt%; (d), 75 wt%; (e), 80% while polymer concentration was maintained at 15 wt%. The scale bars are 100μm.

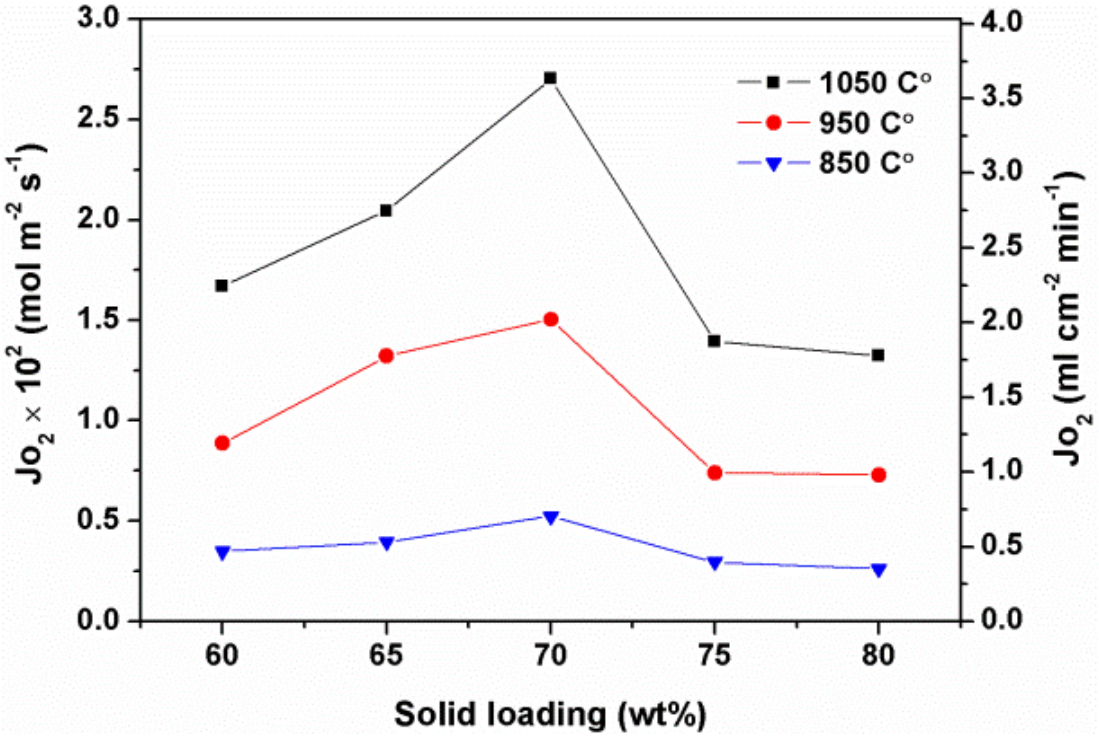

Figure 4-11. OPFs of membranes made from slurries with different solid loadings.

4.4 Formation mechanism of microchanneled structure

4.4.1 Templating microchannels

The formation mechanism of the pore structure within the membranes prepared by phase-inversion process has been mainly studied previously on polymer membrane preparation,[5, 7, 10] and a few studies have investigated the effect of preparation parameters on the microstructure of ceramic membranes.[9, 33] As a new templated phase-inversion process, the templated uniform microchannels provide a strong basis for studying the formation mechanism of the microchanneled structure.

The asymmetric structure of the membranes is generally formed by two steps.[29] Firstly, a dense skin layer is formed due to the rapid desolvation of NMP from the slurry into water when slurry contacts with the coagulant. The skin layer restrains the convection of NMP and water because of its high density, which is indispensable for the formation of the pore channel structure in the sublayer. In the second step, a small amount of water enters into the slurry through the skin layer, forming a nucleus of polymer-poor phase as nascent pores.[10]

NMP in the slurry enters into the pores, driven by the miscibility between NMP and water. As a result, pore channels grow when the convection of NMP and water continues. In our templating process, the small pore channels below the skin layer were templated by mesh apertures into uniform channels when the pore channel growth approached the mesh template (Figure. 4-12). After completion of the phase-inversion, the layer above the mesh template was removed via lifting off the mesh, leaving open, uniform microchannels. The microstructures of the templated membrane and the removed skin layer are shown in Figure. 4-13. As proposed in Figure. 4-12, numerous small pore channels (about 10 μm in diameter) were combined into uniform microchannels about 40 μm in diameter by the mesh apertures. Therefore, the mesh has a two-fold role in the formation of the microchanneled structure: templating microchannels and removing the skin layer.

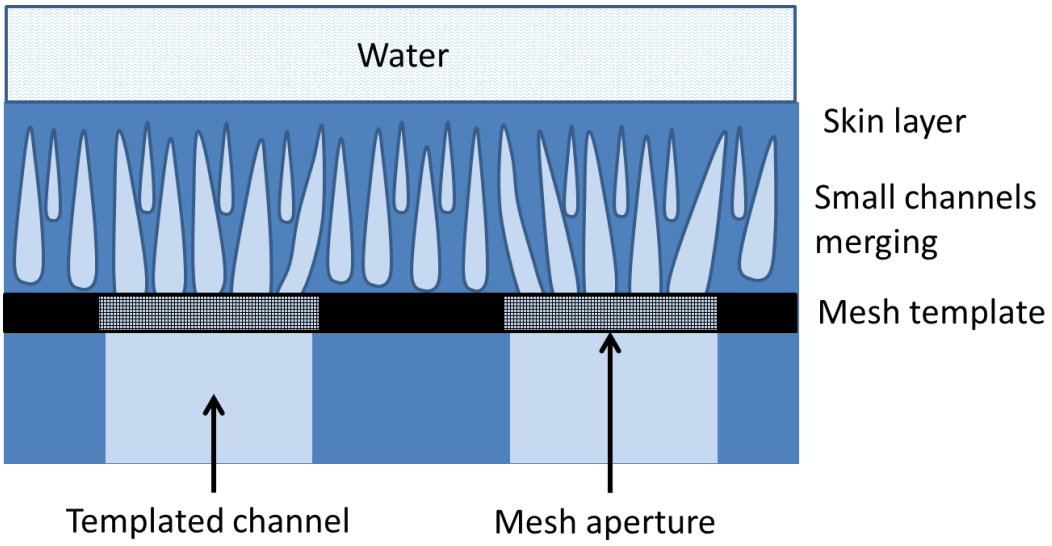

Figure 4-12. Schematic representation of templating microchannels by mesh apertures during the phase-inversion process.

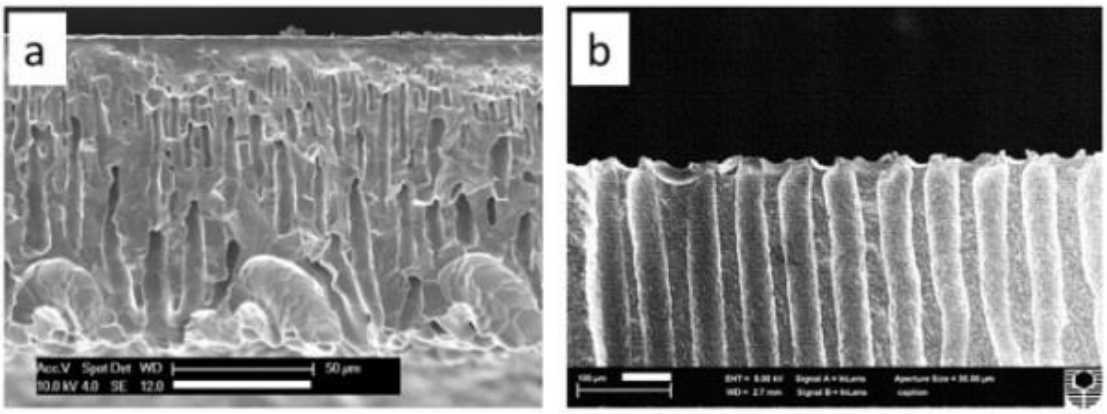

Figure 4-13. SEM images of pore channels above (a) and below (b) the mesh template within a ceramic membrane prepared by the templated phase-inversion process. The scale bars are 50 μm.

4.4.2 Microchannel growth

As the mesh apertures produce uniform microchannels, the channels have an equal opportunity to grow via extracting NMP from the surrounding slurry. The channel growth is directed by NMP availability, which causes the channels to cross the membrane. Accordingly, the convection/diffusion rates of NMP and coagulant at the head of the channels determine the channel growth,[7, 10] as shown in Figure. 4-14. If the diffusion rate of NMP into the channels is greater than the diffusion rate of water from the channels into the slurry, the channels will grow because the slurry volume shrinks and the channel volume expands. If the two diffusion rates are equal, the channels will stop growing. The pore channels can be shortened when the NMP diffusion rate is lower than the water diffusion rate due to the volume changes. During phase-inversion, the water diffusion from pore channels into the slurry is restrained by the water diffusion through the dense skin layer and within the microchannels. Consequently, the water diffusion rate at the pore channel head is much lower than the NMP diffusion rate, which makes the pore channels grow quickly. This is the reason that a skin layer is indispensable for the pore channel formation. The channels keep growing until the NMP diffusion rate reduces to the value which is close to the water diffusion rate. Therefore, the channel growth is largely determined by the NMP diffusion rate.

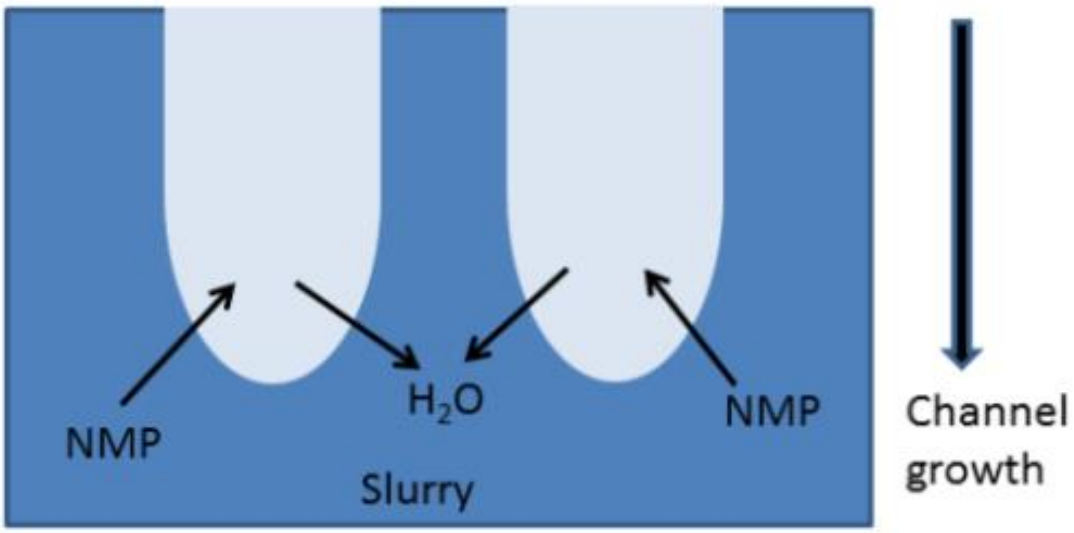

Figure 4-14. The proposed mechanism for the microchannel growth.

The miscibility between NMP and coagulant is the driving force of the NMP diffusion, while the NMP diffusion experiences resistance within the slurry.[8] In the above studies, the driving force was adjusted by using coagulants with different solubilities. When the solubility difference between NMP and coagulant was decreased, the microchannels became shorter because of the smaller driving force. The viscosity affects the NMP diffusion from the slurry into pore channels, and the higher viscosity leads to larger resistance to the NMP diffusion.[33] Our studies have shown that the slurry viscosity was affected by the PESF content and the solid loading of ceramic powders. The longest microchannels were formed at the lowest slurry viscosities because these gave the lowest resistances to the NMP diffusion. As shown above, the immersion time also affected the microstructure. After phase-inversion for 20 mins, the NMP diffusion rate was reduced to the level of the water diffusion rate and the pore channel growth was automatically stopped with a NMP-poor slurry layer because of the absence of NMP in the slurry, forming the longest microchannels. If the phase-inversion time was more than 20 mins, the amount of water entering into the slurry is more than the amount of NMP diffusing into pore channels because of the decrease of NMP diffusion rate, which caused the slurry to expand and the microchannels to shorten. The proposed formation mechanism is consistent with the experimental results obtained in this study. Thus, the microchannel formation is driven by the miscibility between NMP and water and the NMP diffusion determines the microchannel growth, which is affected by coagulant solubility and slurry viscosity.

4.5 Conclusions

The process of templated phase-inversion has been studied to control the microstructure of a microchanneled membrane for oxygen separation. A suitable coagulant concentration at the interface between coagulant and slurry to form a thin skin layer is essential for the formation of long microchannels. The coagulant solubility affects the microchanneled structure because the miscibility between NMP and coagulant is the driving force of the microchannel growth. As the microchannel formation is in some cases reversible, the optimized phase-inversion time is 20 mins for water coagulant in this study. Both polymer concentration and solid loading of ceramic powder affect the microchannel structure, which influences the resistance of microchannel growth *via* slurry viscosity. The slurry with the lowest viscosity formed the longest and most uniform microchannels, which were produced in the membrane that showed the highest oxygen permeation flux. Based on the results, a formation mechanism of microchannels has been proposed: mesh apertures template microchannels and microchannel growth is mainly attributed to rapid NMP diffusion from the slurry into pore channels, which is driven by the miscibility between NMP and coagulant and resisted by the slurry.

4.6 References

1. G. R. Guillen, Y. J. Pan, M. H. Li and E. M. V. Hoek, *Industrial & Engineering Chemistry Research*, 2011, **50**, 3798-3817.
2. H. Strathmann, K. Kock, P. Amar and R. W. Baker, *Desalination*, 1975, **16**, 179-203.
3. H. A. Tsai, L. D. Li, K. R. Lee, Y. C. Wang, C. L. Li, J. Huang and J. Y. Lai, *Journal of Membrane Science*, 2000, **176**, 97-103.
4. D. L. Wang, W. K. Teo and K. Li, *J. Membr. Sci.*, 2002, **204**, 247-256.
5. H. Strathmann and K. Kock, *Desalination*, 1977, **21**, 241-255.
6. M. A. Frommer and R. M. Messalem, *Industrial & Engineering Chemistry Product Research and Development*, 1973, **12**, 328-333.
7. C. A. Smolders, A. J. Reuvers, R. M. Boom and I. M. Wienk, *Journal of Membrane Science*, 1992, **73**, 259-275.

8. A. J. Reuvers, J. W. A. Vandenberg and C. A. Smolders, *Journal of Membrane Science*, 1987, **34**, 45-65.

9. C. Jin, C. H. Yang and F. L. Chen, *Journal of Membrane Science*, 2010, **363**, 250-255.

10. T. H. Young and L. W. Chen, *Desalination*, 1995, **103**, 233-247.

11. Z. H. Zhang, Q. F. An, Y. L. Ji, J. W. Qian and C. J. Gao, *Desalination*, 2010, **260**, 43-50.

12. Q. Z. Zheng, P. Wang and Y. N. Yang, *Journal of Membrane Science*, 2006, **279**, 230-237.

13. X. F. Zhu, S. M. Sun, Y. F. He, Y. Cong and W. S. Yang, *Journal of Membrane Science*, 2008, **323**, 221-224.

14. S. S. Madaeni, E. Enayati and V. Vatanpour, *Polym. Adv. Technol.*, 2011, **22**, 2556-2563.

15. B. Zydorczak, Z. T. Wu and K. Li, *Chemical Engineering Science*, 2009, **64**, 4383-4388.

16. F. R. Garcia-Garcia, M. A. Rahman, B. F. K. Kingsbury and K. Li, *Appl. Catal. A-Gen.*, 2011, **393**, 71-77.

17. M. H. D. Othman, N. Droushiotis, Z. T. Wu, G. Kelsall and K. Li, *Adv. Mater.*, 2011, **23**, 2480-+.

18. X. L. Dong, W. Q. Jin, N. P. Xu and K. Li, *Chemical Communications*, 2011, **47**, 10886-10902.

19. X. Shao, D. H. Dong, G. Parkinson and C.-Z. Li, *J. Mater. Chem. A*, 2013.

20. N. Liu, X. Y. Tan, B. Meng and S. M. Liu, *Separation and Purification Technology*, 2011, **80**, 396-401.

21. B. Sellergren and K. J. Shea, *Journal of Chromatography*, 1993, **635**, 31-49.

22. A. Agrawal, A. D. Saran, S. S. Rath and A. Khanna, *Polymer*, 2004, **45**, 8603-8612.

23. B. Sellergren and K. J. Shea, *Journal of Chromatography A*, 1993, **635**, 31-49.

24. A. Agrawal, A. D. Saran, S. S. Rath and A. Khanna, *Polymer*, 2004, **45**, 8603-8612.

25. D. H. Dong, J. F. Gao, X. Q. Liu and G. Y. Meng, *Journal of Power Sources*, 2007, **165**, 217-223.

26. Z. S. Li and C. Z. Jiang, *J. Polym. Sci. Pt. B-Polym. Phys.*, 2005, **43**, 498-510.

27. M. H. D. Othman, N. Droushiotis, Z. T. Wu, G. Kelsall and K. Li, *J. Power Sources*, 2011, **196**, 5035-5044.

28. C. Stropnik, L. Germic and B. Zerjal, *J. Appl. Polym. Sci.*, 1996, **61**, 1821-1830.

29. T. H. Young and L. W. Chen, *Journal of Membrane Science*, 1991, **57**, 69-81.

30. J. Barzin, S. S. Madaeni, H. Mirzadeh and M. Mehrabzadeh, *Journal of Applied Polymer Science*, 2004, **92**, 3804-3813.

31. S. J. Xu and W. J. Thomson, *Chemical Engineering Science*, 1999, **54**, 3839-3850.

32. C. J. Bae, C. K. Erdonmez, J. W. Halloran and Y. M. Chiang, *Adv. Mater.*, 2013, **25**, 1254-1258.

33. B. F. K. Kingsbury and K. Li, *Journal of Membrane Science*, 2009, **328**, 134-140.

This work has been published on Journal of Materials Chemistry A. I sincerely acknowledge the co-authors in this study, Dr. Dehua Dong, Professor Gordon Parkinson, Professor Chun-Zhu Li, for their assistance and guidance.

Chapter 5. Improvement of oxygen permeation through microchanneled ceramic membranes

5.1. Introduction

Currently, industrial oxygen production mainly relies on a cryogenic process, which requires both a large capital investment and high operating costs.[1] A potentially cheaper technology, using oxygen permeation membranes to separate oxygen from air, is a process that is driven by the difference between the oxygen the partial pressures on two sides of the membrane.[2, 3] More benefits can be delivered when the technology is coupled with high temperature reactions such as methane conversion and oxyfuel combustion.[4, 5] The technology has been developed for nearly 30 years since Teraoka et al. demonstrated oxygen permeation through perovskite ceramics in 1985.[6] However, the technology has not been commercialized so far because the oxygen fluxes achieved have been too low or high performance materials such as $Ba_{0.5}Sr_{0.5}Co_{0.8}Fe_{0.2}O_{3-\delta}$ show low long-term stability and resistance to poisoning.

Oxygen permeation through ceramic membranes is generally rate-limited by surface reactions on the membrane surfaces and/or bulk diffusion within the membranes; the dominant factor varies with temperature. According to the Wagner equation (Eq. 1),

$$J_{O_2} = \frac{\delta_e \delta_i}{16F^2 L(\delta_e+\delta_i)} \ln\left(\frac{P'_{O_2,feed}}{P''_{O_2,sweep}}\right) \qquad (5\text{-}1)$$

Where J_{O_2} is oxygen flux, F is Faraday constant, δ_e and δ_i are electronic and ionic conductivities, respectively, L is membrane thickness, $P'_{O_2,feed}$ and $P''_{O_2,sweep}$ are the oxygen partial pressures at oxygen feed side and sweep gas side, respectively. The oxygen permeation rate is influenced by membrane thickness (L) and the mixed conductivities (ionic δ_i and electronic δ_e).[2] Some researchers have prepared thin membranes on porous supports to reduce the bulk diffusion distance of oxygen ions.[7] However, the preparation process needs to be carefully controlled to avoid the formation of defects and cracks due to mismatches in the thermal expansion coefficients because they would cause leaks and prevent complete gas separation.[8] Additionally, the high temperature co-sintering of the support and the thin membrane readily densifies the support, increasing gas diffusion resistance within the support.[9] As described in

chapters 3 and 4, a novel microchanneled structure of oxygen permeation membranes was created using a mesh-templating phase inversion method.[10] The membranes contain numerous, parallel microchannels crossing their thickness with one end open and another end stopped by a thin layer. The microchanneled structure greatly increased oxygen flux by a factor of up to 5 compared with conventional dense thick membranes, giving a flux which is higher than results previously reported in the literature. In this study, we further increase the oxygen flux of the microchanneled membrane through employing dual-phase membranes and applying catalysts.

Both the oxygen ionic conductivity and the electronic conductivity of ceramic membranes affect the oxygen permeation. As shown in Equation 2, with the presence of electrons, gaseous oxygen is reduced into oxygen ions on the oxygen rich side.[2]

$$\frac{1}{2}O_2 + V_o^{\cdot\cdot} + 2e^- \rightarrow O^{2-} \qquad (5\text{-}2)$$

where $V_o^{\cdot\cdot}$ is an oxygen vacancy in the ceramic material, e^- is an electron and O^{2-} is an oxygen ion in the lattice structure. When oxygen ions diffuse through a membrane from the oxygen rich side to the oxygen lean side, electrons move in the opposite direction to maintain electrical neutrality within the membrane. Therefore, balanced ionic and electronic conductivities are required to achieve high oxygen fluxes. There are two types of materials used in this study: fluorite and perovskite ceramics. Although the fluorite ceramic such as $Ce_{0.8}Gd_{0.2}O_{2-\delta}$ (GDC) is of much higher oxygen ion conductivity than perovskite ceramic such as $La_{0.6}Sr_{0.4}Co_{0.2}Fe_{0.8}O_{3-\delta}$ (LSCF), the very low electronic conductivity limits its application in oxygen permeation membranes.[11] In contrast, the LSCF has moderate oxygen ionic conductivity and high electronic conductivity, and is widely used in oxygen separation. Some researchers have added the fluorite ceramic into perovskite ceramics to increase their oxygen ionic conductivity, and these are referred as dual-phase membranes.[11-14] The balanced mixed conductivities can be reached via tuning the volume ratio of the two ceramics for achieving high oxygen fluxes. Moreover, fluorite ceramics have higher stability than perovskite ceramics, and therefore using a dual-phase membrane can enhance the membrane stability, which is a critical issue for practical applications. In this study, dual-phase membranes are used to improve the oxygen fluxes of the microchanneled membranes.

In addition, catalysts such as Ag and Pt can greatly accelerate the membrane surface reactions, including oxygen dissociation and oxygen ion combination.[15, 16] In this study, Pt is coated on both sides of the membrane to improve the overall oxygen permeation. The catalyst is delivered to the membrane surface on the microchannel side directly through the microchannels. The effect of the catalyst on the oxygen permeation rate is investigated.

5.2. Experimental

5.2.1 Membrane preparation

To prepare dual-phase membranes, $La_{0.6}Sr_{0.4}Co_{0.2}Fe_{0.8}O_{3-\delta}$ powder (LSCF, Fuel Cell Materials, Ohio, USA) was mixed with $Ce_{0.8}Gd_{0.2}O_{2-\delta}$ powder (GDC, Fuel Cell Materials, Ohio, USA) as a suspension in ethanol by ball milling for 24 hours to form uniform mixtures with the LSCF weight ratios of 20%, 30%, 40% and 50%, respectively. The mixtures were made into disk membrane green bodies by hydraulic pressing under a pressure of 300 MPa, followed by sintering at 1400 °C for 2 h in a box furnace (ModuTemp Pty. Ltd., Australia). According to the LSCF and GDC theoretical densities of 6.35 and 7.31 g/cm^3, LSCF volume ratios in the dense dual-phase membranes are 22.3%, 33.0%, 43.4% and 53.5% corresponding to the LSCF weight ratios of 20%, 30%, 40% and 50%, respectively. Pure LSCF and GDC membranes were also prepared for XRD characterization. The prepared disk membranes were polished by sand paper (P800) to ensure that the membranes had the desired thicknesses. As shown in Figure 5-1, the membrane has different surface morphology before and after polishing. Accordingly, all disk membrane surfaces were polished to ensure consistency.

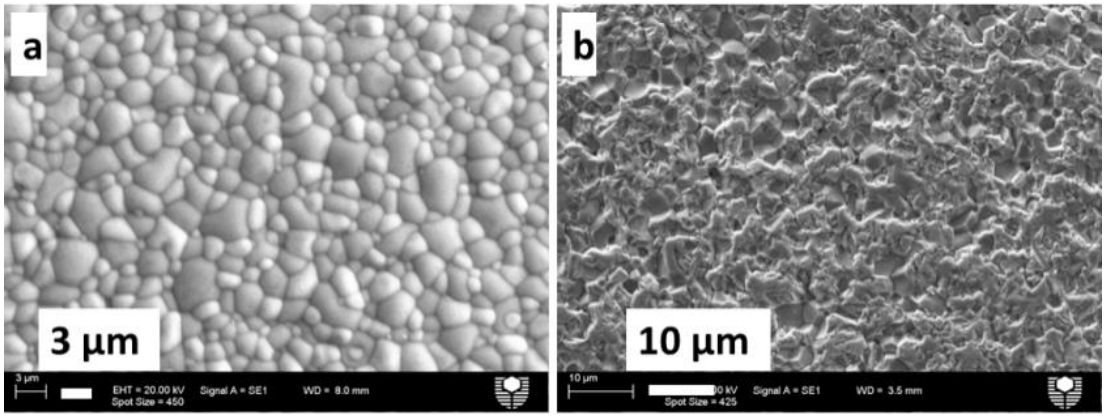

Figure 5-1. SEM images of as-prepared disk membrane surfaces before (a) and after (b) polishing.

The preparation process of microchanneled membranes is described in chapter 3. 0.3 g of polyvinylpyrrolidone (PVP, molecular weight=40000, Sigma-Aldrich, Australia), 2.8 g of polyethersulfone (PESF, Radel-A300, Sigma-Aldrich, Australia) and 14.7 g of 1-methyl-2-pyrrolidinone (NMP, 99%, Acros organics) were mixed in a beaker to achieve a homogeneous solution. The prepared solution was mixed with 30g of the well-mixed powder and then ball milled for 48 h to make a slurry. Microchanneled membranes with a thickness of about 0.8 mm were prepared by using a stainless steel mesh to template the phase inversion process, and the formed membrane green bodies were sintered at 1400 °C for 2 h in the box furnace. For pure LSCF microchanneled membrane preparation, a different slurry component was used to form the membrane having a similar microstructure as the dual-phase membrane.[17] 0.21 g of PVP, 4 g of PESF, 16 g of NMP and 30 g of LSCF powder were used to prepare LSCF slurry using the same process. The membrane green body was sintered at 1350 °C for 5 h.

5.2.2 Catalyst preparation

Platinum catalyst was coated on both sides of the oxygen permeation membranes using different methods for each side because of the asymmetric structure. On the microchannel side, a polymer hydrogel assisted process was used to uniformly coat catalyst on the microchannel walls.[18] Briefly, 10 g of acrylamide monomer, 0.5 g of 1 N, N-methylenebisacrylamide (as a cross linker) and 0.04 g of ammonium persulfate (as an initiator of polymerization) were dissolved in 42 g of deionized water. 0.3 g of platinum chloride was dissolved into the above solution to form 0.05 Pt mol/L catalyst precursor. The ceramic membranes were immersed into the catalyst precursor, followed by vacuum treatment to remove air bubbles and heating in an oven set at 55 °C for 1 h to perform monomer polymerization. The membranes were finally taken out from the catalyst hydrogel. After removing the catalyst hydrogel on the dense surface of the membrane using tissue and water for coating catalyst in the next step, the membrane with the catalyst precursor in the microchannels was heated at 950°C for 3 hours.

For the preparation of catalyst on the dense side of membranes, poly(furfuryl alcohol) was used to assist the catalyst coating.[19] Typically, 0.02 mol/L platinum chloride/ethylene glycol solution was mixed with furfuryl alcohol and butanol at the weight ratio of 1:1:0.8. One drop of 10 wt% p-toluenesulfonic acid/ethanol solution was added into the above solution to

initiate polymerization of the furfuryl alcohol. The prepared catalyst precursor was coated on the membrane surface using a spin coater at a rotation rate of 300 RPM, followed by heating in an oven set at 70 ℃ for 3 h to complete the polymerization and subsequently calcination at 950 ℃ for 3 h. All chemicals were used as supplied by Sigma-Aldrich, Australia without further treatment.

5.2.3 Membrane characterization and testing

The membranes were characterized by XRD, using CuKα radiation with a Bruker D8 Advance diffractometer equipped with a LynxEye detector (Bruker-AXS, Karlsruhe, Germany) at a scan rate of 2 °/min and a step size of 0.02°. The membrane microstructure and catalyst morphology were observed using scanning electron microscopes (Zeiss Neon 40EsB FIBSEM and Zeiss Evo 40XVP) and energy dispersive X-ray spectrum (EDX) was conducting at same time.

The ceramic membranes were sealed on one end of a quartz tube using ceramic adhesive (552-VFG, Aremco Products Inc., USA). Argon was used as the sweep gas and air as the feed gas. The oxygen concentration on the sweep side was detected by gas chromatography (Shimadzu 2014, Japan). The oxygen flux was calculated based on Equation 3,

$$J_{O_2} = \frac{F_s(C_{O_2} - C_{N_2}\frac{21}{79})}{\mathrm{A}} \qquad (5\text{-}3)$$

where J_{O_2} is the oxygen flux of the membranes, F_s is the flow rate of sweep gas, C_{O_2} is the oxygen concentration in sweep gas, C_{N_2} is the amount of nitrogen leaking into the sweep gas and A is the effective area of the membranes.

5.3. Results and discussion

5.3.1 Optimization of LSCF/GDC dual-phase membranes

To perform oxygen separation from air, the LSCF/GDC powder needs to be sintered into dense membranes at high temperatures (e.g. 1400 ℃). However, it has been reported that reactions between the two phases at high temperatures may form impurities, which reduce the

oxygen permeation of membranes because the undesired impurities sit between the grain boundaries, blocking the transport of oxygen ions.[11, 20] Thus, using two materials without causing phase reactions at sintering temperatures is important for preparing dual-phase membranes. Figure 5-2 shows XRD patterns of the prepared membranes. By comparison with pure LSCF and GDC membranes, it can be seen that no impurity peak is found in the dual-phase membranes, which suggests no new phase was formed between LSCF and GDC at the sintering temperature used. We found LSCF peaks such as at 32.6^{o} shifted to the right and the GDC peaks slightly shifted to the left in LSCF-GDC dual-phase the membranes compared to the peaks of pure LSCF and GDC membranes. According to Bragg's equation ($n\lambda=2d\sin\theta$), the peak shifts are related to the shrinkage of LSCF crystals and the expansion of GDC crystals. At 1400 °C, LSCF begins to melt or creep, which might result in the mobilization of elements such as Sr and Co from LSCF crystals migrating into GDC crystals or volatization of metal elements, resulting in LSCF crystal shrinkage and and GDC crystal expansion.

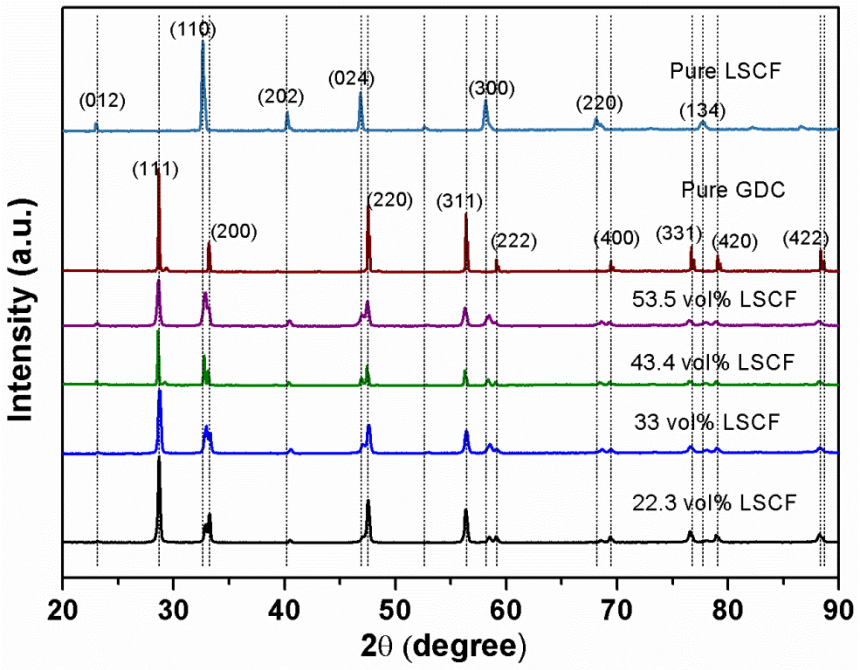

Figure 5-2. XRD patterns of pure LSCF, GDC membranes and the dual-phase membranes with different LSCF volume ratios.

The intensities of XRD peaks changed with the LSCF volume ratio. As the LSCF volume ratio was increased, GDC and LSCF peaks decreased, indicating crystal size decreases according to the Scherrer Equation. The XRD results are consistent with particle sizes shown

in Figure 5-3. As the LSCF volume ratio was increased from 22.3% to 53.5%, the dispersion role of each phase to prevent the other phase from sintering was enhanced, resulting in the smaller particles.

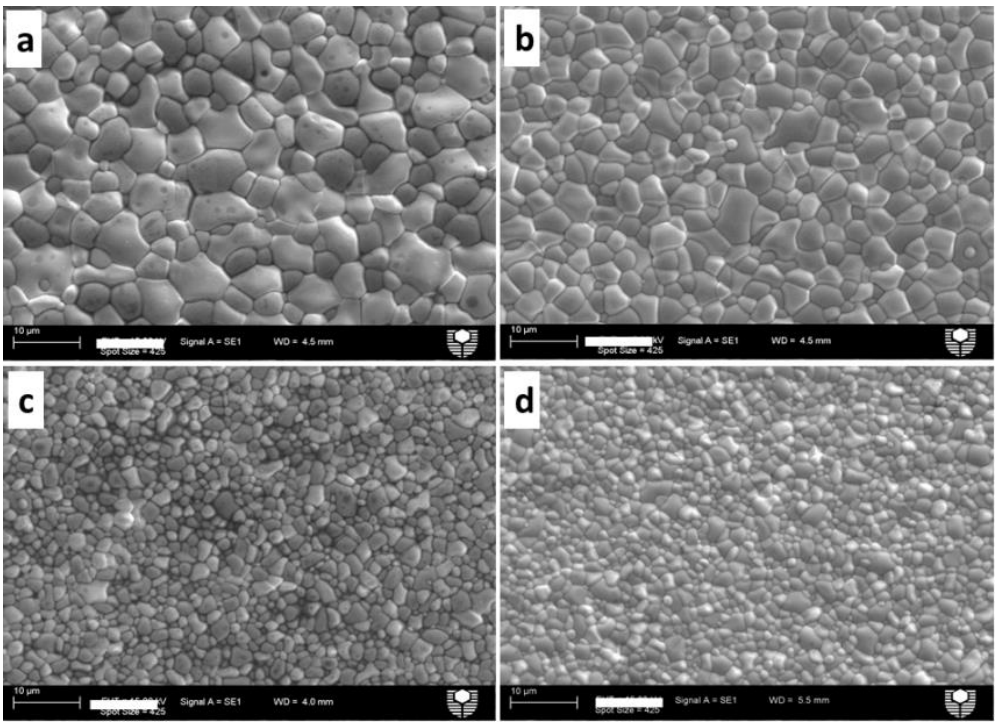

Figure 5-3. SEM images of the surface of membranes with different LSCF volume ratios: a, 22.3 %, b, 33 %, c, 43.4 % and d, 53.5 %. Scale bars are 10 µm.

As the oxygen permeation through ceramic membranes is rate-limited by bulk diffusion and/or surface reactions, the component optimization of the dual-phase membrane needs to be conducted under conditions such that bulk diffusion controls the oxygen permeation, in order to eliminate the effect of surface reactions. Oxygen permeation through thick membranes (e.g. above 0.8 mm in thickness) is known to be controlled by bulk diffusion.[21] In this study, membrane thicknesses are in the range from 1.5 to 2 mm. Figure 5-4 shows that the oxygen fluxes are inversely proportional to the thicknesses for all dual-phase membranes at different LSCF volume ratios, suggesting that the oxygen permeations of the dual-phase membranes were rate-limited by the bulk diffusion.[3, 12] Therefore, it is valid to compare the oxygen fluxes through the dual-phase membranes with a thickness of 2 mm to optimize the ratios of the two components in the mixture. The dual-phase membranes with 33 vol% LSCF (30 wt%) achieved the highest oxygen fluxes, which is similar to the result of the $Ce_{0.85}Sm_{0.15}O_{1.925}$-$Sm_{0.6}Sr_{0.4}CrO_3$ dual-phase membrane.[13]

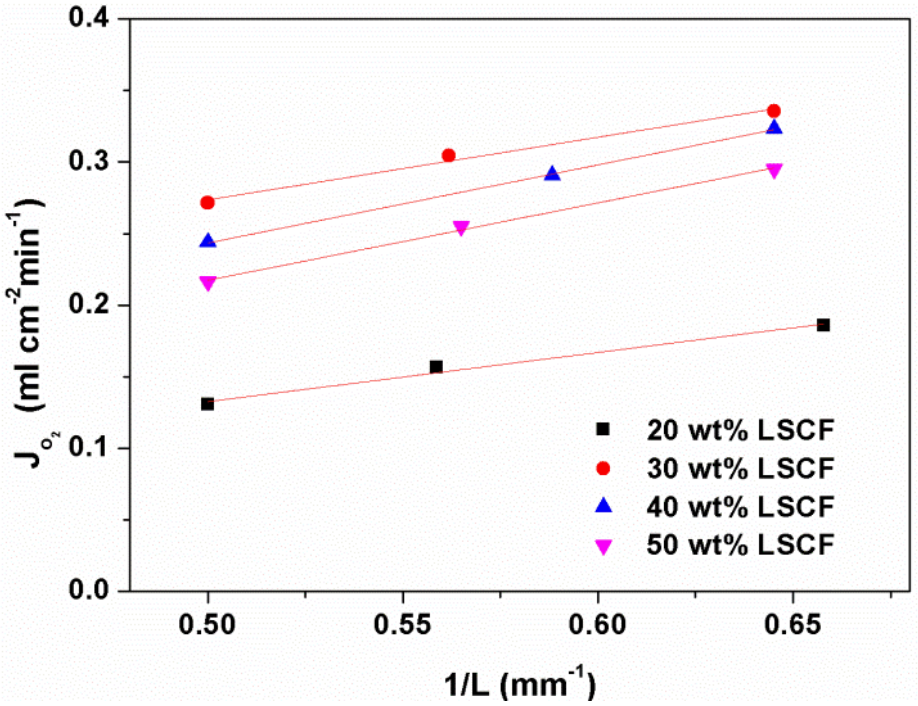

Figure 5-4. Membrane thickness (L) dependence of oxygen fluxes through the dual-phase disk membranes with different LSCF volume ratios.

Figure 5-5 shows the Arrhenius plot of oxygen permeation through the dual-phase disk membranes with a thickness of 2 mm, and the activation energies are 34.6, 44.2, 45.6 and 47.6 kJ mol^{-1} for the membranes with LSCF volume ratios of 22.3 %, 33 %, 43.4 % and 53.5 %, respectively. LSCF ceramic has higher electronic conductivity and lower ionic conductivity compared to GDC ceramic.[11] As the LSCF volume ratio is decreased in the dual-phase membranes, the electronic conductivity of the membrane decreases while the ionic conductivity increases. The threshold for a percolating network is around 30 vol%.[22] Therefore, as the LSCF volum ratio was decreased to 22.3 vol% (below the threshold), the limitation to the oxygen permeation was changed from oxygen ion diffusion to electron diffusion because LSCF particles cannot form a percolating conductive network for electron movement, leading to the sudden decrease of oxygen permeation. The activation energy of electron diffusion is lower than that of oxygen ion diffusion. This is the reason that the activation energy of the oxygen permeation sharply decreased from 44.2 kJ mol^{-1} to 34.6 kJ mol^{-1} when the LSCF volume ratio was decreased from 33% to 22.3%. Among these membranes, the membrane with the LSCF volume ratio of 33 % had the balanced mixed ionic and electronic conductivities, resulting in the highest oxygen fluxes.

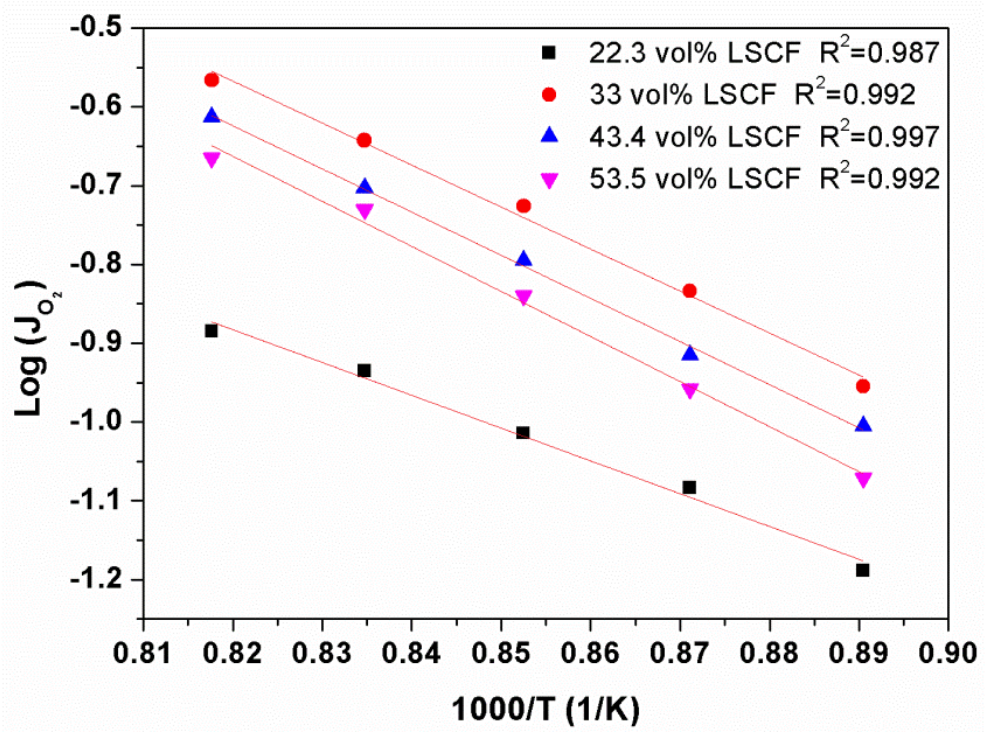

Figure 5-5. Arrhenius plots of oxygen permeation through the dual-phase membranes of thickness 2 mm.

5.3.2 Microchanneled dual-phase membranes

The LSCF/GDC composite with the optimized LSCF volume ratio of 33 % was made into microchanneled membranes to investigate their oxygen fluxes. To identify the flux improvement compared with pure LSCF membranes, the two types of the membranes need to have similar microstructures in order to make them comparable. The membrane structure was tuned via the slurry components, as described in chapter 4.[17] Cross-section SEM images of the microchanneled membranes are shown in Figure 5-6. The two membranes have comparable, long microchannels (around 700 µm) and thin dense layers (less than 100 µm), with the total thickness about 750 µm.

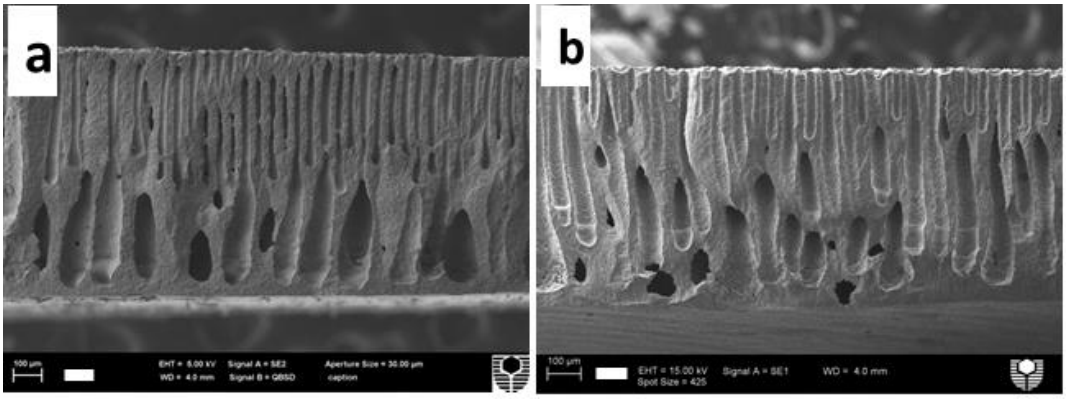

Figure 5-6. Cross-section SEM images of the dual-phase (a) and the pure LSCF (b) microchanneled membranes. The scale bars are 100 µm.

Oxygen permeation through the membranes was tested using air as feed gas on the microchannel side and argon as a sweep gas on the dense side over the temperature range 750 to 950 °C. Figure 5-7 shows a comparison of the oxygen permeation of the two membranes, with the dual-phase membrane showing much higher oxygen fluxes compared with the pure LSCF membrane. The pure LSCF membrane had an oxygen flux of 1.4 ml cm^{-2} min^{-1} at 950 °C. In contrast, the dual-phase membrane achieved an oxygen flux of 2.2 ml cm^{-2} min^{-1} at the same temperature, an improvement in the oxygen flux of 57%. As the two membranes have similar microstructure with a similar oxygen permeation distance, the oxygen flux improvement is attributed to the higher bulk diffusion rates within the dual-phase membrane compared to that within the pure LSCF membrane.

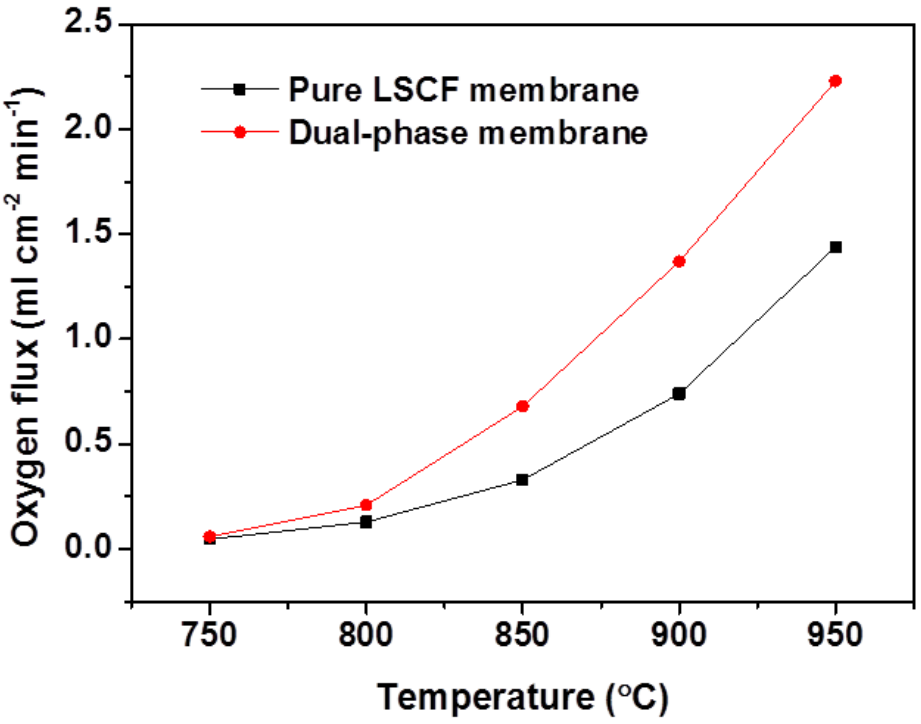

Figure 5-7. The oxygen fluxes of pure LSCF and dual-phase microchanneled membranes.

5.3.3 The effect of catalyst

Applying catalyst on a membrane surface is an efficient way of accelerating surface reactions when oxygen surface reactions are jointed in the rate limiting steps, and in turn increasing the oxygen flux. As the microchanneled membrane has an asymmetrical structure, catalyst was coated on the two sides of the membrane by two different methods, as described in Section 5.2.2. On the dense side of the membrane, the catalyst precursor was coated on the flat surface by spin-coating. Furfuryl alcohol was introduced into the catalyst precursor to form a uniform nanocatalyst coating.[19] Partially polymerized furfuryl alcohol has a strong adhesion on ceramic surfaces. Coupled with spin-coating at high rotation speeds, it can form a very thin and uniform catalyst coating. After the completion of furfuryl alcohol polymerization, the formed poly(furfuryl alcohol) immobilized the catalyst precursor within its network before solvent evaporation, which avoids the redistribution of catalyst and even catalyst aggregation that can occur during conventional coating processes. As shown in Figure 5-8b, the catalyst is uniformly distributed on the surface of the pure LSCF membrane with larger particles located near crystal boundaries because of the thicker catalyst coating near the

crystal boundary. As measured by SEM, the particle sizes are mostly less than 100 nm. EDX spectrum shows the bright particles are platinum (Figure 5-9). In addition, the smooth surface of the membrane before coating with catalyst (Figure 5-8a) became rough after coating (Figure 5-8b red ring). It is possible that the catalyst precursor reacted with the LSCF membrane or segregation of SrO occurred during the catalyst preparation.[23] However, this did not occur on the GDC surface. For the images of the dual-phase membrane in Figure 5-8c, GDC particles appear brighter than LSCF particles due to their heavier elements. After coating with catalyst, the smooth surface of GDC particle did not change and Pt catalyst particles preferentially stayed on the rough surface of LSCF particles.

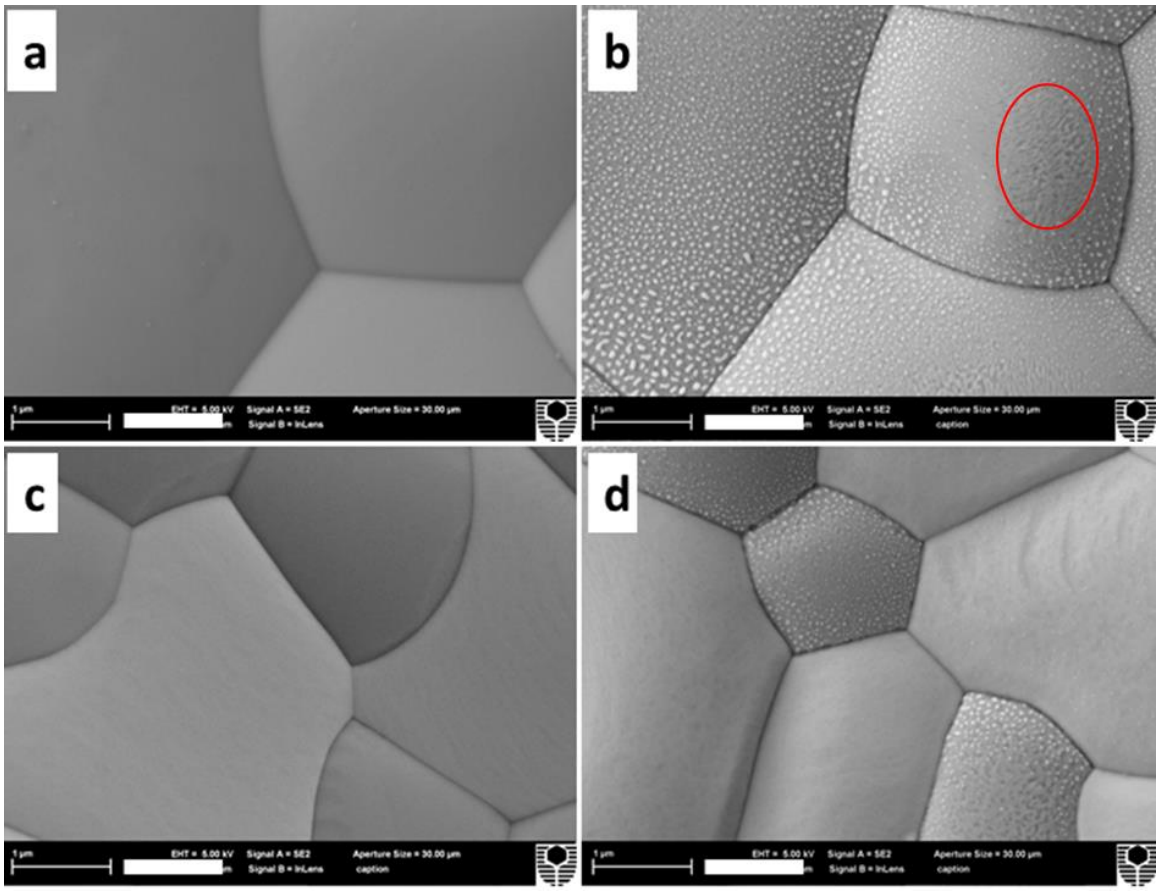

Figure 5-8. SEM images of the dense surfaces of an LSCF microchanneled membrane (a and b) and a dual-phase microchanneled membrane (c and d) before (a and c) and after (b and d) coating with catalyst. The red ring in Figure 5-8b is showing the rough surface. The scale bars are 1 µm.

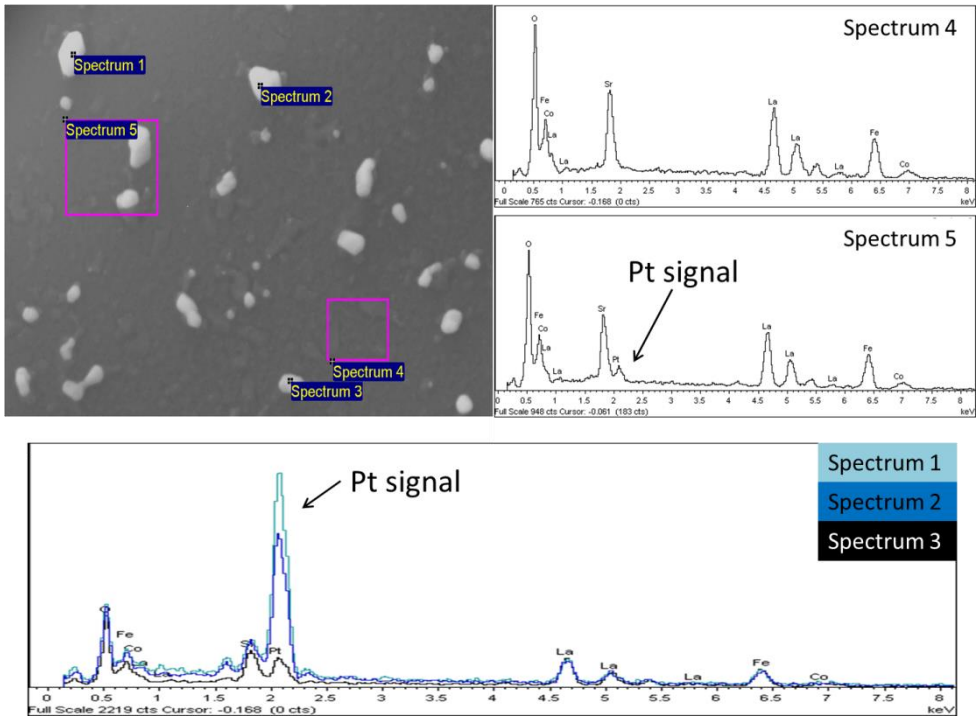

Figure 5-9. EDX elements scanning of Pt particles on membrane surface

Numerous open microchannels within membranes offer the opportunity to coat catalyst on both sides of the membrane, which is not feasible for conventional thin membranes supported on porous ceramics. Catalyst can readily be delivered to the membrane surface through the microchannels. Moreover, the microchannel structure greatly enlarges the membrane surface area located within the microchannels. However, conventional coating methods and wet-impregnation processes cannot be used to uniformly deposit catalyst on the channel wall surfaces. Instead, a polymer hydrogel assisted process was developed to coat catalyst on these surfaces.[18] The catalyst precursor solution was mixed with monomer solution, and then the microchannels were filled with the mixture. The mixture gelled after monomer polymerization, and catalyst precursor was uniformly held within the microchannels by the polymer network after drying off the water. The preferential deposition of Pt at grain boundaries could not be found here. This is in contrast to the conventional wet-impregnation process where catalyst precursor will condense at a certain places such as the bottom of the microchannels during solvent evaporation. Subsequent heat treatment burned off the polymer, and the catalyst was deposited on the microchannel walls. As seen in Figure 5-10, catalyst was deposited on the ceramic surfaces within the microchannels. Compared to the catalyst prepared by spin-coating on the flat membrane surface, the catalyst within the microchannels

is seen to be less uniform, with larger particle sizes (more than 100 nm). The non-uniform distribution of catalyst on LSCF and GDC particles was also found in Figure 5-10b.

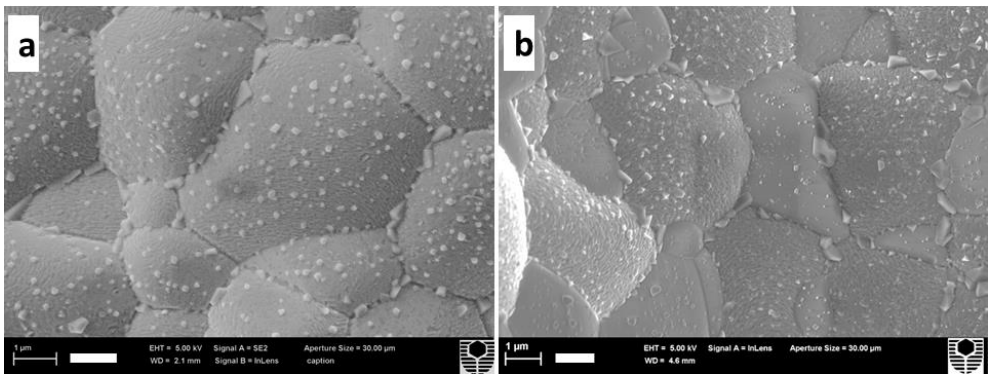

Figure 5-10. Surface images of the microchannels within (a) an LSCF membrane and (b) a dual-phase membrane with catalyst coatings. The scale bars are 1 µm.

The two membranes with catalyst coatings were tested for oxygen separation from air under the same conditions as the membranes without catalyst coating. The oxygen permeation results in Figure 5-11 show that the Pt catalyst increased the oxygen flux from 1.4 to 2.2 ml cm^{-2} min^{-1} for the pure LSCF membrane and from 2.1 to 3.8 ml cm^{-2} min^{-1} for the dual-phase membrane at 950 °C. The Arrhenius plots of oxygen permeation through microchanneled membranes are shown in Figure 5-12, and the activation energies for the pure LSCF membrane and the dual-phase membrane without catalyst are 87 and 95 kJ mol^{-1}, respectively. It is thought that the activation energy for surface reaction is larger than that for bulk diffusion because surface reactions are chemical processes and bulk diffusion is a physical process. The activation energy of the microchanneled membranes is much higher than that of the thick membranes (44.2 kJ mol^{-1}) (see Figure 5-4), which indicates the oxygen permeation through the microchanneled membranes is controlled by the combination of bulk diffusion and surface reaction.[24-26] After coating with catalyst, the activation energies for the pure LSCF membrane and the dual-phase membrane were reduced from 87 to 74 kJ mol^{-1} and from 95 to71 kJ mol^{-1} respectively, which confirms that surface reactions affect the oxygen permeation. Moreover, the catalyst has a larger effect on the activation energy of the dual phase membrane than on that of pure LSCF membranes. Consequently, the dual-phase membrane is limited by the surface reactions in the oxygen permeation process to a larger extent compared with the pure LSCF microchanneled membrane. One possible reason is that dual-phase membranes have a higher bulk diffusion rate than pure LSCF membranes.

Another possible reason is the LSCF ceramic has a higher surface exchange coefficient than the LSCF-GDC ceramic. In summary, through using dual-phase ceramic composite and applying catalyst on membrane surfaces, the oxygen flux of the microchanneled membrane has been increased from 1.4 to 3.8 ml cm^{-2} min^{-1} at 950 °C, improving by a factor of 2.7.

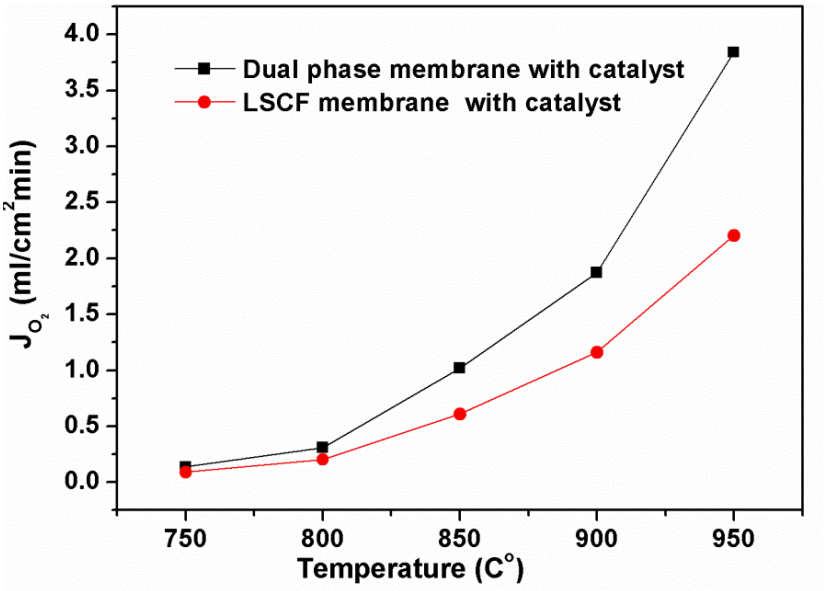

Figure 5-11. Oxygen fluxes of the pure LSCF microchanneled membrane and the dual-phase microchanneled membrane with catalyst coatings.

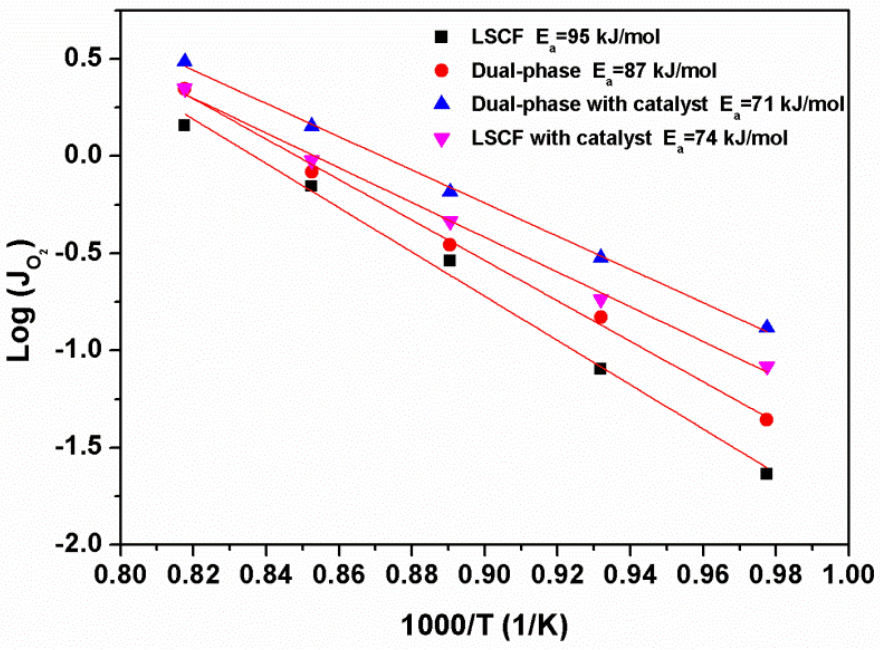

Figure 5-12. Arrhenius plots of oxygen permeation through microchanneled membranes.

5.4. Conclusion

The improvement of oxygen flux through microchanneled membranes has been achieved through using dual-phase membranes and applying catalyst on the membrane surfaces. The microchanneled structure offers an opportunity to investigate the effects of bulk diffusion and surface reaction on the oxygen permeation. Dual-phase membranes with balanced mixed conductivities were employed to increase the bulk diffusion rate, and catalyst was applied to accelerate surface reactions. Open microchannels crossing the membrane make it feasible to applying catalyst on both sides of the membrane. The final oxygen permeation flux reached 3.8 ml cm^{-2} min^{-1} at 950 °C, which is promising for practical applications.

5.5 References

1. R. W. Baker, *Industrial & Engineering Chemistry Research*, 2002, **41**, 1393-1411.
2. Y.-S. Lin, W. Wang and J. Han, *AIChE Journal*, 1994, **40**, 786-798.
3. J. Sunarso, S. Baumann, J. M. Serra, W. A. Meulenberg, S. Liu, Y. S. Lin and J. C. Diniz da Costa, *Journal of Membrane Science*, 2008, **320**, 13-41.
4. H. J. M. Bouwmeester, *Catalysis Today*, 2003, **82**, 141-150.
5. X. F. Zhu, H. Y. Liu, Y. Cong and W. S. Yang, *Chemical Communications*, 2012, **48**, 251-253.
6. Y. Teraoka, H. M. Zhang, S. Furukawa and N. Yamazoe, *Chem. Lett.*, 1985, 1743-1746.
7. K. Watanabe, M. Yuasa, T. Kida, K. Shimanoe, Y. Teraoka and N. Yamazoe, *Solid State Ionics*, 2008, **179**, 1377-1381.
8. F. Schulze-Kuppers, S. Baumann, W. A. Meulenberg, D. Stover and H. P. Buchkremer, *Journal of Membrane Science*, 2013, **433**, 121-125.
9. S. Baumann, J. M. Serra, M. P. Lobera, S. Escolastico, F. Schulze-Kuppers and W. A. Meulenberg, *Journal of Membrane Science*, 2011, **377**, 198-205.
10. X. Shao, D. Dong, G. Parkinson and C.-Z. Li, *Journal of Materials Chemistry A*, 2013, **1**, 9641-9644.

11. V. V. Kharton, A. V. Kovalevsky, A. P. Viskup, A. L. Shaula, F. M. Figueiredo, E. N. Naumovich and F. M. B. Marques, *Solid State Ionics*, 2003, **160**, 247-258.

12. M. B. Choi, S. Y. Jeon, H. J. Hwang, J. Y. Park and S. J. Song, *Solid State Ionics*, 2010, **181**, 1680-1684.

13. X. F. Zhu, M. R. Li, H. Y. Liu, T. Y. Zhang, Y. Cong and W. S. Yang, *Journal of Membrane Science*, 2012, **394**, 120-130.

14. H. X. Luo, K. Efimov, H. Q. Jiang, A. Feldhoff, H. H. Wang and J. Caro, *Angew. Chem.-Int. Edit.*, 2011, **50**, 759-763.

15. D. Han, J. Sunarso, X. Tan, Z. Yan, L. Liu and S. Liu, *Energy & Fuels*, 2012, **26**, 4728-4734.

16. X. Tan, Z. Wang, H. Liu and S. Liu, *Journal of Membrane Science*, 2008, **324**, 128-135.

17. X. Shao, D. Dong, G. Parkinson and C.-Z. Li, *Journal of Materials Chemistry A*, 2014, **DOI: 10.1039/C3TA13744A**.

18. D. Dong, Z. Chai, C.-Z. Li and H. Wang, *Materials Chemistry and Physics*, 2009, **118**, 148-152.

19. D. Dong, D. Li, X. Zhang, Z. Chai, K. Wang, C.-Z. Li, D. Zhao and H. Wang, *Journal of Materials Chemistry*, 2010, **20**, 1122-1126.

20. V. V. Kharton, A. V. Kovalevsky, A. P. Viskup, F. M. Figueiredo, A. A. Yaremchenko, E. N. Naumovich and F. M. B. Marques, *Journal of the European Ceramic Society*, 2001, **21**, 1763-1767.

21. T. Chen, H. L. Zhao, Z. X. Xie, L. C. Feng, X. G. Lu, W. Z. Ding and F. S. Li, *International Journal of Hydrogen Energy*, 2012, **37**, 5277-5285.

22. J. R. Wilson, J. S. Cronin, A. T. Duong, S. Rukes, H.-Y. Chen, K. Thornton, D. R. Mumm and S. Barnett, *Journal of Power Sources*, 2010, **195**, 1829-1840.

23. S. P. Jiang, S. Zhang and Y. D. Zhen, *Journal of The Electrochemical Society*, 2006, **153**, A127-A134.

24. K. Watanabe, M. Yuasa, T. Kida, K. Shimanoe, Y. Teraoka and N. Yamazoe, *Chemistry of Materials*, 2008, **20**, 6965-6973.

25. S. J. Xu and W. J. Thomson, *Chemical Engineering Science*, 1999, **54**, 3839-3850.

26. J. M. Serra, J. Garcia-Fayos, S. Baumann, F. Schulze-Kuppers and W. A. Meulenberg, *Journal of Membrane Science*, 2013, **447**, 297-305.

This work has been published on Journal of Membrane Science. I sincerely acknowledge the co-authors in this study, Dr. Dehua Dong, Professor Gordon Parkinson, Professor Chun-Zhu Li, for their assistance and guidance.

Chapter 6. Importance of microchannels in the oxygen permeation of microchanneled membranes

6.1 Introduction

Ceramic membranes for oxygen separation have attracted significant attention in recent years. The ceramic membrane relies on oxygen ion diffusion through dense solids and shows theoretically 100 % selectivity of oxygen separation. It is also considered as a cheaper technology than cryogenic separation, especially when the oxygen separation using ceramic membranes at high temperatures is coupled with high temperature reactions, such as natural gas conversion, coal gasification and oxyfuel combustion.[1-5]

Two major issues have hindered the commercialization of oxygen permeation membranes. Firstly, many materials with high intrinsic oxygen ion transfer rates have not shown the repeated long term stability. For example, a $Ba_{0.5}Sr_{0.5}Co_{0.8}Fe_{0.2}O_{3-\delta}$ and $SrCo_{0.8}Fe_{0.2}O_{3-\delta}$ membrane could produce an oxygen flux above 5 ml cm^{-2} min^{-1} at 900 °C, but they are unstable in CO_2 containing or reducing atmosphere due to chemical decomposition.[6-8] Secondly, many materials with strong chemical toughness exhibit small oxygen permeation fluxes, a tipical example is the dual phase material: 40 wt % $NiFe_2O_4$ and 60 wt % $Ce_{0.9}Gd_{0.1}O_{2-\delta}$.[9]

One approach to overcoming these issues is developing new membrane geometries and microstructures that bring benefits to oxygen permeation because the membrane geometry and microstructure are not necessarily limited by materials. The materials with good chemical stability can also be used to promote the oxygen permeation rate by modifying membrane geometry and microstructure. In Chapter 3, the microchanneled membranes with embedded microchannels open on one side of the membranes were fabricated using a mesh-templating phase inversion process.[10] With a superior structure to conventional supported membranes, the microchanneled membranes possess well-organized microchannels sitting on the thin dense layer, and these were formed by a one-step phase inversion process, showing good thermal compatibility. This microchanneled membrane produced high oxygen fluxes. For

example, $La_{0.6}Sr_{0.4}Co_{0.2}Fe_{0.8}O_{3-\delta}$ microchanneld membranes achieved oxygen fluxes of 3.2 ml cm^{-2} min^{-1} at 1000 °C and 2.45 ml cm^{-2} min^{-1} at 950 °C.[10]

In microchanneled membranes, oxygen permeation can be divided into 5 steps when the microchannel side is adopted as the air feeding side: oxygen diffusion into microchannels, oxygen surface reaction on the microchannel surfaces, oxygen ion bulk diffusion through the solid phase, oxygen surface reaction on the dense surface and oxygen viscous flow in the exiting gas phase. The last step, oxygen viscous flow in the gas phase, is generally considered to be fast and provides no resistance to the entire process.[11] It is also believed that the thin dense layer of microchanneled membrane shortened the oxygen diffusion distance. However, the initial two steps, oxygen diffusion into the microchannels and surface reaction on the microchannel surfaces, are still not clear. In microchanneled membranes, the whole microchannel wall can be catalytically active for oxygen surface reactions. Oxygen molecules diffuse into the microchannels and are consumed by the microchannel walls. Since the oxygen diffusion in gas phase is not necessarily greatly faster than the rates of oxygen consumption on microchannel walls. It is necessary to understand the interaction between those two steps and the related influence to oxygen permeation process.

In this Chapter, we respectively compare the oxygen permeations of microchanneled membranes to disk membranes and supported membranes. The contributions to oxygen flux from the microchannel surface and gas diffusion limitation will be discussed.

6.2. Experimental

6.2.1 Fabrication of microchanneled membranes

The mesh-templating phase inversion method starts with slurry preparation by planetary ball milling (MTI corporation, USA) of 30 g $La_{0.6}Sr_{0.4}Co_{0.2}Fe_{0.8}O_{3-\delta}$ (LSCF-6428, Fuel Cell Materials, Ohio, USA), 1.87 g polyethersulfone (PESF, Radel-A300), 0.21 g polyvinylpyrrolidone (PVP, MW=40000) and 11 g 1-methyl-2-pyrrolidinone (NMP, Sigma-aldrich, Australia) at a speed of 300 RPM for 48 hours to form a homogeneous slurry. The fabrication process of microchanneled membranes is described in Chapter 3.[12] The prepared green bodies of the microchanneled membranes were then sintered in air at 1300 °C in a box furnace (ModuTemp Pty. Ltd., Australia) for 5 hours to achieve dense membrane.

6.2.2. Fabrication of disk and porous supported membranes

Disk membranes were fabricated using the static pressure method followed by sintering at 1300 °C. The membrane thicknesses were managed by controlling the amount of powder used.

The porous supported membranes were made by a static pressure and dip coating method. Firstly, potato starch (Sigma-Aldrich, Australia) and $La_{0.6}Sr_{0.4}Co_{0.2}Fe_{0.8}O_{3-\delta}$ powder were mixed by mass ratio of 1:4 in ethanol using a ball mill at a speed of 400 RPM for 24 hours. After drying, the mixed power was hydraulically pressed under a pressure of 300 MPa to form the green body of the porous support. The green body was pre-sintered in a box furnace at 800 °C for 2 hours.

The dip coating slurry was prepared by mixing 3 g $La_{0.6}Sr_{0.4}Co_{0.2}Fe_{0.8}O_{3-\delta}$ powder, 27 g ethanol and 0.1 g PVP using a ball mill at the speed of 400 RPM for 24 hours. The pre-sintered porous support was dip coated in the slurry for several times to achieve the desired dense layer thickness. Finally, the membrane was sintered at 1200 °C in the box furnace for 5 hours to densify the coated layer.

6.2.3. Membrane characterization and testing

The membrane microstructure was observed by scanning electron microscopy (SEM, Zeiss Evo 40XVP). Membrane porosities were measured using Archimedes' method. In this study, the microchannel side of the microchanneled membranes was faced to the air feeding side in all experiments, because it had been shown to give a higher oxygen permeation flux in chapter 3. Argon was used as the sweep gas, and air or oxygen was supplied at the microchannel side or porous support side in this study. The gas flow rates were controlled by mass flow controllers (MFC, AALBORG). Oxygen concentration in the sweep gas was measured by online gas chromatography (GC, GC-2014, Shimadzu) with a packed column of molecular sieve 5Å. The oxygen permeation fluxes were calculated using the following equation,

$$J_{O_2} = \frac{\mathrm{F}_S(C_{O_2} - C_{N_2}(21/79))}{\mathrm{A}}$$

where J_{O_2} is the oxygen permeation flux of the membranes, F_S is the flow rate of the sweep gas, C_{O_2} is the oxygen concentration in sweep gas, C_{N_2} is the concentration of nitrogen leaking into sweep gas and A is the effective area of the membranes.

6.3. Results and discussion

6.3.1 Effects of gas flow rate

In order to study the influence of air flow rate to the oxygen permeation in microchanneled membranes, a supported membrane was fabricated for comparison. SEM images of a microchanneled membrane and a supported membrane are shown in Figure 6-1. The average dense layer thickness of the supported membrane and the microchanneled membrane were managed to be approximately 150 μm (Figure 6-1a-b). At the same magnification, the pore microstructure and microchannel structure are illustrated in Figure 6c and d. The pores in the supported membrane are around 5-10 μm, while the diameters of microchannels are about 30 μm; this indicates that the supported membrane presented a much larger surface area than the microchanneled membrane. The porosity of the microchanneled membrane was measured to be 22.7%, much lower than the 36.2% of the supported membrane. In this study, the oxygen permeation measurements of microchanneled membranes used the microchannel side as the air feeding side.

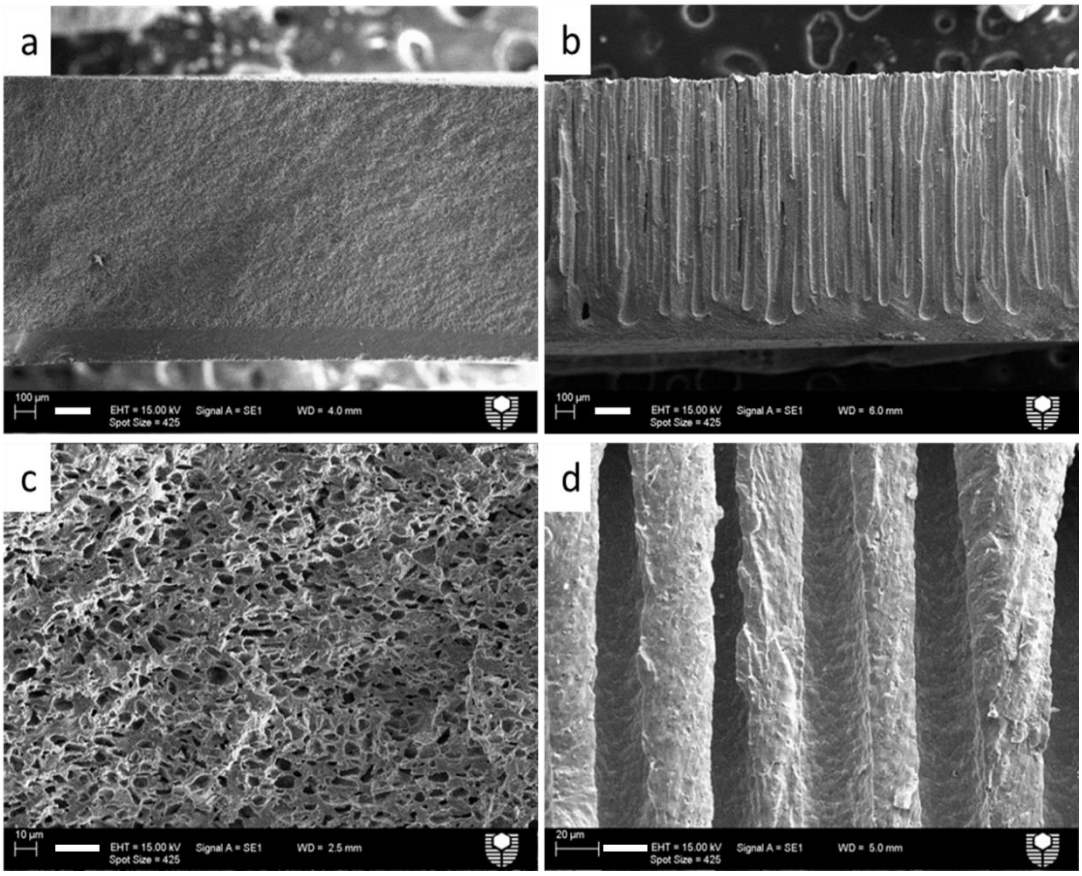

Figure 6-1. SEM images of the cross sections of a supported membrane (a), and a microchanneled membrane (b), high magnification images of the cross sections of supported membrane (c) and microchanneled membrane (d). The white bars are 200 µm in a and b while 20 µm in c and d.

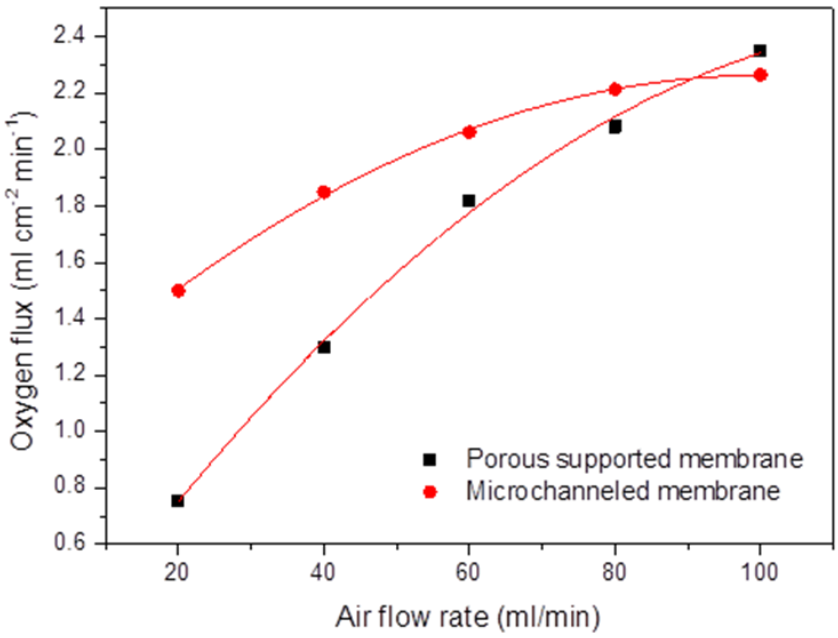

Figure 6-2. Air flow rate dependence of the oxygen permeation rate of a microchanneled membrane and a supported membrane at 1000 °C. The sweep gas flow rate was maintained at 100 ml min^{-1}.

Figure 6-2 shows that the oxygen fluxes of a microchanneled membrane and a supported membrane as a function of air flow rate. The oxygen fluxes of both the microchanneled and supported membranes increased with air flow rate. When the air flow rate increased from 20 to 100 ml min^{-1}, the increase of oxygen flux of the microchanneled membrane was quite small, from 1.5 to 2.3 ml min^{-1}. In contrast, the oxygen flux of the supported membrane increased from 0.76 to 2.4 ml min^{-1}. The oxygen permeation of the supported membrane was very sensitive to the change of air flow rates. It indicates that the gas diffusion resistance of the supported membrane was higher than that in the microchanneled membrane and the gas diffusion resistance of the supported membrane was mainly from the external of the porous support. Figure 6-3 shows the gas diffusion pathways in supported and microchanneled membrane. Due to the small pore size (5-10 μm) and tortuous pathways for gas diffusion in the porous support, the air supply can only effectively influence the external diffusion for the porous support.[13] However, the air supply could influence some part of the microchannels and cause micro-turbulence in the microchannels because the large channel size (30 μm) and straight channel shape. Therefore, it could largely promote the gas diffusion in the microchannels.

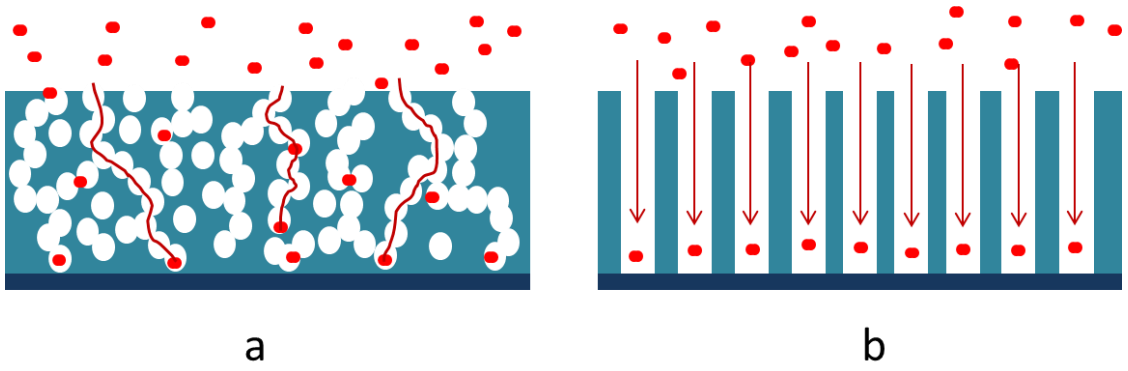

Figure 6-3. Graphic illustration of gas diffusion in a porous supported membrane (a) and a microchanneled membrane (b). External and internal parts, reaction zones in a and b are showing different length scales, but not quantitatively demonstration.

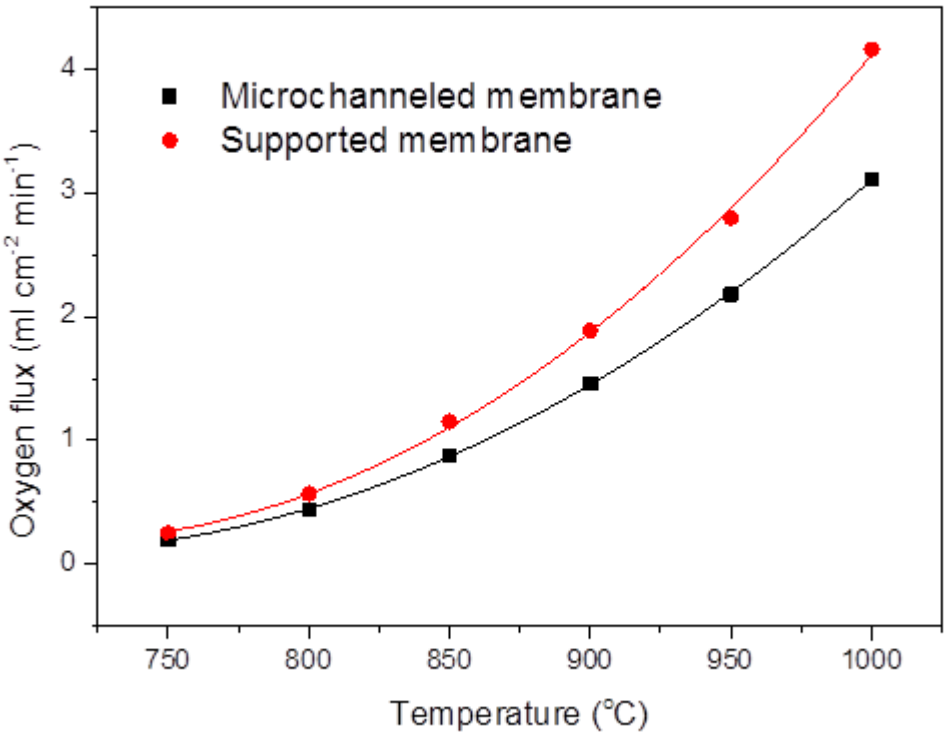

Figure 6-4. Oxygen permeation measurement of a microchanneled membrane and a supported membrane in a pure oxygen feeding atmosphere. The sweep gas flow rate was maintained at 100 ml min^{-1}.

The oxygen permeations of the microchanneled and the supported membranes were further measured in a pure oxygen feeding atmosphere (Figure 6-4). The supported membrane showed a higher oxygen flux than the microchanneled membrane. At 1000 °C, the values were 4.2 ml cm^{-2} min^{-1}, and 3.1 ml cm^{-2} min^{-1} for supported and microchanneled membrane, respectively. In pure oxygen atmosphere, the oxygen partial pressure was fixed through the microchannels and porous support. The high oxygen flux of the supported membrane was attributed to its higher surface area than the microchanneled membrane. It further explains that the supported membrane showed higher gas diffusion resistance than the microchanneled membrane when they were operated in air feeding atmosphere. The small gas diffusion resistance of the microchanneled membrane operating in air also suggests that the microchanneled membrane is more favourable in practical applications compared with the supported membrane because a high speed of air flow may crack the membrane and also be energy inefficient.

Figure 6-5 presents the Arrhenius plots of oxygen permeation as a result of applying different air flow rates. When 100 ml min^{-1} air flow rate was applied, the supported membrane achieved a higher oxygen flux than the microchanneled membrane. Nevertheless, the oxygen flux of the supported membrane was much smaller than that of the microchanneled membrane when only 20 ml min^{-1} air flow rate was applied. According to Arrhenius equation,

$$lnJ_{O_2} = -\frac{E}{RT} + lnA$$

where J_{O_2} is the oxygen permeation flux, E is activation energy, R is the idea gas constant, T is temperature and A is pre-exponential factor. Therefore, plot the graph with lnJ_{O_2} against $\frac{1}{T}$, the activation energy can be calculated using the slope of the trend line. It is generally believed the oxygen permeation is rate limited by ionic bulk diffusion at high temperature and shows an activation energy about 80-90 kJ mol^{-1}, while it is rate limited by oxygen surface reactions at low temperature range and shows an activation energy around 180-200 kJ mol^{-1}.[11] Comparatively, oxygen diffusion in the gas phase demonstrates much smaller activation energy, and therefore, the apparent activation energy can be small when the oxygen permeation is jointly rate limited by oxygen gas diffusion with another step. This gas diffusion resistance can also be indicated by the activation energies given in Table 6-1. The oxygen permeation in the supported membrane exhibits smaller activation energies than in the microchanneled membrane, which indicates that gas diffusion was involved in the overall

rate-limiting step because the gas diffusion activation energies are generally small.[14] It has been reported that the activation energies of LSCF-6428 are 115 kJ mol^{-1} for oxygen bulk diffusion and 191 kJ mol-1 for oxygen surface reactions.[11] Based on the comparison of the activation energies, no matter large or small air flow rate was applied, the oxygen permeations of supported membranes were largely rate-limited by oxygen diffusion in gas phase. When the air flow rate decreased from 100 to 20 ml min^{-1}, both activation energies of microchanneled and supported membranes were decreased, suggesting the gas diffusion tends to be more involved in the rate-limiting steps. In comparison, when 100 ml min^{-1} air flow rate was applied, the oxygen permeations of microchanneled membrane were dominantly controlled by the oxygen bulk diffusion and the surface reactions at high and low temperature, respectively. However, by decreasing the air flow rate to 20 ml min^{-1}, the oxygen permeation of the microchanneled membrane was jointly rate-limited by oxygen diffusion in gas phase and oxygen diffusion in solid phase at high temperature while it was still dominantly controlled by oxygen surface reactions in the low temperature range.

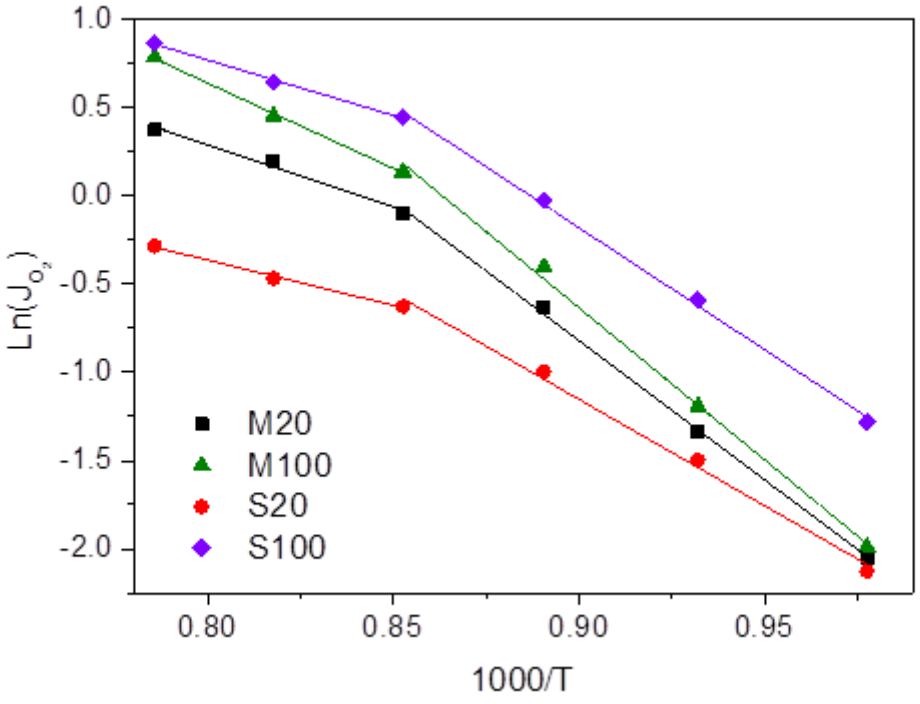

Figure 6-5. Arrhenius plot of oxygen permeation in a microchanneled membrane and a supported membrane with different air supply rates. M20, M100, S20, S100 represent a microchanneled membrane with 20 ml min^{-1} air supply rate, a microchanneled membrane

with 100 ml min^{-1} air supply rate, a supported membrane with 20 ml min^{-1} air supply rate and a supported membrane with 100 ml min^{-1} air supply rate, respectively.

Table 6-1. Activation energies of microchanneled and supported membranes.

Temperature range (°C)	Activation energies (kJ/mol)			
	Microchanneled membrane		Supported membrane	
	20 ml/min air flow rate	100 ml/min air flow rate	20 ml/min air flow rate	100 ml/min air flow rate
900-1000	58	80	42	52
750-900	131	143	100	115

6.3.2 Contribution of oxygen flux from microchannel walls

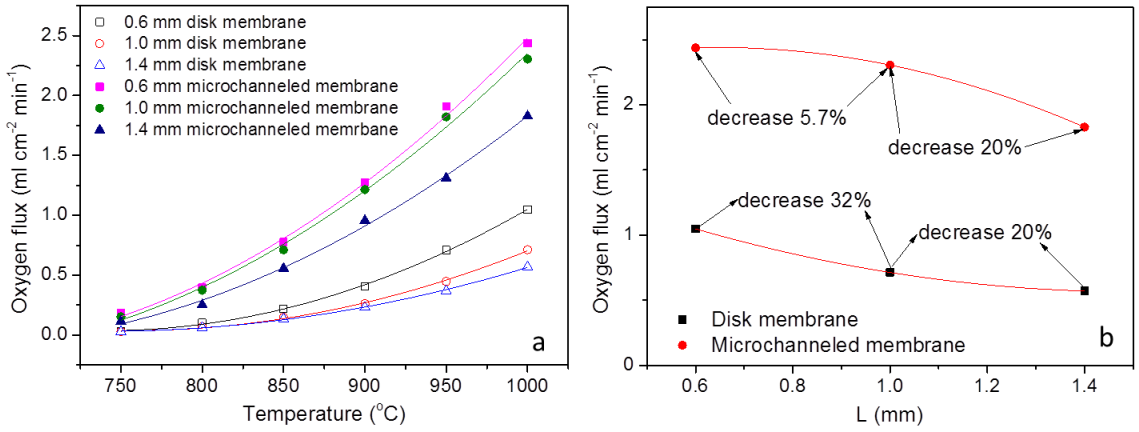

Figure 6-6. a) Oxygen fluxes of microchanneled membranes and disk membranes with different thicknesses, the dense layer thickness remained the same in the microchanneled membranes with different thicknesses. b) Decreases in oxygen flux with increasing of membrane thicknesses at 1000 °C. Oxygen partial pressures difference was maintained at 0.21/0.004 atm and the air flow rate was 100 ml min^{-1}.

Oxygen permeation fluxes of microchanneled and disk membranes are given in Figure 6-6a. To minimize the gas diffusion effect, 100 ml min^{-1} air flow rate was applied in the following measurements. Since the microchannels in different membranes could be slightly different, it is better to use only one microchanneled membrane to maintain the measurement comparability of microchanneled membrane with different thicknesses. Therefore, in these measurements, only one microchanneled membrane was used by gradually polishing in steps

to achieve the required overall thickness. The polishing was only conducted at microchannel side and the dense layer of the microchanneled membrane remained the same. The microchanneled membrane was finally polished to have 0.6 mm thickness; further polishing cannot be conducted because the very thin membrane was not strong enough for handling. The oxygen partial pressure differences across the membranes were fixed in order to measure the activation energies. As shown, the oxygen fluxes increased with decreasing membrane thicknesses. The microchanneled membranes showed much higher oxygen fluxes than dense membranes. For the membranes with 0.6 mm thickness, the oxygen flux of the microchanneled membrane achieved 2.4 ml cm^{-2} min^{-1} while the disk membrane only achieved 1 ml cm^{-2} min^{-1} at 1000 °C (Figure 6-6a). It is also noticed that by increasing the membrane thicknesses, the rates of oxygen flux decrease for the microchanneled and dense membranes are different. Figure 6-6b shows the oxygen flux decrease rate by increasing membrane thicknesses at 1000 °C. When the membrane thicknesses increased from 1.0 to 1.4 mm, the oxygen fluxes of the microchanneled and disk membranes similarly decreased by about 20%. However, the oxygen flux of the microchanneled membrane only decreased by 5.7% when the membrane thickness was changed from 0.6 to 1.0 mm. In comparison, the oxygen flux of the dense membrane decreased by 32% when the thickness was changed from 0.6 to 1.0 mm. This phenomenon may imply a specialty of the microchanneled membranes, over a certain range of membrane thicknesses (e.g. 0.6-1 mm in this study), oxygen flux could be only slightly influenced by changing the membrane thickness (i.e. the length of the microchannels).

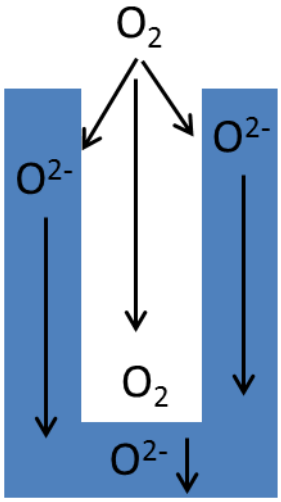

Figure 6-7. Graphic illustration of oxygen permeation paths in a microchannel

The observed changes in oxygen flux with membrane thickness in microchanneled membranes can be explained by the oxygen flux contribution from the microchannel walls. In microchanneled membranes, the oxygen reactions are illustrated in Figure 6-7. There are three types of oxygen pathways: oxygen molecules diffuse through the microchannels in the gas phase, oxygen molecules react with the microchannel bottom area and diffuse through the solid phase, and oxygen molecules react with microchannel walls and diffuse through the solid phase (longer pathway). It is believed that the oxygen permeation can occur at the entire surface of microchannel wall. This has been proved in supported membranes: the surface reaction current of oxygen ions increases with porous support thickness.[15, 16] Based on the literatures,[15, 17] the oxygen flux is expected to increase with microchanneled membrane thickness when oxygen partial pressure is unchanged in gas phase; however, this was not found in our study (see Figure 6-6a). Figure 6-8 shows the oxygen fluxes measured in pure oxygen atmosphere for microchanneled membranes with different thicknesses. Here, the oxygen partial pressure was unchanged and the oxygen flux did increase with membrane thickness. The increasing oxygen flux with microchanneled membrane thickness can be attributed to the contribution of oxygen permeation from the microchannel walls. However, it can also be observed in Figure 6-8, oxygen flux largely increased with membrane thickness from 0.6 to 1.0 mm, however, further increase of the membrane thickness does not effectively promote oxygen flux. This is because the microchannel walls far away from the microchannel bottom contribute small proportion to the overall oxygen flux. Similar phenomenon has been reported in supported membranes, when oxygen partial pressure remains unchanged in gas phase, a large improvement of oxygen flux cannot gain by increasing the thickness of the porous support when the porous support is thick enough.[15, 17]

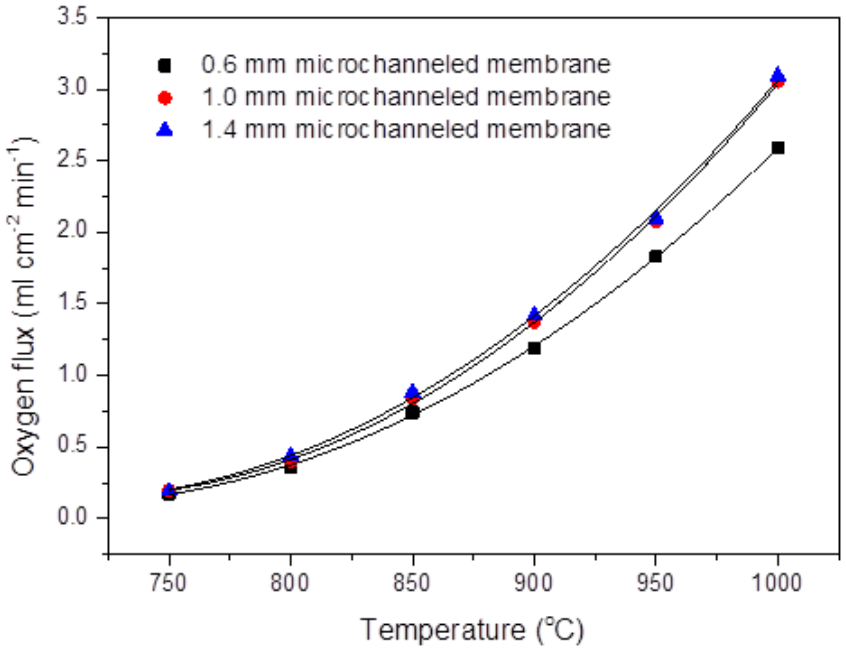

Figure 6-8. Microchanneled membrane with different thicknesses in pure oxygen. Sweep gas flow rate was maintained at 100 ml min^{-1}.

6.3.3 The rate-limiting steps during oxygen permeation

Oxygen permeation fluxes of microchanneled membranes in air and pure oxygen feeding atmospheres showed inverse results. This is attributed to the oxygen partial pressure gradient in the microchannels when the membranes are measured in air. In the pure oxygen measurement, the oxygen partial pressure in the microchannels is constant throughout their length. The surface ion current is only determined by surface exchange kinetics and ionic diffusion in solid phase.[18] The oxygen flux contributed by the microchannel walls can be observed by increasing membrane thickness. However, when the microchanneled membrane was measured in air, the continuous consumption of oxygen molecules on microchannel walls created an oxygen concentration gradient inside the microchannels. Consequently, the gas diffusion step becomes a rate-limiting part of the oxygen permeation process and the overall oxygen flux exhibit a joint effect of gas diffusion resistance and microchannel wall contribution. In summary, increasing the thickness of microchanneled membranes could increase the gas diffusion resistance as well as increase more surface area for oxygen permeation. It is well known that oxygen permeation membranes require high mechanical strength in practical applications. A potential advantage of the microchanneled membranes

may be deduced that the microchanneled membranes could enhance the mechanical strength with little sacrificing of oxygen flux (increase membrane thickness), but this advantage could only exist within a certain thickness range.

Figure 6-9 shows the Arrhenius plots of oxygen permeation in microchanneled and disk membranes. The activation energies were calculated using the slopes of the figure and summarized in Table 6-2. During the oxygen permeation process in microchanneled membranes, the oxygen permeations occurred at the surface close to microchannel bottom area are expected to be rate-limited by oxygen surface reaction due to the thin diffusion distance in solid phase (150 μm). As a result, the overall activation energies of oxygen permeations in microchanneled membranes would have been expected to be much larger than those in dense membranes with same thicknesses because oxygen permeation in microchanneled membrane can be conducted at different thickness scales (Figure 6-7). In Figure 6-9, the activation energies of the microchanneled membranes are smaller than those of dense membranes over the same temperature range. This implies that the gaseous diffusion of oxygen was involved in the whole process because the activation energy for gas diffusion is fairly small,[14] and therefore, leading to smaller apparent activation energies.

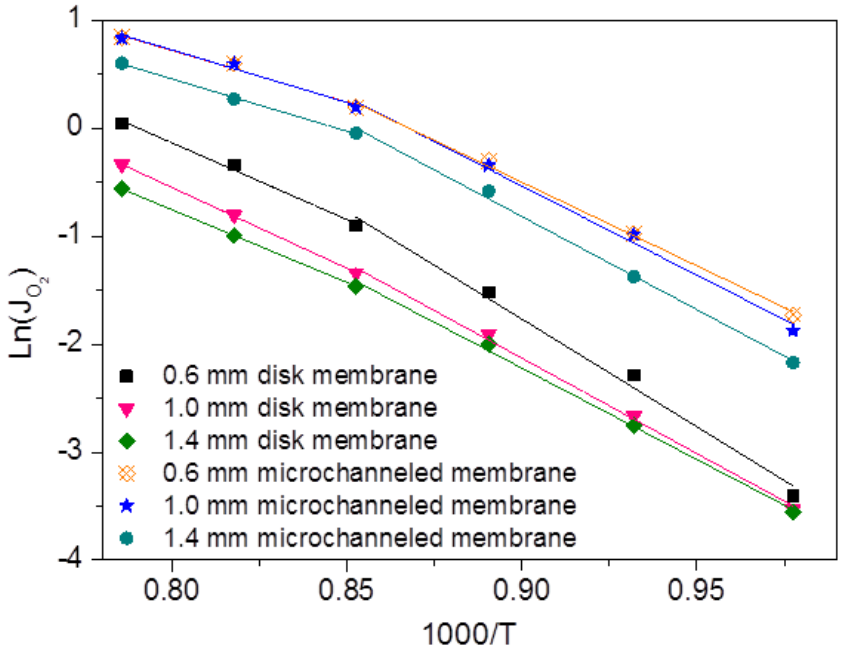

Figure 6-9. Arrhenius plots of oxygen permeations on microchanneled and disk membranes.

Table 6-2. Activation energies of microchanneled and disk membranes.

	Activation energies (kJ/mol)					
Temperature range (°C)	**Microchanneled membranes**			**Disk membranes**		
	0.6 mm	1.0 mm	1.4 mm	0.6 mm	1.0 mm	1.4 mm
900-1000	80	80	81	118	124	112
750-900	129	137	141	166	147	141

In high temperature range (900-1000 °C), the activation energies of dense membranes are close to the value of oxygen bulk diffusion (115 kJ mol^{-1}) in LSCF-6428 membranes, which indicates the oxygen permeation of dense membranes are rate-limited by oxygen diffusion in solid phase. However, their activation energies increased to around 150 kJ mol^{-1} in the low temperature range (750-900 °C); these values are located between the activation energy values of oxygen bulk diffusion and surface reactions (191 kJ mol^{-1}), suggesting that the oxygen permeations of dense membranes were jointly rate-limited by oxygen bulk diffusion and surface reactions. In contrast, the activation energies of microchanneled membranes in the high temperature range, about 80 kJ mol^{-1}, are much lower than that of oxygen bulk diffusion in LSCF-6428 membranes. In the low temperature range, the activation energies of microchanneled membranes are smaller or close to those of dense membranes. This further confirms that gas diffusion was involved in the oxygen permeation process in microchanneled membranes.

6.4 Conclusion

The oxygen permeation of microchanneled membranes was compared with those of supported and dense membranes in this study. It was found gas diffusion resistance was involved in the oxygen permeation process of microchanneled membranes and the gas diffusion resistance was proved to be much smaller than in supported membranes. When membrane thicknesses were both 1.4 mm, the microchannled membranes showed much higher oxygen flux than supported membranes at 1000 °C if the air feeding rate was small. In practical application, for the purpose of energy saving and lowering the risk of membrane cracking, small air feeding rate will be preferable, and therefore, microchanneled membranes will be preferable. The microchannled membrane was also shown to produce a much higher oxygen flux than the dense membranes with same thickness. The oxygen flux of microchanneled membranes did not decrease significantly with an increase of thickness from 0.6 – 1.0 mm because of the oxygen flux contribution from the microchannel walls,

suggesting that microchanneled membranes could potentially be made with improved mechanical strength by increasing the membrane thickness to some extent.

6.5 References

1. U. Balachandran, J. Dusek, R. L. Mieville, R. Poeppel, M. Kleefisch, S. Pei, T. Kobylinski, C. Udovich and A. Bose, *Applied Catalysis A: General*, 1995, **133**, 19-29.
2. U. Balachandran, J. Dusek, P. Maiya, B. Ma, R. Mieville, M. Kleefisch and C. Udovich, *Catalysis Today*, 1997, **36**, 265-272.
3. A. Leo, S. Liu and J. C. D. d. Costa, *International Journal of Greenhouse Gas Control*, 2009, **3**, 357-367.
4. S. Smart, C. Lin, L. Ding, K. Thambimuthu and J. D. Da Costa, *Energy & Environmental Science*, 2010, **3**, 268-278.
5. H. Stadler, F. Beggel, M. Habermehl, B. Persigehl, R. Kneer, M. Modigell and P. Jeschke, *International Journal of Greenhouse Gas Control*, 2011, **5**, 7-15.
6. B. J. Mitchell, R. C. Rogan, J. W. Richardson Jr, B. Ma and U. Balachandran, *Solid State Ionics*, 2002, **146**, 313-321.
7. S. McIntosh, J. F. Vente, W. G. Haije, D. H. A. Blank and H. J. M. Bouwmeester, *Solid State Ionics*, 2006, **177**, 833-842.
8. M. Arnold, T. M. Gesing, J. Martynczuk and A. Feldhoff, *Chemistry of Materials*, 2008, **20**, 5851-5858.
9. H. Luo, K. Efimov, H. Jiang, A. Feldhoff, H. Wang and J. Caro, *Angewandte Chemie International Edition*, 2011, **50**, 759-763.
10. X. Shao, D. Dong, G. Parkinson and C.-Z. Li, *Journal of Materials Chemistry A*, 2013, **1**, 9641-9644.
11. S. J. Xu and W. J. Thomson, *Chemical Engineering Science*, 1999, **54**, 3839-3850.
12. X. Shao, D. Dong, G. Parkinson and C.-Z. Li, *Journal of Materials Chemistry A*, 2014, **2**, 410-417.
13. C. K. Ho, Webb, Stephen W. , *Gas Transport in Porous Media*, Springer, 2006.
14. A. B. Shelekhin, A. G. Dixon and Y. H. Ma, *AIChE Journal*, 1995, **41**, 58-67.
15. H. Deng, M. Zhou and B. Abeles, *Solid State Ionics*, 1994, **74**, 75-84.
16. A. Häffelin, C. Niedrig, S. F. Wagner, S. Baumann, W. A. Meulenberg and E. Ivers-Tiffée, *Journal of The Electrochemical Society*, 2014, **161**, F1409-F1415.

17. S. B. Adler, J. A. Lane and B. C. H. Steele, *Journal of The Electrochemical Society*, 1996, **143**, 3554-3564.
18. S. Wang, A. Verma, Y. L. Yang, A. J. Jacobson and B. Abeles, *Solid State Ionics*, 2001, **140**, 125-133.

Chapter 7: Conclusions and recommendations

7.1 Conclusions

In this thesis, a novel microchanneled membrane structure was developed using mesh-templating phase inversion method. This membrane structure showed much higher oxygen flux than conventional dense membrane. The membrane formation mechanism, process compatibility to other material, further improvement of the oxygen flux by modifying membrane materials and the influence of the microchannels to oxygen flux were specifically studied. Through these studies, several general conclusions can be made as follows.

7.1.1 A microchanneled ceramic membrane for highly-efficient oxygen separation

- The novel microchanneled membrane structure was developed using mesh-templating phase inversion process. The process would be easy to be scaled up to industry scale.

- The formed microchanneled membrane demonstrated much higher oxygen flux than conventional disk membrane.

- The microchanneled membranes showed high mechanic strength.

7.1.2 Microstructure control of oxygen permeation membranes with templated microchannels

- Based on the study of the mesh-templating phase inversion process, the microchanneled structure can be controlled by modifying a few parameters: the method of applying coagulant, coagulant component, phase inversion time and slurry component.

- The microcahnneled membrane with the most regular and the longest microchannels showed the highest oxygen flux because the membrane with the most regular and the longest microchannels had the highest surface area.

- The formation mechanism of microchannels during phase inversion was specifically discussed. It was concluded that the high miscibility of solvent and non-solvent as well as the low viscosity of slurry assist the growth of microchannels.

7.1.3 Improvement of oxygen permeation through microchanneled ceramic membranes

- The microchanneled membrane was fabricated using dual-phase materials. It proves the compatibility of the microchanneled structure to other materials.

- By balancing the ionic and electrical conductivities of materials, the microchanneled membrane showed improved oxygen flux.

- The large surface area of microchanneled membrane is suitable for catalyst coating. The oxygen flux of microchanneled membrane can be further improved by coating catalyst.

7.1.4 Investigation of microchannel influence in the oxygen permeation of microchanneled membranes

- Microchanneled membranes can improve their mechanic strength by increasing the membrane thicknesses to some extent because the oxygen flux contribution from microchannel walls could partially offset the oxygen flux reduction due to the increase of the microchanneled membrane thickness.

- The oxygen flux reduction due to the increase of microchanneled membrane thicknesses was caused by oxygen diffusion resistance in gas phase.

- Compared with the supported membrane, the gas diffusion resistance of the microchanneled membrane was much smaller. Therefore, the microchanneled membrane showed much higher oxygen flux than supported membrane when small air flow rate was supplied.

7.2 Recommendations

1. This study targeted the development of new membrane microstructure. The material applied in this study, $La_{0.6}Sr_{0.4}Co_{0.2}Fe_{0.8}O_{3-\delta}$, is not the material with high oxygen diffusion rate or good chemical stability in CO_2, H_2S containing atmosphere. The further work can focus on the further improvement of oxygen flux or enhance the chemical stability by changing materials.

2. This study experimentally analyzed the microchanneled membranes formation process and oxygen permeation in microchanelled membranes. Due to the characteristics of the microchanneled membranes, it was difficult to figure out a quantitative analysis regarding the rate limiting step, oxygen flux contribution from microchannel wall and bottom area. A mathematic modelling study is expected to answer those questions in the future.

3. The microcahnneled membrane can also be used in many aplications, such as natural gas reforming, CO_2 and water reduction, solid oxide fuel cells, oxygen pumps, batteries, etc. It is necessary to investigate the performance of microchanneled membrane in these applications.

Appendix

Permission of Reproduction from the Copyright Owner

Copyright Clearance Center RightsLink®

Home | Account Info | Help

Title: Improving oxygen permeability in SrFeCo0.5Ox asymmetric membranes by modifying support-layer porous structure

Publication: Materials Letters

Publisher: Elsevier

Date: May 2005

Logged in as:
xin shao
LOGOUT

Order Completed

Thank you very much for your order.

This is a License Agreement between xin shao ("You") and Elsevier ("Elsevier"). The license consists of your order details, the terms and conditions provided by Elsevier, and the payment terms and conditions.

Get the printable license.

License Number	3564500251221
License date	Feb 08, 2015
Licensed content publisher	Elsevier
Licensed content publication	Materials Letters
Licensed content title	Improving oxygen permeability in SrFeCo0.5Ox asymmetric membranes by modifying support-layer porous structure
Licensed content author	None
Licensed content date	May 2005
Licensed content volume number	59
Licensed content issue number	11
Number of pages	5
Type of Use	reuse in a thesis/dissertation
Portion	figures/tables/illustrations
Number of figures/tables/illustrations	1
Format	both print and electronic
Are you the author of this Elsevier article?	No
Will you be translating?	No
Order reference number	102
Original figure numbers	figure 5
Title of your thesis/dissertation	Microchanneled ceramic membrane for oxygen separation from air
Expected completion date	Feb 2015
Estimated size (number of pages)	180
Elsevier VAT number	GB 494 6272 12
Permissions price	0.00 AUD
VAT/Local Sales Tax	0.00 AUD / 0.00 GBP

Title:	Oxygen permeation through tape-cast asymmetric all-La0.6Sr0.4Co0.2Fe0.8O3−δ membranes
Author:	José M. Serra,Julio Garcia-Fayos,S. Baumann,F. Schulze-Küppers,W.A. Meulenberg
Publication:	Journal of Membrane Science
Publisher:	Elsevier
Date:	15 November 2013

Order Completed

Thank you very much for your order.

This is a License Agreement between xin shao ("You") and Elsevier ("Elsevier"). The license consists of your order details, the terms and conditions provided by Elsevier, and the payment terms and conditions.

Get the printable license.

License Number	3564500663415
License date	Feb 08, 2015
Licensed content publisher	Elsevier
Licensed content publication	Journal of Membrane Science
Licensed content title	Oxygen permeation through tape-cast asymmetric all-La0.6Sr0.4Co0.2Fe0.8O3−δ membranes
Licensed content author	José M. Serra,Julio Garcia-Fayos,S. Baumann,F. Schulze-Küppers,W.A. Meulenberg
Licensed content date	15 November 2013
Licensed content volume number	447
Licensed content issue number	n/a
Number of pages	9
Type of Use	reuse in a thesis/dissertation
Portion	figures/tables/illustrations
Number of figures/tables/illustrations	1
Format	both print and electronic
Are you the author of this Elsevier article?	No
Will you be translating?	No
Order reference number	103
Original figure numbers	Figure 1
Title of your thesis/dissertation	Microchanneled ceramic membrane for oxygen separation from air
Expected completion date	Feb 2015
Estimated size (number of pages)	180
Elsevier VAT number	GB 494 6272 12

Title:	Ultrahigh oxygen permeation flux through supported Ba0.5Sr0.5Co0.8Fe0.2O3−δ membranes
Author:	S. Baumann,J.M. Serra,M.P. Lobera,S. Escolástico,F. Schulze-Küppers,W.A. Meulenberg
Publication:	Journal of Membrane Science
Publisher:	Elsevier
Date:	15 July 2011

Order Completed

Thank you very much for your order.

This is a License Agreement between xin shao ("You") and Elsevier ("Elsevier"). The license consists of your order details, the terms and conditions provided by Elsevier, and the payment terms and conditions.

Get the printable license.

License Number	3564581398871
License date	Feb 09, 2015
Licensed content publisher	Elsevier
Licensed content publication	Journal of Membrane Science
Licensed content title	Ultrahigh oxygen permeation flux through supported Ba0.5Sr0.5Co0.8Fe0.2O3−δ membranes
Licensed content author	S. Baumann,J.M. Serra,M.P. Lobera,S. Escolástico,F. Schulze-Küppers,W.A. Meulenberg
Licensed content date	15 July 2011
Licensed content volume number	377
Licensed content issue number	1-2
Number of pages	8
Type of Use	reuse in a thesis/dissertation
Portion	figures/tables/illustrations
Number of figures/tables/illustrations	1
Format	both print and electronic
Are you the author of this Elsevier article?	No
Will you be translating?	No
Order reference number	104
Original figure numbers	Figure 1
Title of your thesis/dissertation	Microchanneled ceramic membrane for oxygen separation from air
Expected completion date	Feb 2015
Estimated size (number of pages)	180
Elsevier VAT number	GB 494 6272 12

Order Completed

Thank you very much for your order.

This is a License Agreement between xin shao ("You") and Elsevier ("Elsevier"). The license consists of your order details, the terms and conditions provided by Elsevier, and the payment terms and conditions.

Get the printable license.

License Number	3564500899390
License date	Feb 08, 2015
Licensed content publisher	Elsevier
Licensed content publication	Journal of Membrane Science
Licensed content title	A novel dual-layer ceramic hollow fibre membrane reactor for methane conversion
Licensed content author	Zhentao Wu, Bo Wang, K. Li
Licensed content date	15 April 2010
Licensed content volume number	352
Licensed content issue number	1-2
Number of pages	8
Type of Use	reuse in a thesis/dissertation
Portion	figures/tables/illustrations
Number of figures/tables/illustrations	1
Format	both print and electronic
Are you the author of this Elsevier article?	No
Will you be translating?	No
Order reference number	159
Original figure numbers	Figure 1
Title of your thesis/dissertation	Microchanneled ceramic membrane for oxygen separation from air
Expected completion date	Feb 2015
Estimated size (number of pages)	180
Elsevier VAT number	GB 494 6272 12
Permissions price	0.00 AUD
VAT/Local Sales Tax	0.00 AUD / 0.00 GBP
Total	0.00 AUD

Order Completed

Thank you very much for your order.

This is a License Agreement between xin shao ("You") and Elsevier ("Elsevier"). The license consists of your order details, the terms and conditions provided by Elsevier, and the payment terms and conditions.

Get the printable license.

License Number	3564501007172
License date	Feb 08, 2015
Licensed content publisher	Elsevier
Licensed content publication	Journal of Membrane Science
Licensed content title	A morphological study of ceramic hollow fibre membranes
Licensed content author	Benjamin F.K. Kingsbury,K. Li
Licensed content date	20 February 2009
Licensed content volume number	328
Licensed content issue number	1-2
Number of pages	7
Type of Use	reuse in a thesis/dissertation
Portion	figures/tables/illustrations
Number of figures/tables/illustrations	1
Format	both print and electronic
Are you the author of this Elsevier article?	No
Will you be translating?	No
Order reference number	1
Original figure numbers	Figure 1
Title of your thesis/dissertation	Microchanneled ceramic membrane for oxygen separation from air
Expected completion date	Feb 2015
Estimated size (number of pages)	180
Elsevier VAT number	GB 494 6272 12
Permissions price	0.00 AUD
VAT/Local Sales Tax	0.00 USD / 0.00 GBP
Total	0.00 AUD

Title: Phase separation in polysulfone/solvent/water and polyethersulfone/solvent/water systems

Author: Wayne W.Y. Lau,Michael D. Guiver,T. Matsuura

Publication: Journal of Membrane Science

Publisher: Elsevier

Date: 1 June 1991

Order Completed

Thank you very much for your order.

This is a License Agreement between xin shao ("You") and Elsevier ("Elsevier"). The license consists of your order details, the terms and conditions provided by Elsevier, and the payment terms and conditions.

Get the printable license.

License Number	3564501155006
License date	Feb 08, 2015
Licensed content publisher	Elsevier
Licensed content publication	Journal of Membrane Science
Licensed content title	Phase separation in polysulfone/solvent/water and polyethersulfone/solvent/water systems
Licensed content author	Wayne W.Y. Lau,Michael D. Guiver,T. Matsuura
Licensed content date	1 June 1991
Licensed content volume number	59
Licensed content issue number	2
Number of pages	9
Type of Use	reuse in a thesis/dissertation
Portion	figures/tables/illustrations
Number of figures/tables/illustrations	1
Format	both print and electronic
Are you the author of this Elsevier article?	No
Will you be translating?	No
Order reference number	179
Original figure numbers	Figure 1
Title of your thesis/dissertation	Microchanneled ceramic membrane for oxygen separation from air
Expected completion date	Feb 2015
Estimated size (number of pages)	180
Elsevier VAT number	GB 494 6272 12
Permissions price	0.00 AUD
VAT/Local Sales Tax	0.00 USD / 0.00 GBP

Title: A morphological study of ceramic hollow fibre membranes: A perspective on multifunctional catalytic membrane reactors

Author: Benjamin F.K. Kingsbury,Zhentao Wu,K. Li

Publication: Catalysis Today

Publisher: Elsevier

Date: 31 October 2010

Order Completed

Thank you very much for your order.

This is a License Agreement between xin shao ("You") and Elsevier ("Elsevier"). The license consists of your order details, the terms and conditions provided by Elsevier, and the payment terms and conditions.

Get the printable license.

License Number	3564501350658
License date	Feb 08, 2015
Licensed content publisher	Elsevier
Licensed content publication	Catalysis Today
Licensed content title	A morphological study of ceramic hollow fibre membranes: A perspective on multifunctional catalytic membrane reactors
Licensed content author	Benjamin F.K. Kingsbury,Zhentao Wu,K. Li
Licensed content date	31 October 2010
Licensed content volume number	156
Licensed content issue number	3-4
Number of pages	10
Type of Use	reuse in a thesis/dissertation
Portion	figures/tables/illustrations
Number of figures/tables/illustrations	1
Format	both print and electronic
Are you the author of this Elsevier article?	No
Will you be translating?	No
Order reference number	163
Original figure numbers	Figure 11
Title of your thesis/dissertation	Microchanneled ceramic membrane for oxygen separation from air
Expected completion date	Feb 2015
Estimated size (number of pages)	180
Elsevier VAT number	GB 494 6272 12

Order Completed

Thank you very much for your order.

This is a License Agreement between xin shao ("You") and Elsevier ("Elsevier"). The license consists of your order details, the terms and conditions provided by Elsevier, and the payment terms and conditions.

Get the printable license.

License Number	3564501471376
License date	Feb 08, 2015
Licensed content publisher	Elsevier
Licensed content publication	Chemical Engineering Science
Licensed content title	Influence of permeation modes on oxygen permeability of the multichannel mixed-conducting hollow fibre membrane
Licensed content author	None
Licensed content date	27 January 2015
Licensed content volume number	122
Licensed content issue number	n/a
Number of pages	8
Type of Use	reuse in a thesis/dissertation
Portion	figures/tables/illustrations
Number of figures/tables/illustrations	1
Format	both print and electronic
Are you the author of this Elsevier article?	No
Will you be translating?	No
Order reference number	158
Original figure numbers	Figure 4
Title of your thesis/dissertation	Microchanneled ceramic membrane for oxygen separation from air
Expected completion date	Feb 2015
Estimated size (number of pages)	180
Elsevier VAT number	GB 494 6272 12
Permissions price	0.00 AUD
VAT/Local Sales Tax	0.00 USD / 0.00 GBP

Order Completed

Thank you very much for your order.

This is a License Agreement between xin shao ("You") and Elsevier ("Elsevier"). The license consists of your order details, the terms and conditions provided by Elsevier, and the payment terms and conditions.

Get the printable license.

License Number	3565660993641
License date	Feb 10, 2015
Licensed content publisher	Elsevier
Licensed content publication	Journal of Membrane Science
Licensed content title	Improvement of oxygen permeation through microchanneled ceramic membranes
Licensed content author	Xin Shao,Dehua Dong,Gordon Parkinson,Chun-Zhu Li
Licensed content date	15 March 2014
Licensed content volume number	454
Licensed content issue number	n/a
Number of pages	7
Type of Use	reuse in a thesis/dissertation
Portion	full article
Format	both print and electronic
Are you the author of this Elsevier article?	Yes
Will you be translating?	No
Title of your thesis/dissertation	Microchanneled ceramic membrane for oxygen separation from air
Expected completion date	Feb 2015
Estimated size (number of pages)	180
Elsevier VAT number	GB 494 6272 12
Permissions price	0.00 AUD
VAT/Local Sales Tax	0.00 USD / 0.00 GBP
Total	0.00 AUD